2018

HIGH-ORDER INTEGRAL EQUATION METHODS FOR QUASI-MAGNETOSTATIC AND CORROSION-RELATED FIELD ANALYSIS WITH MARITIME APPLICATIONS

Robert Pfeiffer
University of Kentucky, robpfeiffer@gmail.com
Digital Object Identifier: https://doi.org/10.13023/ETD.2018.212

STUDENT AGREEMENT:

I represent that my thesis or dissertation and abstract are my original work. Proper attribution has been given to all outside sources. I understand that I am solely responsible for obtaining any needed copyright permissions. I have obtained needed written permission statement(s) from the owner(s) of each third-party copyrighted matter to be included in my work, allowing electronic distribution (if such use is not permitted by the fair use doctrine) which will be submitted to UKnowledge as Additional File.

I hereby grant to The University of Kentucky and its agents the irrevocable, non-exclusive, and royalty-free license to archive and make accessible my work in whole or in part in all forms of media, now or hereafter known. I agree that the document mentioned above may be made available immediately for worldwide access unless an embargo applies.

I retain all other ownership rights to the copyright of my work. I also retain the right to use in future works (such as articles or books) all or part of my work. I understand that I am free to register the copyright to my work.

REVIEW, APPROVAL AND ACCEPTANCE

The document mentioned above has been reviewed and accepted by the student's advisor, on behalf of the advisory committee, and by the Director of Graduate Studies (DGS), on behalf of the program; we verify that this is the final, approved version of the student's thesis including all changes required by the advisory committee. The undersigned agree to abide by the statements above.

Robert Pfeiffer, Student

Dr. John C. Young, Major Professor

Dr. Cai-Cheng Lu, Director of Graduate Studies

HIGH-ORDER INTEGRAL EQUATION METHODS FOR QUASI-MAGNETOSTATIC AND CORROSION-RELATED FIELD ANALYSIS WITH MARITIME APPLICATIONS

DISSERTATION

A dissertation submitted in partial fulfillment of the
requirements for the degree of Doctor of Philosophy in the
College of Engineering
at the University of Kentucky

By
Robert Pfeiffer
Lexington, Kentucky

Director: Dr. John C. Young, Professor of
Electrical and Computer Engineering
Lexington, Kentucky

2018

ABSTRACT OF DISSERTATION

HIGH-ORDER INTEGRAL EQUATION METHODS FOR QUASI-MAGNETOSTATIC AND CORROSION-RELATED FIELD ANALYSIS WITH MARITIME APPLICATIONS

This dissertation presents techniques for high-order simulation of electromagnetic fields, particularly for problems involving ships with ferromagnetic hulls and active corrosion-protection systems.

A set of numerically constrained hexahedral basis functions for volume integral equation discretization is presented in a method-of-moments context. Test simulations demonstrate the accuracy achievable with these functions as well as the improvement brought about in system conditioning when compared to other basis sets.

A general method for converting between a locally-corrected Nyström discretization of an integral equation and a method-of-moments discretization is presented next. Several problems involving conducting and magnetic-conducting materials are solved to verify the accuracy of the method and to illustrate both the reduction in number of unknowns and the effect of the numerically constrained bases on the conditioning of the converted matrix.

Finally, a surface integral equation derived from Laplace's equation is discretized using the locally-corrected Nyström method in order to calculate the electric fields created by impressed-current corrosion protection systems. An iterative technique is presented for handling nonlinear boundary conditions. In addition we examine different approaches for calculating the magnetic field radiated by the corrosion protection system. Numerical tests show the accuracy achievable by higher-order discretizations, validate the iterative technique presented. Various methods for magnetic field calculation are also applied to basic test cases.

KEYWORDS: Locally-Corrected Nyström, Computational Electromagnetics, Integral Equation, Quasi-Magnetostatic, Corrosion Protection

Robert Pfeiffer

May 17, 2018

Date

HIGH-ORDER INTEGRAL EQUATION METHODS FOR QUASI-MAGNETOSTATIC AND CORROSION-RELATED FIELD ANALYSIS WITH MARITIME APPLICATIONS

By

Robert Pfeiffer

John C. Young

Director of Dissertation

Cai-Cheng Lu

Director of Graduate Studies

May 17, 2018

ACKNOWLEDGEMENTS

I am indebted to my advisor Dr. John C. Young for his continual instruction and advice during my graduate research. I am thankful for the opportunity to benefit from his knowledge and expertise in theoretical and computational electromagnetics. His patient and thorough guidance has been an immense help in my research and in learning the fundamentals of a complex and fascinating field.

I am grateful to Dr. Robert J. Adams and Dr. Stephen D. Gedney for their advice and insights during my studies and research. It has been a real privilege to work with the electromagnetics team at the University of Kentucky.

My thanks to Dr. Cai-Cheng Lu and Dr. David Jensen for serving on my defense committee, and for the thorough instruction they have given me in electromagnetics and analysis. I am also grateful for the support of the Office of Naval Research through grants N00014-15-1-2270 and N00014-16-1-3066 that made this research possible.

I owe many thanks to the excellent teachers under whom I have been privileged to study at the University of Kentucky as well as at Thomas Aquinas College and the Milwaukee School of Engineering. I am also very grateful to my parents and family for their loving encouragement throughout my education. Lastly, I must gratefully acknowledge my patient and loving wife, whose cheerful and selfless support has been a constant inspiration during my graduate studies.

TABLE OF CONTENTS

LIST OF TABLES

LIST OF FIGURES

CHAPTER 1. Introduction

Modern electronic technology has come to rely increasingly on a precise understanding of electromagnetic phenomena and their applications. As devices become more intricate and specifications more demanding, the expense of constructing prototypes, coupled with the difficulty of obtaining accurate measurements from prototypes once constructed, makes it necessary in practice to have precise and robust computational simulation techniques.

Methods for modeling electromagnetic devices and problems have been under development for decades now, and commercial software is widely available to solve many of the problems encountered in industry. In principle, computational solutions can be obtained for all manner of electromagnetic problems via methods that have been known for years. Research in this area continues nevertheless, aiming to improve the efficiency of existing methods without sacrificing accuracy. This is particularly true where very large structures are involved, since here an accurate simulation requires an abundance of computational resources and can be very time-consuming. Yet it is also in designing these structures, where prototype construction and testing carry particularly heavy time and resource requirements, that accurate and practical simulations are especially needed.

In marine engineering the study of the electromagnetic properties of ships and other maritime structures has become particularly important in recent years. Vessels must often be designed with special attention to aspects such as the magnetic field generated or scattered by the ferromagnetic hull and by other structures and systems onboard.

This paper proposes efficient numerical techniques for predicting electromagnetic fields caused by magnetic and conducting materials, mainly with a view to modeling marine structures. First, we look at a technique for streamlining computation of the quasi-magnetostatic fields scattered by conducting and ferromagnetic objects. Second, we look at high-order modeling of corrosion-related electric and magnetic fields produced by active corrosion countermeasures on structures in electrolytic media.

1.1 Magnetostatic Nyström-Moment Method Conversion Using Numerically Constrained Basis Functions

Chapters 2 and 3 present a method for constructing high-order divergence conforming basis functions on hexahedral cells, and investigate the effect of these basis functions on the solution of quasi-magnetostatic volume integral equations involving conducting and conducting-magnetic materials.

1.1.1 High-Order Basis Functions for Well-Conditioned Integral Equation Discretizations

Integral equation methods for solving electromagnetic problems are often preferable to alternative approaches in problems involving scatterers in infinite or semi-infinite media. Such methods necessitate the discretization of the structure of interest but not of the surrounding medium, as would be required in finite-difference or finite-element analysis. In many cases involving homogeneous scatterers, the boundary conditions at interfaces allow a surface integral equation to be used. Until relatively recently, integral equation solvers have relied extensively on low-order basis functions to approximate surface vector quantities. These include the well-known Rao-Wilton-Glisson (RWG) bases [1] and their analogues on other cell

types, e.g., the rooftop basis functions on quadrilaterals in [2,3] and the tetrahedral bases in [4].

More recent efforts have made increasing use of higher-order approximations, both in the representation of mesh geometry by higher-order curvilinear elements [5] and in the representation of unknowns with higher-order basis functions. The motivation behind this trend is the ability of higher-order methods to yield an increase in accuracy similar to that achieved by an increase in mesh refinement without a similar increase in the number of unknowns [6,7]. An overview of this adoption of higher-order methods can be found in [8].

The complexity of higher-order basis functions can make them difficult to implement in electromagnetic simulation programs. Moreover, the conditioning of the system matrix resulting from high-order bases can often degrade rapidly with increasing basis order if special care is is not taken in constructing the bases, making solution by fast solvers difficult [9–11]. This becomes problematic in modeling large structures where direct inversion of a dense matrix is impractical.

Basis functions with higher mutual orthogonality help to mitigate the growth in condition number with basis order. Examples are the quadrilateral and hexahedral bases constructed using the mutually orthogonal Legendre polynomials in [9,10]. More recently, a method for automatic numerical construction of basis functions to satisfy continuity constraints was also shown to give a substantial reduction in condition number. These *constrained bases* are used to solve surface integral equations with quadrilateral elements using Legendre polynomials in [11–14] and with triangular elements in [15] using the Koornwinder-Dubiner polynomials [16,17]. A similar method is used to derive divergence-conforming functions in [7].

As shown in [18], the method used to construct the quadrilateral constrained bases can be extended to hexahedral elements. This extension is discussed in Chapter 2 of this paper, and the resulting basis functions are characterized in

moment-method solutions of dielectric scattering problems.

1.1.2 Conversion of Nyström Discretization of Quasi-Magnetostatic Problems with Eddy Currents to Well-Conditioned Moment-Method Discretization

Prediction of the fields scattered by magnetic objects is often performed using integral equation methods. While surface integral equations can be used for problems with linear, homogeneous materials [19,20], many practical problems will involve hysteretic materials, requiring a volume integral equation approach. While the method of moments can be used to solve the resulting volume integral equation [21], the expense of numerical integrations in moment-method codes makes the point-based Nyström method an attractive alternative. This is particularly desirable where large structures are concerned, as in the case of sea vessels. The singular kernels used in electromagnetic integral equations require the *locally corrected* Nyström (LCN) method described in [13, 22, 23]. An integral formulation based on the $\mathbf{H} - \mathrm{M}$ formulation [24,25] is shown and discretized using the LCN method in [26].

The magnetic problem becomes more complicated when the body under consideration is conducting and the field is not constant. Thus, for instance, when a conducting ship is in motion the ambient magnetic field can induce eddy currents in the hull. A volume integral equation (VIE) formulation of this problem is solved using the LCN method in [27]. Because low frequencies are often of interest, the system matrix condition number growth must be kept in check by using an augmented formulation, as in [28].

Two advantages of the LCN method, where interactions are defined between points on individual cells rather than between basis and test functions that may have support on multiple cells, are the consequent ease of using various element types (e.g. hexahedra, prisms, tetrahedra) in the same mesh [26] and the ability

to use a non-conformal mesh [23]. In problems such as the eddy current problem, however, where volume conduction or polarization currents are involved, the point-based Nyström approach does not by itself enforce the continuity in current that should exist between cells in a homogeneous region. This can cause a loss of accuracy, particularly at lower orders [13,22]. In certain formulations where charge density is modeled explicitly, the resulting fictitious boundary charges can increase the number of degrees of freedom in the problem [28].

As shown in [29], the moment method and Nyström method are equivalent by a linear transformation. This allows us to convert the LCN system matrix to a moment-method matrix. This conversion can reduce the number of degrees of freedom associated with quantities subject to continuity constraints, and in the augmented formulation it can eliminate additional degrees of freedom corresponding to fictitious boundary charges. This fact is taken advantage of at low orders in [30–32]. A conversion given in [12, 13] can be used to convert a Nyström matrix to the equivalent moment-method matrix using high-order constrained bases on quadrilaterals. In Chapter 3 of this paper, a more general conversion is proposed for converting a high-order Nyström matrix to a moment-method matrix discretized with arbitrary topological basis functions. The conversion is used to streamline the solution of quasi-magnetostatic problems with eddy currents, both by reducing the number of degrees of freedom and by using the bases presented in Chapter 2 to improve system conditioning. Numerical tests investigate the accuracy of solutions thus obtained as well as the numerical properties of both the Nyström matrix itself and the matrix resulting from the Nyström-moment method conversion. Both the constrained hexahedral basis functions and the interpolatory bases of [33] are used and compared.

1.2 Corrosion-Related Electric and Magnetic Field Simulation

In Chapters 4 and 5, the accurate computation of fields resulting from active corrosion protection systems on metal vessels in electrolytic media is discussed. Accurate prediction of the electric fields resulting from impressed-current cathodic protection systems is addressed in Chapter 4. Techniques for computing the resulting magnetic field are then discussed in Chapter 5.

1.2.1 Impressed-Current Corrosion Protection System Modeling

With the exception of the noble metals (e.g. gold, platinum), bare metal surfaces exposed to electrolytic solutions will decay as the metal oxidizes and dissolves into the surrounding fluid. While a metal ship hull is generally coated with a non-reactive paint that prevents this decay, this coating gradually wears away under the action of the elements and the mechanical stresses to which the ship's hull is continually subjected. As a result, patches of exposed metal will corrode over time.

The corrosion of submerged metal creates an electric current; electrons given up by the more easily corroded metal flow through the metal structure to regions of higher electric potential, e.g. an exposed surface made of more noble metal. For example, take an iron electrode connected to a copper electrode, both in a solution of sodium chloride (NaCl) in water. The iron is more readily corroded than the copper (it is said to be *less noble*) and so it is oxidized (cf. [34, 35])

$$\mathrm{Fe} \longrightarrow \mathrm{Fe}^{++} + 2\,\mathrm{e}^{-} \tag{1.1}$$

and the electrons e^{-} flow to the *anodic* copper electrode to fuel the reaction

$$2\,\mathrm{H}^{+} + 2\,\mathrm{e}^{-} \longrightarrow \mathrm{H}_2. \tag{1.2}$$

The dissolution of the iron ions in (1.1) gradually wears away the structure. Two general methods of corrosion protection are employed to slow this process. The first is to attach to the hull pieces of a metal that is less noble, or more easily corroded, than the metal making up the hull. These *sacrificial anodes* corrode in preference to the hull itself. For instance, a magnesium electrode placed in the electrolyte and electrically connected to the iron electrode in the above example will corrode instead of the iron.

The alternative protection method investigated here is an impressed-current cathodic protection (ICCP) system. In such a system, rather than current being supplied by the oxidation of a sacrificial anode, a dc power supply is connected to the structure. The negative side of the dc supply is connected to the exposed surface, and the positive side to an exposed electrode made of a noble metal such as platinum.

While the sacrificial anode approach is simple, it does suffer from certain drawbacks. These include the added weight of the electrodes, the effect on the ship's hydrodynamics [36], and the inconvenience of replacing the electrodes as they deteriorate [37]. This last point is also relevant in onshore applications, e.g., the protection of reinforced concrete structures [38]. ICCP systems tend to be regarded as the better option for structures with longer life expectancies [39]. The use of an ICCP system also allows for the dc current to be adjusted, based on potential measurements from probes placed around the hull, in order to optimize protection and power efficiency [40].

Design of corrosion protection systems originally relied on experimental work and on engineering experience and expertise [39, 41]. One popular technique is *physical scale modeling*, where a scale model of the structure is subjected to measurements in a medium of similarly scaled conductivity [41–43]. It is often desirable, however, to predict the performance of the system under many different

sets of conditions, making accurate computational modeling a preferable alternative [42, 44].

Computational simulation of ICCP systems is useful in predicting the efficacy and longevity of a given configuration [45] and in optimizing the power consumption of the impressed-current system [40]. Moreover, accurate numerical models can be used in conjunction with voltage sensors on the hull to estimate the location and degree of paint damage [40, 46, 47]. Another motivation for developing accurate modeling techniques is the increasing need to compute accurately the fields radiated by a ship with an onboard ICCP system. On large ships, the corrosion-related currents can have a measurable impact on the surrounding magnetic field [48].

Since the corrosion currents created by an ICCP system are distributed continuously in the surrounding fluid, finite difference methods (FDM) were employed in earlier numerical corrosion simulations. Difficulties in modeling oddly shaped structures soon made a finite element method (FEM) preferable [34, 49, 50], but while this avoids certain difficulties posed by FDM, both the FDM and FEM still require the modeling of an often large volume of electrolyte [45]. More recently it was shown that a boundary element method (BEM) could be used [51]. This approach reduces the problem to a surface integral solution of Laplace's equation on the electrolyte boundary. In typical problems of interest, where a structure is surrounded by a volume of electrolyte many times greater than itself, this method dramatically reduces the number of unknowns required for an accurate solution.

The complex chemistry of the corrosion reactions taking place at cathodic surfaces implies, in general, nonlinear boundary conditions in the BEM problem. For a given metal under given conditions, the current entering or leaving the metal is determined by its potential difference relative to the other electrodes. This relation is plotted in a *polarization curve* relating the normal current density on the surface

to the surface potential taken relative to some reference electrode [52]. The relation is usually determined experimentally, and is in general nonlinear and often complicated [53,54]. A simple iterative method for solving such problems is presented in [34]. More sophisticated approaches using the Newton-Raphson method, either by itself or in combination with other approaches, are described in [55]. In many practical problems, nonlinear boundary conditions are only found over relatively small portions of the surface of interest, allowing for various techniques to be used to reduce the computational expense of the iterative procedure [55,56]. It has also been shown that the fast multipole method (FMM) can be used to reduce computation time significantly [57].

In Chapter 4, a high-order locally corrected Nyström method is used to discretize the popular BEM solution to the electrostatic problem. A derivation of the surface integral equation from Laplace's equation in a homogeneous electrolyte is given for both exterior and interior problems. The degree to which different boundary conditions determine a unique solution is then discussed. Iterative solution of problems with nonlinear boundary conditions is addressed, and a technique that uses the Schur complement to improve the efficiency of the Newton-Raphson iterative method is presented.

1.2.2 Prediction of Corrosion-Related Magnetic Fields

While the electric potential and currents can be predicted using boundary element methods, the calculation of the corrosion-related magnetic (CRM) fields is often carried out using finite-element techniques [48,58]. An alternative to this computationally expensive approach is to approximate the field in medium and far regions by replacing the structure with a set of discrete current monopole sources [58]. This method is efficient and can produce accurate results at some distance from the hull.

It is shown in [59] that the volume integral form of the Biot-Savart law used to compute the field due to the distributed corrosion currents in the seawater can be reduced to an integral over the electrolyte boundary. This method, which directly makes use of the electric potential found in the electrostatic solution, is applied in [60]. A similar method using the electric field on the boundary is shown in [61]. While this type of approach is straightforward and accurate when the hull is surrounded by an infinite medium, difficulties arise when the hull is in a semi-infinite conducting region. The image techniques used to compute the electric fields [62] cannot be used to calculate the magnetic fields, and so in problems with semi-infinite electrolytes, as, for example, in the case of ships floating on the water surface, the electrolyte must be truncated at some depth and at some lateral distance from the ship. The resulting mesh, composed of the submerged portion of the structure, the water surface, and the imaginary box bounding the electrolyte, is treated as an interior boundary-element problem. The inclusion of the surfaces besides the submerged structure surface causes a significant increase in the number of unknowns in the problem, especially since the bounding box must often be made quite large to reduce the errors due to truncation of the electrolyte.

In Chapter 5, calculation of the corrosion-related magnetic fields is addressed, particularly computation from the surface potential solution to Laplace's equation. A simple method of approximating the magnetic field using discrete monopole sources, as in [58], is also briefly discussed, and results are compared for a discrete-source computation and a surface-integral computation of the CRM fields in a benchmark problem. A technique is presented for approximating the field due to an unspecified ICCP current within the hull or structure. A technique for calculating fields in a semi-infinite electrolyte without increasing the number of unknowns in the system solution is also discussed and validated.

CHAPTER 2. Construction of Highly Orthogonal Basis Functions for Volume Integral Equations Using the Singular Value Decomposition

Moment method solutions of integral equations in computational electromagnetic simulations generally approximate physical quantities according to well-defined, often simple, basis functions defined over mesh cells that approximate a given structure or its boundary. In general, greater accuracy can be obtained either by refining the mesh or by increasing the order of the functions used to model the unknowns. While both methods allow for more precise capturing of the small variations in the unknown quantities within a given part of the structure, mesh refinement tends to require a greater number of unknowns for a given degree of accuracy [33]. The resulting expenses in time and computer memory can make it impractical to achieve a desired accuracy for certain large problems. On the other hand, high-order basis functions can be difficult to implement for certain geometry types and can result in a poorly conditioned system matrix, making the use of fast solvers impractical [11].

Various methods have been presented for construction of well-conditioned high-order basis functions, as in [10]. A recently proposed approach constructs basis functions numerically by solving a system of constraint equations on mesh cells or cell pairs. This technique has been applied to quadrilateral [11] and triangular mesh elements [15]. These basis functions have been shown to slow the growth of the condition number with basis order when compared to other popular high-order basis sets while achieving essentially the same accuracy. The method has also been applied to volume bases on hexahedral elements [18]. Volume bases are of interest in this paper since they allow for a divergence-conforming representation of

magnetization and electric current in quasi-magnetostatic problems. Particularly when eddy currents are involved, this makes possible high-order modeling of currents without significantly degrading system conditioning and without the need for extra degrees of freedom to represent charge accumulation at mesh interfaces where no material discontinuity exists. In this chapter the numerical construction of divergence-conforming basis functions of arbitrary order is described in detail for hexahedral volume elements. In Chapter 3 is investigated the application of these bases to quasi-magnetostatic problems with eddy currents.

2.1 High-Order Divergence-Conforming Basis Functions

For integral equation solutions of scattering problems using such formulations as the electric field integral equation (EFIE) or equation (2.16) below, the presence of the divergence operator makes it desirable to model quantities such as currents or fields with basis functions that have a finite divergence. This implies that they should be normally continuous across interfaces where no physical discontinuity exists. Failure to meet this condition can affect the accuracy of the solution.

2.1.1 Definitions

In this section is defined the coordinate and geometric notation for the volume basis functions presented below, as well as the terminology used for basis function types.

2.1.1.1 Coordinate and Geometry Notation

Figure 2.1 illustrates the parametric coordinate system as well as the face labeling used in this paper to describe basis functions on hexahedral mesh cells. As

indicated in the figure, each of the three *independent* coordinates $u^i, i = 1, 2, 3$ corresponds to a *dependent* coordinate $u^{i+3} = 1 - u^i$. In this chapter index arithmetic with coordinates is understood to be modulo 6.

2.1.1.2 Face Basis Functions

For vector basis functions modeling vector quantities that pass between adjacent cells, e.g., electric or magnetic currents, it is useful to have a basis function with support on two cells so that such quantities may be modeled continuously. These bases, called *face* basis functions here, model a vector quantity whose normal component is continuous at the boundary between two adjacent cells. The face basis has an identically zero normal component at all non-shared faces of the two cells on which it has support, but is not identically zero on the shared face. For general hexahedral cells, a basis is computed in terms of each cell's parameterized coordinates, so that a basis $\mathbf{B}$ with support on the adjacent cells V_m and V_n would be written as

$$\mathbf{B}(\mathbf{r}) = \begin{cases} \mathbf{B}_m(\mathbf{r}) & \mathbf{r} \in V_m \\ \mathbf{B}_n(\mathbf{r}) & \mathbf{r} \in V_n \end{cases}. \tag{2.1}$$

The divergence-conforming constraint on $\mathbf{B}_m$ is then expressed as

$$\mathbf{B}_m(\mathbf{r}) \cdot \hat{\mathbf{n}} = \begin{cases} \mathbf{B}_n(\mathbf{r}) \cdot \hat{\mathbf{n}} & \mathbf{r} \in \partial V_m \cap \partial V_n \\ 0 & \mathbf{r} \in \partial V_m \backslash \partial V_n \end{cases} \tag{2.2}$$

where $\hat{\mathbf{n}}$ is normal to the boundary ∂V_m of V_m at $\mathbf{r}$. Switching m and n in (2.2) gives the constraint on $\mathbf{B}_n$.

2.1.1.3 Half Basis Functions

At certain interfaces, the normal continuity of face bases is not appropriate. For example, if two adjacent cells, each homogeneous, differ in relative permittivity ϵ_r, this can cause a discontinuity in the polarization current normal to the interface. Modeling such a discontinuous current requires bases that are not continuous at the shared face. These functions, termed *half* bases here, are still constrained to have a zero normal component at all but one face, but differ from the face bases defined above in that no constraint is applied at the remaining face. Thus they need not be defined with reference to two adjacent cells, and in fact will often be applied to faces on mesh boundaries where there is no adjacent cell. Half bases are defined by the property

$$\mathbf{B}_m(\mathbf{r}) \cdot \hat{\mathbf{n}} = 0, \mathbf{r} \in \partial V_m \backslash S \tag{2.3}$$

where S is the face at the material discontinuity or mesh boundary. A simple half basis is illustrated in Fig. 2.3.

2.1.1.4 Volume Basis Functions

In order to model components of vector quantities that do not flow across cell boundaries, we make use of another type of basis function, called a *volume* basis function here. An example of a hexahedral volume basis is shown in Fig. 2.4, and the defining property can be expressed as

$$\mathbf{B}_m(\mathbf{r}) \cdot \hat{\mathbf{n}} = 0, \mathbf{r} \in \partial V_m. \tag{2.4}$$

2.1.2 Numerical Construction of Constrained Basis Functions

The hexahedral basis functions used for volume integral equations in this paper are expressed in terms of the parametric coordinates (u^1, u^2, u^3) described in Fig. 2.1

and the corresponding unitary vectors [63, Chapter I] defined by

$$\mathbf{a}_i = \frac{\partial \mathbf{r}}{\partial u^i}. \tag{2.5}$$

This allows for the bases on a cell to be separated into three independent sets, one in each coordinate direction. Let the qth basis function on cell V_m pointing in the direction of $\mathbf{a}_i$, denoted here by $\mathbf{B}_m^{q,i}$, be given by

$$\mathbf{B}_m^{q,i} = B_m^{q,i}(u^1, u^2, u^3)\mathbf{a}_i. \tag{2.6}$$

In most cases, $B_m^{q,i}$ would be given some definite, predetermined form. The interpolatory basis functions in [33] are a good example of this. In the basis functions presented here, the form of $B_m^{q,i}$ is not given an analytic definition but rather is derived numerically to satisfy the conditions in Section 2.1.1.

A detailed algebraic treatment of basis functions of the form (2.6) suitable for a charge representation [64] polynomial complete to order p is given in Appendix A. It is found that $(p+1)^2$ basis functions are associated with each hexahedral face and that $3p(p+1)^2$ bases are associated with each volume.

While all basis function sets fitting the general description above will allow for an essentially equivalent representation, certain basis sets can yield better-conditioned systems more amenable to solution by certain fast solvers. Various highly-orthogonal basis function sets have been proposed, such as those presented in [9] and [10]. An alternative approach is to construct bases of the form (2.6) numerically in a way that satisfies a given set of constraints such as divergence-conformity while still achieving, as far as cell geometry allows, mutual orthogonality among basis functions. The numerical construction of high-order divergence-conforming basis functions using the singular value decomposition (SVD) has been

detailed for quadrilateral mesh elements in [11, 12, 14, 31]. Volume bases for hexahedral cells can be constructed in a closely analogous way [18]. As in the quadrilateral case, the desired basis constraints (divergence-conformity here) are expressed as an underdetermined system of equations whose unknowns are weighting coefficients for an underlying set of generating functions. An orthonormal set of basis coefficients satisfying the constraints is then found by taking the SVD of the constraint matrix.

2.1.3 Basis Coefficient Calculation

To construct the bases numerically, we impose the constraints discussed above in systems of equations, just as for the quadrilateral bases in [11,12]. Any polynomial $f(u^i, u^j, u^k)$ that has real coefficients and is of degree not greater than p_ℓ in u^ℓ, can be specified by $(p_i+1)(p_j+1)(p_k+1)$ coefficients. For the function to be completely determined on a face F_i or F_{i+3}, it must be specified at $(p_j+1)(p_k+1)$ distinct points on that face. The use of the unitary vector $\mathbf{a}_i$ in the basis definition ensures that bases in the direction of $\hat{\mathbf{a}}_i$ will have a zero normal component on all faces besides F_i and F_{i+3}. In the representation discussed here, this means that for the qth basis $\mathbf{B}_m^{q,i} = B_m^{q,i}\mathbf{a}_i$ the constraints in (2.2), (2.3) and (2.4) are applied as appropriate to a grid of $(p+1)^2$ points on each of the faces F_i and F_{i+3} of cell m. An evenly spaced $(p+1) \times (p+1)$ grid is a good choice.

We pick a set of $p+2$ independent polynomials $\{F_n^1\}$ of degree not greater than $p+1$, and $p+1$ independent polynomials $\{F_n^2\}$ of degree not greater than p. We can therefore write our basis $B_m^{q,i}$ as

$$B_m^{q,i} = \sum_{r=0}^{p+1}\sum_{s=0}^{p}\sum_{t=0}^{p} \beta_{rst} F_r^1(u^i) F_s^2(u^j) F_t^2(u^k) \tag{2.7}$$

where the coefficients β_{rst} are unknown real weights. By imposing the condition

$$\sum_{r=0}^{p+1}\sum_{s=0}^{p}\sum_{t=0}^{p}\beta_{rst}\left[F_r^1(u^i)F_s^2(u^j)F_t^2(u^k)\hat{\mathbf{n}}(\mathbf{r})\cdot\mathbf{a}_i(\mathbf{r})\right]=0 \tag{2.8}$$

over a grid of $(p+1)\times(p+1)$ points on faces where $\mathbf{B}_m^{q,i}\cdot\hat{\mathbf{n}}=0$ and

$$\begin{aligned}&\sum_{r=0}^{p+1}\sum_{s=0}^{p}\sum_{t=0}^{p}\beta_{rst}^m\left[F_r^1(u^{i_m})F_s^2(u^{j_m})F_t^2(u^{k_m})\hat{\mathbf{n}}(\mathbf{r})\cdot\mathbf{a}_{i_m}(\mathbf{r})\right]\\&-\sum_{r=0}^{p+1}\sum_{s=0}^{p}\sum_{t=0}^{p}\beta_{rst}^n\left[F_r^1(u^{i_n})F_s^2(u^{j_n})F_t^2(u^{k_n})\hat{\mathbf{n}}(\mathbf{r})\cdot\mathbf{a}_{i_n}(\mathbf{r})\right]=0\end{aligned} \tag{2.9}$$

on faces where (2.2) must be satisfied, we create a system of $N_F(p+1)^2$ equations where the number of faces N_F is 1 for half bases, 2 for volume bases, and 3 for face bases. The number of unknowns β is $N_V(p+2)(p+1)^2$ where the number of cells N_V is 1 for half and volume bases and 2 for face bases. If the functions $\{F\}$ and the grid are properly chosen, the equations will be independent, and the entire system will have a null space of dimension $(p+1)^3$ for face and half bases and $p(p+1)^2$ for volume bases.

The null space is found computationally by use of the singular value decomposition (SVD)

$$[C]=[U][\Sigma][V]^T \tag{2.10}$$

which allows a matrix $[C]$ to be expressed in terms of unitary matrices $[U]$ and $[V]$ and a diagonal matrix $[\Sigma]$ of *singular values*. Columns in $[U]$ corresponding to *nonzero* singular values in $[\Sigma]$ make up a basis for the range of $[C]$, while columns in $[V]$ corresponding to *zero* singular values in $[\Sigma]$ form a basis for the null space of $[C]$. By expressing (2.8) and (2.9) in terms of matrix equations and taking the SVD, we find a set of orthogonal vectors in the appropriate columns of V satisfying our requirement for the coefficients β. The technique is exactly analogous to that used

for quadrilaterals in [11,12].

Note that the volume basis space is a subspace of the face and half basis spaces, but redundancy can be avoided by projecting the face and half basis coefficient spaces onto the volume basis spaces and subtracting this projection. Let $[V'_{mn}]$ be the $2(p+2)(p+1)^2 \times (p+1)^3$ matrix whose columns form a basis for the null space of the face basis constraint matrix for the face shared by the mth and nth cells. Let $[V'_m]$ and $[V'_n]$ be the $(p+2)(p+1)^2 \times p(p+1)^2$ matrices containing, respectively, the null space of the volume constraint matrices for the mth and nth cells in the relevant direction. (The row ordering is assumed to be such that the kth row in $[V'_{mn}]$ and the kth row in $\begin{bmatrix}[V'_m] \\ [V'_n]\end{bmatrix}$ both correspond to the same basis coefficient.) Now remove the projection of $[V'_{mn}]$ onto the volume subspaces:

$$[P] = \left(I - \begin{bmatrix}[V'_m] & [0] \\ [0] & [V'_n]\end{bmatrix} \begin{bmatrix}[V'_m]^T & [0] \\ [0] & [V'_n]^T\end{bmatrix} \right) [V'_{mn}].$$

Removing the volume basis subspaces results in the $2(p+2)(p+1)^2 \times (p+1)^3$ matrix $[P]$ being rank deficient, and so we take another SVD

$$[P] = [U^P][\Sigma^P][V^P].$$

Now the vectors in $[U^P]$ corresponding to *non*zero singular values in $[\Sigma^P]$ give us a set of $(p+1)^2$ coefficient vectors for face bases that exclude the volume basis spaces. The process is essentially identical to that detailed for quadrilateral bases in [12,14].

Proper selection of the functions F is important in constructing basis functions for well-conditioned systems. The shifted Legendre polynomials P_ℓ defined on the

interval $[0, 1]$ are a good choice because of their mutual orthogonality

$$\langle P_m(x), P_n(x)\rangle = \int_0^1 P_m(x) \cdot P_n(x)dx = \begin{cases} \frac{1}{2n+1} & m = n \\ 0 & m \neq n \end{cases}. \tag{2.11}$$

Defining the scaled Legendre polynomials $\tilde{P}_\ell$ as

$$\tilde{P}_\ell(x) = \sqrt{2\ell + 1}P_\ell(x) \tag{2.12}$$

and applying (2.11) gives

$$\left\langle \tilde{P}_m(x), \tilde{P}_n(x)\right\rangle = \begin{cases} 1 & m = n \\ 0 & m \neq n \end{cases}. \tag{2.13}$$

For the scattering problems considered in this paper, we construct our bases as

$$\mathbf{B}^i(u^i, u^j, u^k) = \frac{\mathbf{a}_i}{\mathcal{J}} \sum_{r=0}^{p+1} \sum_{s=0}^{p} \sum_{t=0}^{p} \beta_{rst} \tilde{P}_r(u^i)\tilde{P}_s(u^{i+1})\tilde{P}_t(u^{i+2}) \tag{2.14}$$

where $\mathcal{J} = (\mathbf{a}_{i+1} \times \mathbf{a}_{i+2}) \cdot \mathbf{a}_i$ is the cell Jacobian.

2.2 Numerical Test Results

Below are shown computational results for the basis functions described above implemented in a moment method code to solve electromagnetic scattering problems with a volume integral equation.

2.2.1 Basis Properties

First we take a look at the computational and numerical properties of the basis functions. The time complexity of basis construction is addressed, and the mutual

orthogonality of bases and the strong diagonal produced are illustrated by analysis of Gram matrices for cubic and skewed hex cells.

2.2.1.1 Computation Time

The most time-consuming operation in the basis coefficient computation process is the singular value decomposition, which for a $m \times n$ matrix with $m \leq n$ has a complexity of around $O(n^3)$ [65]. The constraint matrices give $m = O(p^2)$ and $n = O(p^3)$. This leads to an overall time complexity of about $O(p^{8.5})$ to $O(p^9)$, as shown in Fig. 2.5.

In this context, the presence of $\mathcal{J}$ in (2.14) makes the basis functions independent of the particular cell geometries, since on a shared face the corresponding transverse unitary vectors $\mathbf{a}_{i+1}$ and $\mathbf{a}_{i+2}$ will be identical for both adjacent cells, so that

$$\frac{\hat{\mathbf{n}} \cdot \mathbf{a}_i}{\mathcal{J}} = \frac{\hat{\mathbf{n}} \cdot \mathbf{a}_i}{(\mathbf{a}_{i+1} \times \mathbf{a}_{i+2}) \cdot \mathbf{a}_i} = \frac{\hat{\mathbf{n}} \cdot \mathbf{a}_i}{|\mathbf{a}_{i+1} \times \mathbf{a}_{i+2}| \hat{\mathbf{n}} \cdot \mathbf{a}_i} = \frac{1}{|\mathbf{a}_{i+1} \times \mathbf{a}_{i+2}|}. \tag{2.15}$$

In the conformal mesh required for the technique as presented here, this quantity is the same for both cells at a shared interface.

Although the above consideration renders the recalculation of basis coefficients for each cell or cell pair redundant in this context, the numerical timing test results in Fig. 2.5 still use this recalculation to show the potential time complexity to be expected in formulations that would require recalculation. While the basis construction time becomes more perceptible at very high basis orders (e.g. $p = 12, 13$), it remains small when compared to overall simulation times, and is negligible at lower orders.

2.2.1.2 Gram Matrices

While the high mutual orthogonality of the proposed basis functions on right hexahedral cells can be known *a priori*, it may be helpful to see it graphically illustrated as in Fig. 2.7. The color plots shows the normalized magnitude of the entries in the Gram matrix $[G]$ with $[G]_{i,j} = \langle \mathbf{B}_i, \mathbf{B}_j \rangle$, computed for bases numerically constructed as above using both the normalized and unnormalized Legendre polynomials, as well as the interpolatory bases described in [33]. The effect of the scaling of the Legendre polynomials indicates the importance of the choice of generating function set $\{P\}$. We see moreover the strong diagonal maintained by the numerically constructed bases even when the cell is skewed. The skewed hex geometry is shown in Fig. 2.6, and the vertex coordinates are given in Table 2.1.

The almost entirely diagonal matrix produced in Fig. 2.7f when the scaled Legendre polynomials are used leads one to speculate on the possibility of using this method to construct an entirely orthogonal basis set. The off-diagonal nonzero blocks are due to the face bases on opposite faces of the same cell, which are not mutually orthogonal even on right-angled cells. One sees on examination that to orthogonalize them completely would introduce a dependence of face bases for one cell not only on the adjacent cells but on cells directly beyond those cells in the direction of both the shared face and its opposite. Moreover, in a mesh containing skewed or curvilinear elements the mutual orthogonality of the unitary vectors is lost, and so generating a complete set of wholly orthogonal bases by the above method would require the singular value decomposition of a global coefficient matrix.

2.2.2 Volume Integral Equation for Dielectric Scattering Problems

Time-harmonic electromagnetic scattering from dielectric bodies using volume integral techniques is discussed in [4]. Using the volume equivalence principle [66]

gives an equation relating an incident field $\mathbf{E}^i$ to an induced volume polarization current $\mathbf{J}$. For a body V with permittivity ϵ surrounded by infinite open space, we have

$$\begin{aligned}\mathbf{E}^i(\mathbf{r}) = \frac{1}{j\omega(\varepsilon-\varepsilon_0)}\mathbf{J}(\mathbf{r}) + j\eta_0 k_0 \int_V \frac{e^{-jk_0|\mathbf{r}-\mathbf{r}'|}}{4\pi|\mathbf{r}-\mathbf{r}'|}\mathbf{J}(\mathbf{r}')\,dV' \\ + j\frac{\eta_0}{k_0}\boldsymbol{\nabla}\int_V \frac{e^{-jk_0|\mathbf{r}-\mathbf{r}'|}}{4\pi|\mathbf{r}-\mathbf{r}'|}\boldsymbol{\nabla}'\cdot\mathbf{J}(\mathbf{r}')\,dV',\ \mathbf{r}\in V.\end{aligned} \tag{2.16}$$

Here η_0, ϵ_0, and k_0 are the intrinsic impedance, permittivity, and wave number in free space, respectively. The $\boldsymbol{\nabla}\cdot\mathbf{J}$ term makes it desirable to represent $\mathbf{J}$ with divergence-conforming basis functions, since otherwise discontinuities at cell interfaces where no physical discontinuity exists may need to be modeled as separate degrees of freedom. In what follows we use the basis functions described above in a moment method [67] code to solve (2.16). Error convergence plots give the relative root-mean-square (RMS) error of the computed solution $\{c_n\}$ with respect to a reference solution $\{a_n\}$

$$\text{Error}_{RMS} = \sqrt{\frac{\sum_n |c_n - a_n|^2}{\sum_n |a_n|^2}} \tag{2.17}$$

2.2.3 Layered Dielectric Sphere

A 3-layer $1\,\text{m}$-radius sphere whose relative permittivity $\epsilon_r = \frac{\epsilon}{\epsilon_0}$ is given by

$$\epsilon_r(r) = \begin{cases} 2.0 & r < 0.3\,\text{m} \\ 4.0 & 0.3 < r < 0.7\,\text{m} \\ 8.0 & 0.7 < r < 1.0\,\text{m} \end{cases} \tag{2.18}$$

is simulated and compared to the analytic solution [68]. Figure 2.8 shows the relative RMS error of the resulting scattering cross section and shows the increasing

rate of convergence with basis order as well as the higher accuracy attainable with higher-order bases with a comparable number of unknowns. In Fig. 2.9 the relative RMS error is plotted versus the maximum edge length h in the mesh, and the exponential convergence rates h^{α} are given.

2.2.4 Dielectric Cube

In order to gauge the effect of sharp edges on the performance of the numerically constrained basis functions, a $1\,\mathrm{m}$ cube with relative permittivity $\epsilon_r = 8.0$ is illuminated by a $50\,\mathrm{MHz}$ plane wave traveling normal to one of its faces. It is compared against a surface integral equation solution discretized with 33,750 quadrilaterals using the Müller formulation [69]. As is also observed in the surface integral case [11, 14], the convergence of the scattering cross section is not as rapid as that of the smooth sphere, but it still converges steadily with both basis order and mesh refinement.

2.2.5 Dielectric Shell

Figure 2.11 shows the system condition number for a dielectric shell with inner radius $0.9\,\mathrm{m}$ and outer radius $1.0\,\mathrm{m}$. As in Section 2.2.1.2, we see not only that the numerically constrained bases give better conditioning than the interpolatory set presented in [33] but also that the normalization of the Legendre polynomials lowers both the condition number and its rate of increase with basis order.

2.3 Summary

In this chapter we have looked at the construction and performance of numerically constrained divergence-conforming basis functions for hexahedral mesh elements.

The numerically constructed bases show higher-order error convergence for scattering problems involving both homogeneous and layered scatterers, and they significantly diminish the value and growth rate of the system matrix condition number. So far we have examined only the application of these bases to high-frequency problems. In the following chapter, we investigate their use in problems involving magnetic and conducting materials at low frequencies.

TABLE 2.1: Vertex coordinates (in meters) for skewed hex used in Gram matrix comparison.

Vertex	x	y	z
V_1	-0.50	-0.50	+0.50
V_2	-0.60	-0.40	-0.70
V_3	-0.50	+0.50	+0.50
V_4	-0.40	+0.30	-0.50
V_5	+0.50	-0.50	+0.50
V_6	+0.50	-0.50	-0.50
V_7	+0.55	+0.30	+0.40
V_8	+0.45	+0.65	-0.50

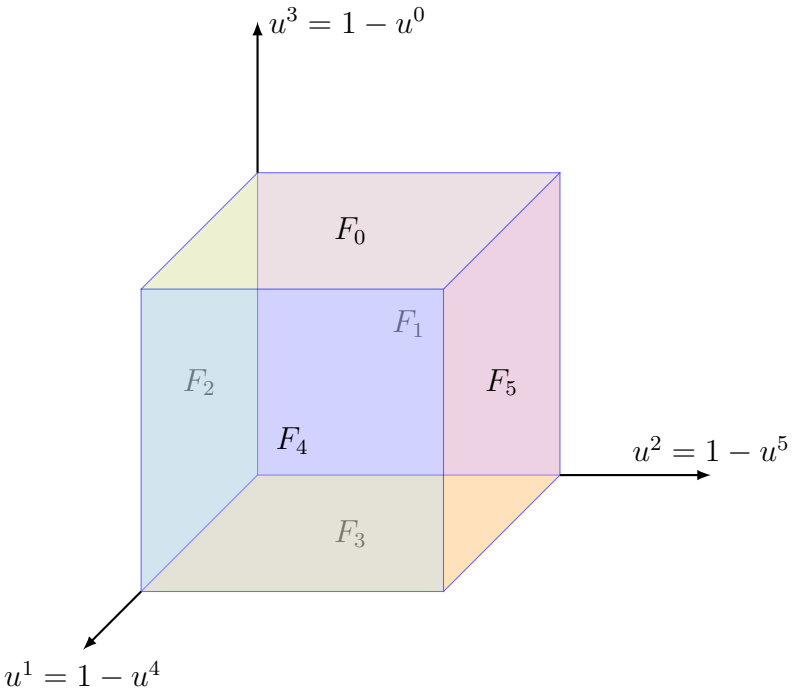

FIGURE 2.1: Coordinate and face labeling on reference hex cell. F_i is defined by $u^i = 0$.

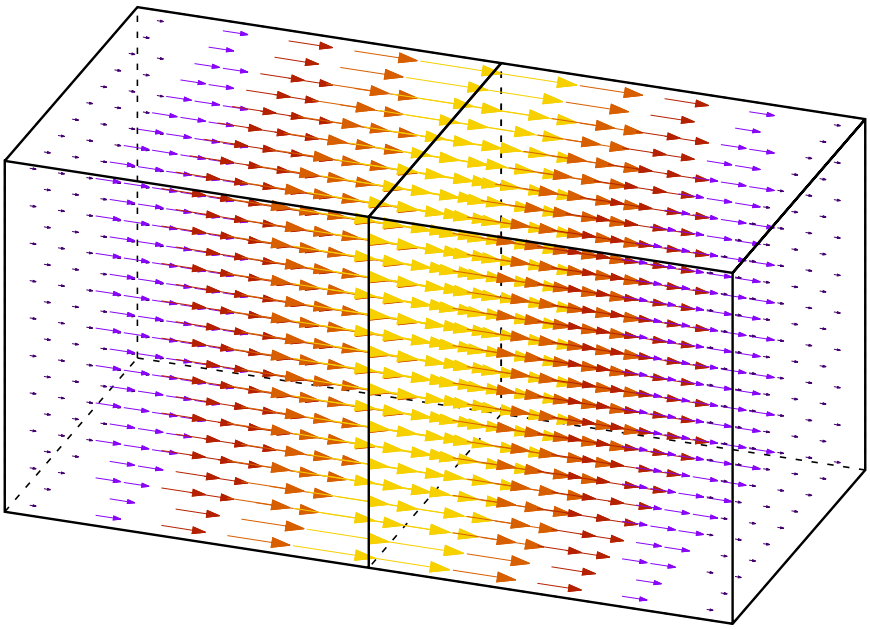

FIGURE 2.2: Illustration of face basis function.

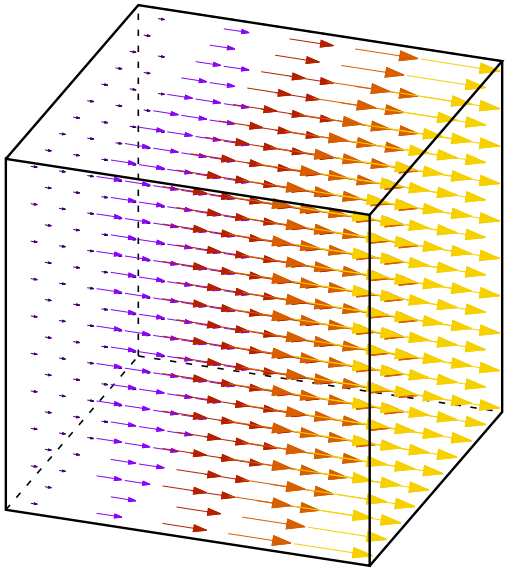

FIGURE 2.3: Illustration of half basis function.

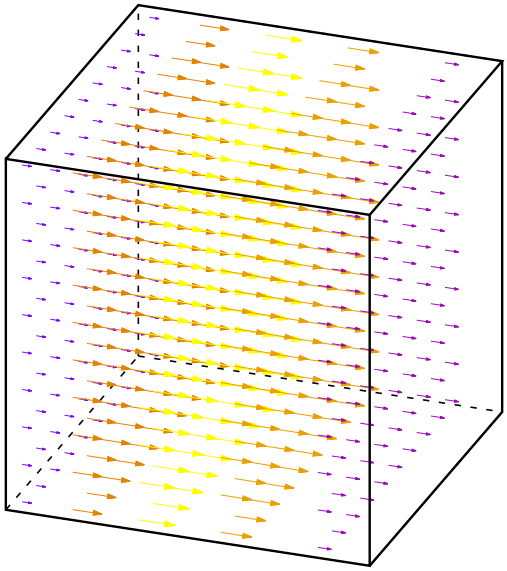

FIGURE 2.4: Illustration of volume basis function.

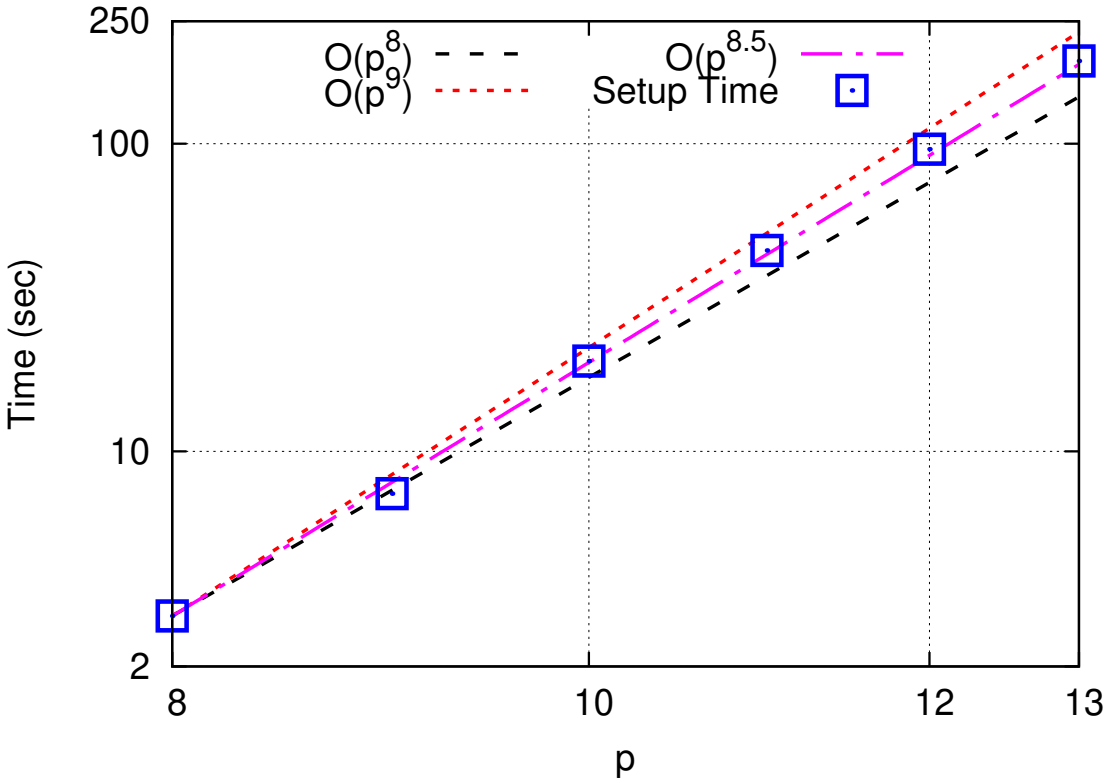

FIGURE 2.5: Constrained basis coefficient computation time versus basis order p for single hex cube.

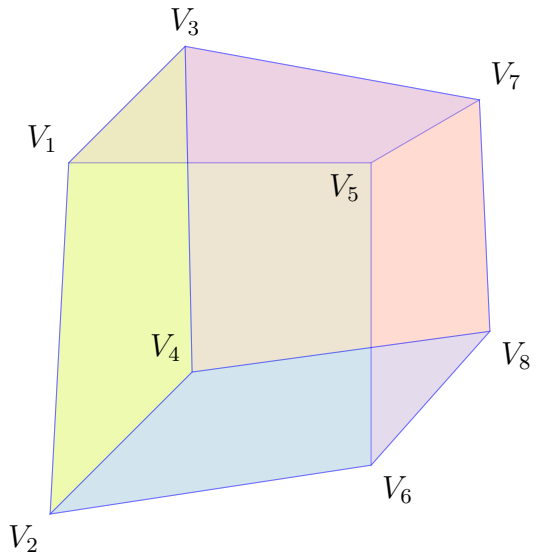

FIGURE 2.6: Skewed hexahedral cell used for Gram matrix comparison.

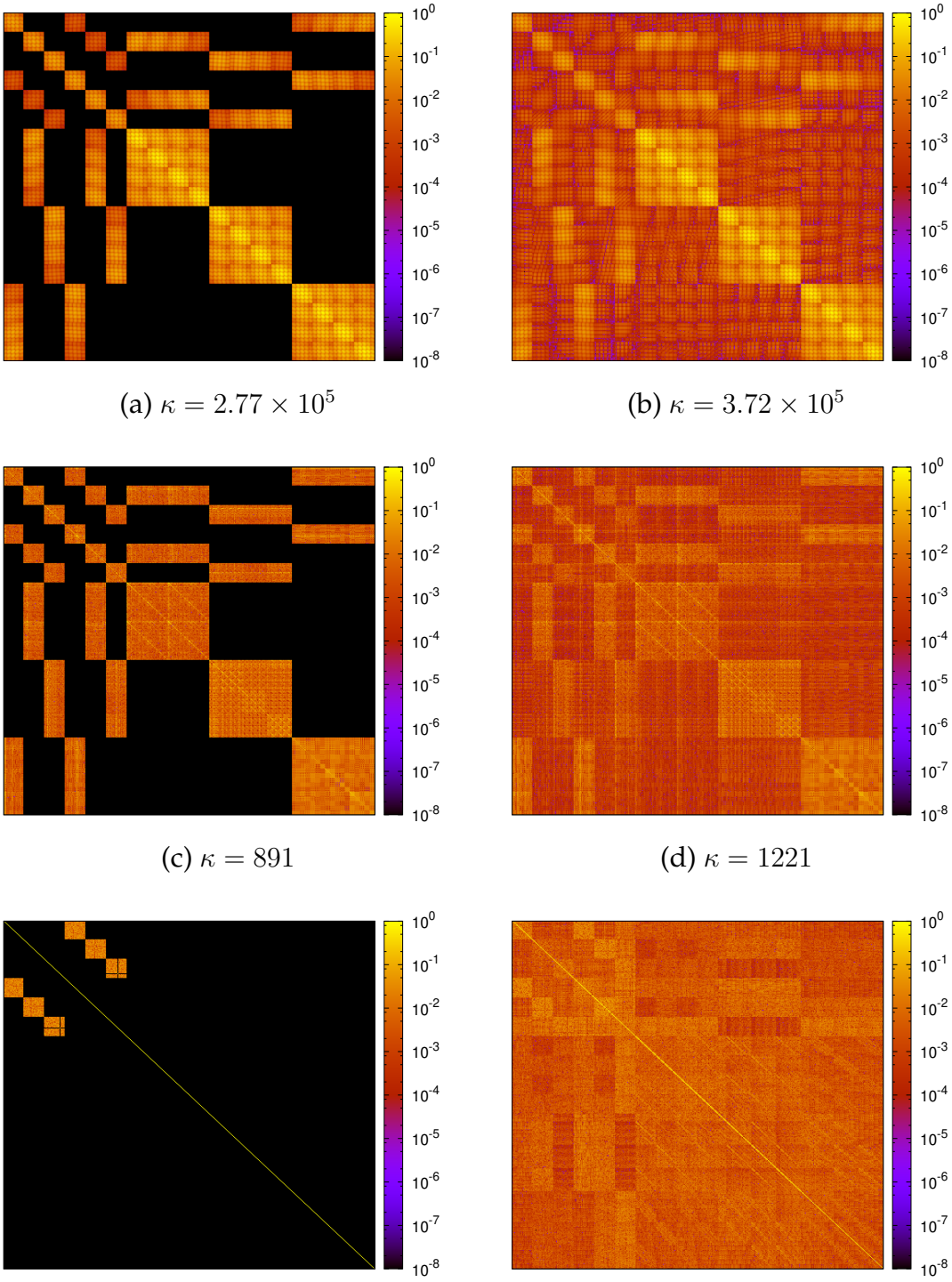

(a) $\kappa = 2.77 \times 10^5$ (b) $\kappa = 3.72 \times 10^5$

(c) $\kappa = 891$ (d) $\kappa = 1221$

(e) $\kappa = 1.4$ (f) $\kappa = 5.47$

FIGURE 2.7: Basis Gram matrices with condition number κ for cubic hex (a,c,e) and skewed hex (b,d,f) using interpolatory bases (a,b), numerically constrained bases (c,d), and scaled numerically constrained bases (e,f). Integration tolerance is 10^{-6}.

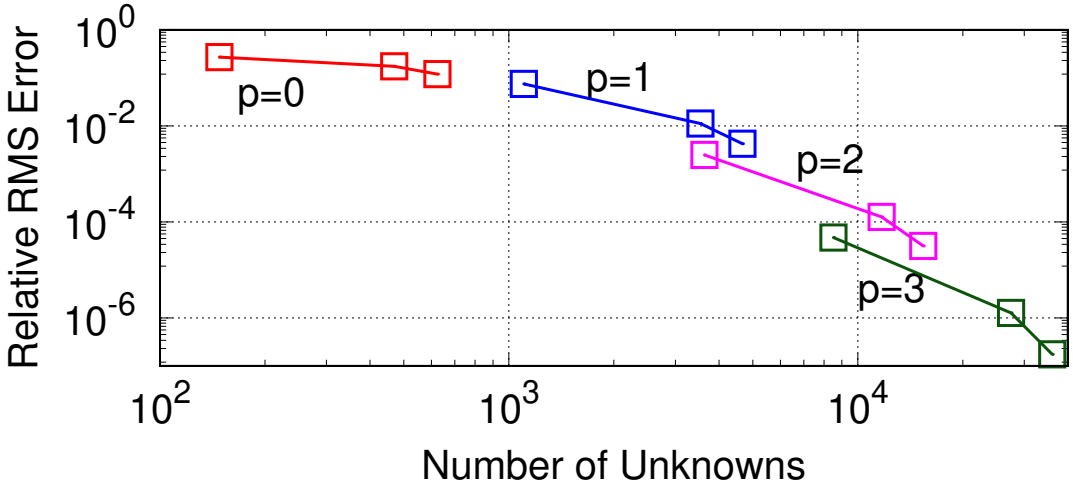

FIGURE 2.8: Relative RMS error of scattering cross section for a layered sphere with radius $1\,\mathrm{m}$ at $50\,\mathrm{MHz}$, plotted versus number of unknowns. Integration tolerance is 10^{-6}.

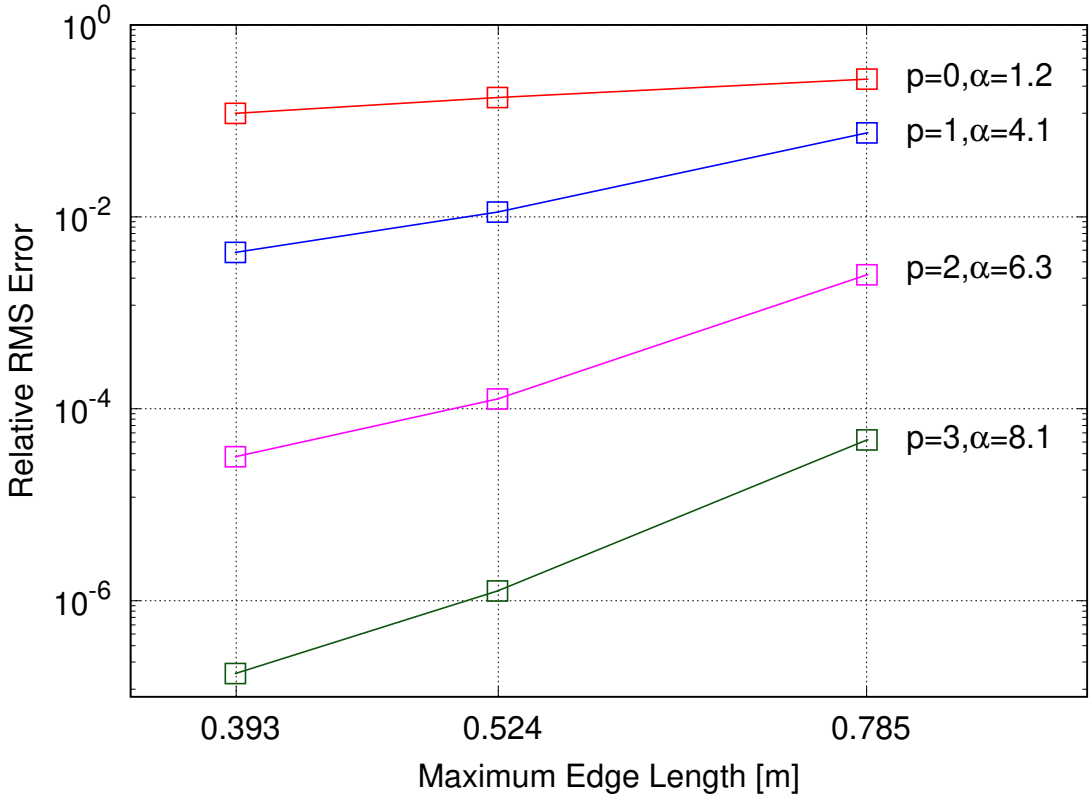

FIGURE 2.9: Relative RMS error of scattering cross section for a layered sphere with radius $1\,\mathrm{m}$ at $50\,\mathrm{MHz}$, plotted versus maximum cell edge length. Integration tolerance is 10^{-6}.

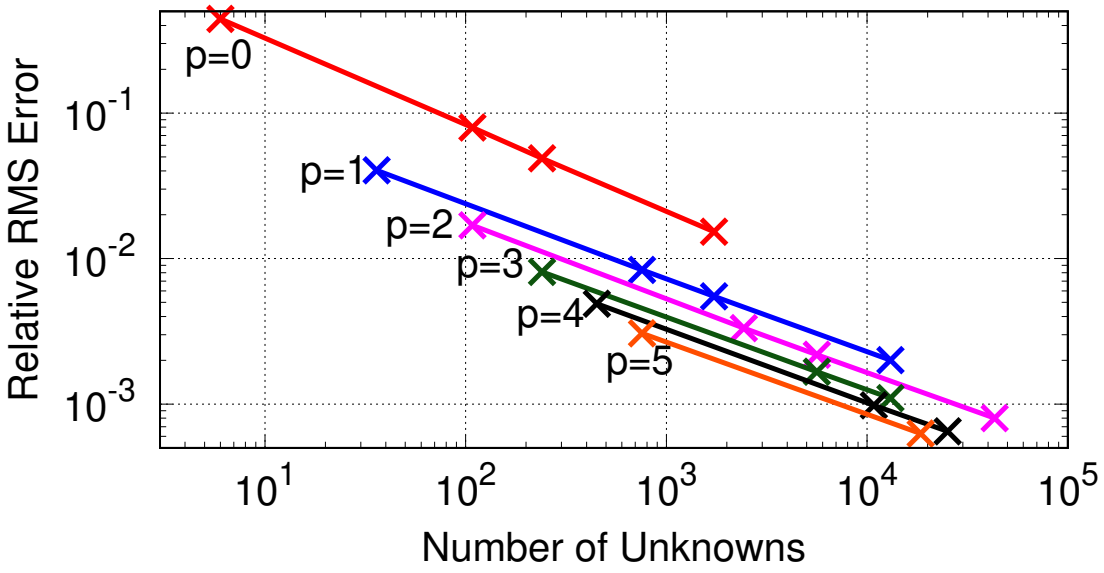

FIGURE 2.10: Relative RMS error of scattering cross section for $1\,\mathrm{m}$ dielectric cube, $\epsilon_r = 8.0$, at $50\,\mathrm{MHz}$. Integration tolerance is 10^{-6}.

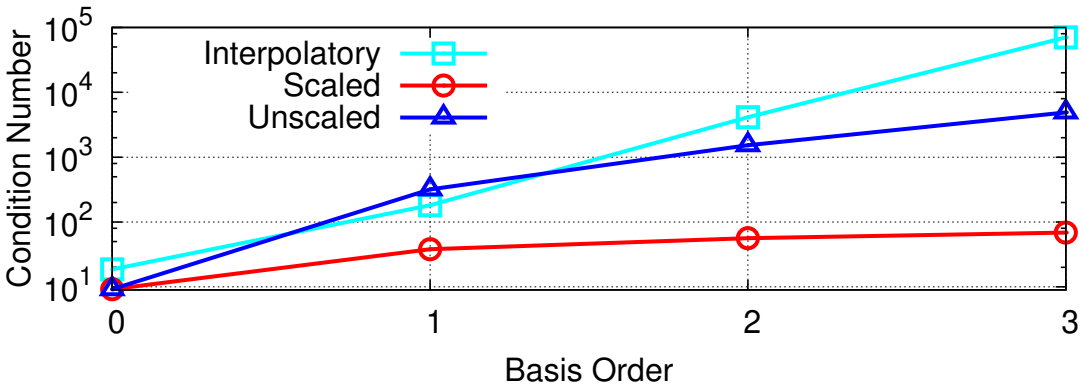

FIGURE 2.11: System matrix condition number for dielectric shell problem with $\epsilon_r = 8.0$, inner radius $0.9\,\mathrm{m}$, outer radius $1.0\,\mathrm{m}$, meshed with 168 10th-order hex cells. Integration tolerance is 10^{-6}.

CHAPTER 3. Quasi-Magnetostatic Simulations Using Nyström-Moment Conversion with Constrained Basis Functions

The basis functions discussed in the previous chapter find application here in quasi-magnetostatic problems with eddy currents. Such problems often involve large meshes with many magnetic and conducting volume elements, as when the magnetic fields scattered by ships are analyzed. At the low frequencies that are often of interest in maritime problems, poor system matrix conditioning can be alleviated by using an augmented formulation [28], which can entail the modeling of both volume and surface charge densities as additional degrees of freedom.

The locally corrected Nyström (LCN) method used here to solve the integral equations has the advantage of simplicity in its straightforward computation of interactions between relatively distant points without the need for two-fold integrations over source and field cells. Unlike the method of moments (MoM) formulation used in Chapter 2, however, the Nyström method does not explicitly enforce normal current continuity at mesh interfaces, meaning that in certain situations non-physical boundary charges must be accounted for. Since the moment and Nyström methods are effectively equivalent by a linear transformation (cf. [31]), this discontinuity and the resulting fictitious boundary charge DoF can be eliminated by converting Nyström interaction blocks to MoM blocks, where the MoM basis functions are divergence-conforming, as in [12].

In this chapter is presented a general method for converting a high-order LCN matrix to a moment-method matrix. The application of this conversion to quasi-magnetostatic problems with eddy currents is then investigated, with numerical

results showing accuracy and system matrix conditioning for different problem geometries.

3.1 The Locally Corrected Nyström Method

A popular technique for solving integral equations numerically is the Nyström method, where interactions between parts of a structure are approximated by sampling at points on mesh cells. As with the moment method, a complicated problem involving unknown fields or currents is reduced to a finite number of interactions between known entities. In a moment-method solution, the interactions between known basis and test functions are calculated, and the unknowns are the weights of the basis functions. The interaction between a basis function B_n on a cell Ω_n and a test function T_m on a cell Ω_m is found (cf. [67]) by computing an integral such as

$$\int_{\Omega_m} T_m(\mathbf{r}) \int_{\Omega_n} K(\mathbf{r}, \mathbf{r}') B_n(\mathbf{r}') d\Omega' d\Omega$$

where K is the kernel relating sources at $\mathbf{r}'$ to fields at $\mathbf{r}$.

The Nyström approach specifies points on the mesh cells, and the unknowns are simply the values of the unknown quantities at these points. The interactions can be computed with a single evaluation of the kernel for each field and source point pair $(\mathbf{r}, \mathbf{r}')$, without the need for surface or volume integrals over both source and field cells. The Green's functions used for electromagnetic problems complicate the process since they are generally singular. To overcome this difficulty, we use the *locally corrected Nyström method* (LCN), described in [12, 13, 22], in which a special quadrature rule is calculated to handle the singular and near-singular interactions.

Let a potential or field $V(\mathbf{r})$ at a point $\mathbf{r}$ be related to sources $J(\mathbf{r}')$ on a cell Ω_n by

$$V(\mathbf{r}) = \int_{\Omega_n} J(\mathbf{r}')K(\mathbf{r}, \mathbf{r}')d\Omega'$$

the Nyström method uses the approximation

$$V(\mathbf{r}) \approx \sum_{i=1}^{N_q} J(\mathbf{r}_{q_n})K(\mathbf{r}, \mathbf{r}_{q_n})\omega_{q_n}\mathcal{J}(\mathbf{r}_{q_n})$$

where $\{\mathbf{r}_{q_n}\}$ and $\{\omega_{q_n}\}$ are the quadrature abscissae and weights (typically Gaussian) for numerical integration over Ω_n, and $\mathcal{J}(\mathbf{r}_{q_n})$ is the cell Jacobian at the qth quadrature point on cell n. The interaction between two quadrature points $\mathbf{r}_{q_m}$ on Ω_m and $\mathbf{r}_{q_n}$ on Ω_n is approximated as

$$Z_{m_q,n_q} = \omega_{q_n}K(\mathbf{r}_{q_m}, \mathbf{r}_{q_n})\mathcal{J}(\mathbf{r}_{q_n}) \tag{3.1}$$

when $\mathbf{r}_{q_m}$ on Ω_m and $\mathbf{r}_{q_n}$ are far from each other.

When $\mathbf{r}_{q_m}$ and $\mathbf{r}_{q_n}$ are not sufficiently separated, the quadrature rule must be corrected to handle the resulting singularity in K. Let Ω_n contain the field point $\mathbf{r}_{q_m}$. We can find an alternate set of weights $\{\tilde{\omega}_{q_n}\}$ on Ω_n to handle the singularity. Suppose J can be approximated on Ω_n by a linear combination of N_f functions $f_k, k = 1 \ldots N_f$. In effect, we want a set of N_{q_n} weights $\{\upsilon_{q_n}\}$ such that

$$\sum_{q_n=1}^{N_{q_n}} f_k(\mathbf{r}_{q_n})K(\mathbf{r}_{q_m}, \mathbf{r}_{q_n})\upsilon_{q_n}\mathcal{J}(\mathbf{r}_{q_n}) = \alpha_k \tag{3.2}$$

where

$$\alpha_k = \int_{\Omega_n} f_k(\mathbf{r}')K(\mathbf{r}_{q_m}, \mathbf{r}')d\Omega'. \tag{3.3}$$

This gives us a system of N_f equations in N_{q_n} unknowns, though it must be modified due to the singularity in the terms where $\mathbf{r}_{q_m} = \mathbf{r}_{q_n}$. Accordingly, we replace the terms $K(\mathbf{r}_{q_m}, \mathbf{r}_{q_n})\upsilon_{q_n}\mathcal{J}(\mathbf{r}_{q_m})$ with the unknowns $\tilde{\omega}_{q_n}$, which yields the system

$$\begin{bmatrix} f_1(\mathbf{r}_{1_n}) & \cdots & f_1(\mathbf{r}_{N_{q_n}}) \\ \vdots & \ddots & \vdots \\ f_{N_f}(\mathbf{r}_{1_n}) & \cdots & f_{N_f}(\mathbf{r}_{N_{q_n}}) \end{bmatrix} \begin{bmatrix} \tilde{\omega}_{1_n} \\ \vdots \\ \tilde{\omega}_{N_{q_n}} \end{bmatrix} = \begin{bmatrix} \alpha_1 \\ \vdots \\ \alpha_{N_f} \end{bmatrix} \tag{3.4}$$

which can be solved for a set of weights $\tilde{\omega}_{q_n}$. Thus if some weighted sum of $\{f_k^n\}$ can give a good approximation of J on Ω_n, then the convolution of J with K over Ω_n can be approximated with the values $\{\tilde{\omega}_{q_n}\}$ found by solving (3.4) as

$$\int_{\Omega_n} J(\mathbf{r}')K(\mathbf{r}_{q_m}, \mathbf{r}')d\Omega' \approx \sum_{q_n=1}^{N_{qn}} J(\mathbf{r}_{q_n})\tilde{\omega}_{q_n}. \tag{3.5}$$

Thus the interaction between $\mathbf{r}_{q_m}$ on Ω_n and another point $\mathbf{r}_{q_n}$ on Ω_n is calculated as

$$Z_{q_m,q_n} = \tilde{\omega}_{q_n}. \tag{3.6}$$

Note that in general each field point $\mathbf{r}_{q_m}$ will have its own set of adjusted quadrature weights $\{\tilde{\omega}_{q_n}\}$.

In the numerical tests run for this paper, the functions f are products of the shifted Legendre polynomials discussed in Chapter 2. As pointed out in [13], this results in the matrix in (3.4) being well-conditioned. Further details may be found in [13, 15].

3.2 Nyström-Moment Method Conversion

Solving an integral equation for an unknown function $J(\mathbf{r})$ with the Nyström method gives us the value of J sampled at a set of points $\mathbf{r}_n$. Thus an integral

equation

$$\int_{\Omega} J(\mathbf{r}')K(\mathbf{r},\mathbf{r}')d\Omega = V(\mathbf{r}) \tag{3.7}$$

can be approximated by the matrix equation

$$[Z^{LCN}] \cdot \bar{\beta}^{LCN} = \bar{V}^{LCN} \tag{3.8}$$

where the notation $\bar{A}$ denotes a column vector of values A_n and

$$[Z^{LCN}]_{mn} = \begin{cases} \omega_n K(\mathbf{r}_m,\mathbf{r}_n)\mathcal{J}(\mathbf{r}_n) & \mathbf{r}_m,\mathbf{r}_n \text{ not on same cell} \\ \tilde{\omega}_n & \mathbf{r}_m,\mathbf{r}_n \text{ on same cell} \end{cases} \tag{3.9}$$

$$\beta_n^{LCN} = J(\mathbf{r}_n). \tag{3.10}$$

$$V_n^{LCN} = V(\mathbf{r}_n). \tag{3.11}$$

It has been shown that the Nyström and moment methods are essentially equivalent by a linear transformation [29]. The equivalence of the well known Rao-Wilton-Glisson (RWG) functions to a low-order Nyström method is shown explicitly in [31]. A conversion for higher orders is shown in [12], where the Nyström DoF are cast onto the set of functions f_k used in Section 3.1 for the local corrections (or onto a weighted sum of these). A more general approach, however, is simply to evaluate the basis functions at the Nyström quadrature points. This is the approach used here, and it allows for more universal LCN-MoM conversion even when the MoM basis functions and the local correction testing functions are not the same.

The rationale for the conversion is illustrated by noting that each of the N_q Nyström unknowns β_n^{LCN} can be expressed in terms of the N_b MoM unknowns

β_n^{MoM} as

$$\beta_n^{LCN} = J(\mathbf{r}_n) \approx \sum_{i=1}^{N_b} \beta_i^{MoM} B_i(\mathbf{r}_n),\ n = 1, 2 \ldots N_q \tag{3.12}$$

that is,

$$\beta_n^{LCN} = J(\mathbf{r}_n) \approx [B_1(\mathbf{r}_n), B_2(\mathbf{r}_n), \ldots, B_{N_b}(\mathbf{r}_n)] \cdot \bar{\beta}^{MoM}, \tag{3.13}$$

and so the solution vectors $\bar{\beta}^{MoM}$ and $\bar{\beta}^{LCN}$ are related by

$$\bar{\beta}^{LCN} = \bar{J} \approx [\mathrm{C}^s]\, \bar{\beta}^{MoM} \tag{3.14}$$

where $\bar{\beta}^{LCN}$ and $\bar{\beta}^{MoM}$ indicate the vectors containing, respectively, the Nyström unknowns β_n^{LCN} and the moment-method unknowns β_n^{MoM}, and the source-side conversion matrix $[\mathrm{C}^s]$ is defined as

$$[\mathrm{C}^s] = \begin{bmatrix} B_1(\mathbf{r}_1) & B_2(\mathbf{r}_1) & \cdots & B_{N_b}(\mathbf{r}_1) \\ B_1(\mathbf{r}_2) & B_2(\mathbf{r}_2) & \cdots & B_{N_b}(\mathbf{r}_2) \\ \vdots & \vdots & \ddots & \vdots \\ B_1(\mathbf{r}_{N_q}) & B_2(\mathbf{r}_{N_q}) & \cdots & B_{N_b}(\mathbf{r}_{N_q}) \end{bmatrix}. \tag{3.15}$$

As pointed out in Section 3.4.1, continuity constraints can enable the moment method to discretize a problem to a given order with fewer unknowns than the Nyström method. As a result the $[\mathrm{C}^s]$ need not be square.

The matrix equation can now be written as

$$[Z^{LCN}]\, [\mathrm{C}^s]\, \bar{\beta}^{MoM} = \bar{V}^{LCN} \tag{3.16}$$

By multiplying $[Z^{LCN}] \cdot [\mathrm{C}^s]$, we get a system which we can solve for the MoM

DoF. If the Nyström solution vector is desired it can be recovered from $\bar{\beta}^{MoM}$ by multiplying by $[\mathrm{C}^s]$ as in (3.14).

A similar conversion can be applied to the field side of the equation, using a field-side conversion matrix $\left[\mathrm{C}^f\right]$ of the form

$$\left[\mathrm{C}^f\right] = \begin{bmatrix} \mathcal{J}_1\omega_1 T_1(\mathbf{r}_1) & \mathcal{J}_2\omega_2 T_1(\mathbf{r}_2) & \cdots & \mathcal{J}_{N_q}\omega_{N_q} T_1(\mathbf{r}_{N_q}) \\ \mathcal{J}_1\omega_1 T_2(\mathbf{r}_1) & \mathcal{J}_2\omega_2 T_2(\mathbf{r}_2) & \cdots & \mathcal{J}_{N_q}\omega_{N_q} T_{N_b}(\mathbf{r}_{N_q}) \\ \vdots & \vdots & \ddots & \vdots \\ \mathcal{J}_1\omega_1 T_{N_b}(\mathbf{r}_1) & \mathcal{J}_2\omega_2 T_{N_b}(\mathbf{r}_2) & \cdots & \mathcal{J}_{N_q}\omega_{N_q} T_{N_b}(\mathbf{r}_{N_q}) \end{bmatrix} \tag{3.17}$$

where the functions T_n are the MoM test functions, and $\mathcal{J}_i$ and ω_i are the Jacobian and quadrature weight, respectively, at each quadrature point $\mathbf{r}_i$. Multiplying $\bar{V}^{LCN}$ on the left by $\left[\mathrm{C}^f\right]$ gives the forcing vector $\bar{V}^{MoM}$ for the moment method, whose entries are defined by

$$V_n^{MoM} = \int_\Omega T_n(\mathbf{r}) V(\mathbf{r}) d\Omega. \tag{3.18}$$

Thus multiplying both sides of (3.16) on the left by $\left[\mathrm{C}^f\right]$ gives

$$\left[\mathrm{C}^f\right] \left[Z^{LCN}\right] \left[\mathrm{C}^s\right] \bar{\beta}^{MoM} = \left[\mathrm{C}^f\right] \bar{V}^{LCN} = \bar{V}^{MoM}, \tag{3.19}$$

that is, $\left[\mathrm{C}^f\right] \left[Z^{LCN}\right] \left[\mathrm{C}^s\right]$ is the completely converted moment-method matrix for the problem, using test functions T_n and basis functions B_n.

For the hexahedral basis functions discussed here, the MoM basis order should in general be one less in each coordinate direction than the corresponding number of points in the Nyström test grid. That is, if the Nyström matrix for a given cell uses a $n_i \times n_j \times n_k$ quadrature rule, where n_ℓ is the number of distinct abscissae on the u^ℓ axis, the MoM basis functions used for conversion should be polynomial complete to order $p_\ell = n_\ell - 1$ in u^ℓ. If the basis functions are of higher order, the

conversion matrix will be rank deficient, resulting in an underdetermined system matrix if $[Z^{LCN}]$ is square. On the other hand, using basis functions of a lower order than $n_\ell - 1$ in u^ℓ gives an overdetermined system if the original Nyström matrix is square. As above, an analogous field-side conversion can be applied to give a square matrix once again, but the reduced set of basis functions, spanning a space of dimension less than $n_i \times n_j \times n_k$ on each cell, will not in general be able to represent the unknowns with the same accuracy as the basis functions complete to order $n_\ell - 1$ in u^ℓ.

It is sometimes convenient (cf. [28]) to use degrees of freedom defined as

$$\beta_n^{LCN} = J(\mathbf{r}_n)\mathcal{J}(\mathbf{r}_n). \tag{3.20}$$

Moreover, scaling each row of $[Z^{LCN}]$ and each corresponding entry of the right-hand side $\bar{V}^{LCN}$ by the quadrature weight ω_m at the field point $\mathbf{r}_m$ makes the far interactions in the matrix symmetric, as pointed out in [13]. This allows the system matrix elements in (3.9) for $\mathbf{r}_m$ and $\mathbf{r}_n$ on different cells to be written as

$$[Z^{LCN}]_{mn} = [Z^{LCN}]_{nm} = \omega_m \omega_n K(\mathbf{r}_m, \mathbf{r}_n), \tag{3.21}$$

and elements in the field-side conversion matrix $\left[\mathrm{C}^f\right]$ in (3.17) as

$$\left[\mathrm{C}^f\right]_{mn} = \mathcal{J}(\mathbf{r}_n) T_m(\mathbf{r}_n). \tag{3.22}$$

In a problem where a vector quantity $\mathbf{J}$ related to the forcing function $\mathbf{V}(\mathbf{r})$ by

$$\mathbf{V}(\mathbf{r}) = \mathcal{L}\mathbf{J}(\mathbf{r}) \tag{3.23}$$

then the unknown is represented at a point $\mathbf{r}_n$ using a set of vectors such as the unitary vectors $\mathbf{a}_\ell$ discussed above. When the DoF are scaled as in (3.20), the unknown $\beta_{n,\ell}^{LCN}$ is then defined by

$$\beta_{n,\ell}^{LCN} = \left(\mathbf{J}(\mathbf{r}_n) \cdot \mathbf{a}^\ell(\mathbf{r}_n)\right) \mathcal{J}(\mathbf{r}_n) \tag{3.24}$$

where $\mathbf{a}^\ell$ signifies the reciprocal vectors defined in [63] which have the property

$$\mathbf{a}_m \cdot \mathbf{a}^n = \delta_{mn}.$$

Test vectors $\mathbf{t}$ are applied to both sides of (3.23)

$$\mathbf{t}(\mathbf{r}) \cdot \mathbf{V}(\mathbf{r}) = \mathbf{t}(\mathbf{r}) \cdot \mathcal{L}\mathbf{J}(\mathbf{r}). \tag{3.25}$$

Further details on the discretization of vector quantities can be found in [12].

Note that in this chapter the Nyström and converted Nyström discretizations use a mixed-order representation for vector quantities. This approach has been found to give better accuracy than a polynomial-complete representation [64, 70]. A polynomial-complete representation is used for the scalar unknowns ρ.

In order to convert from a Nyström matrix to a Galerkin-tested MoM matrix, it is necessary that the test vectors $\mathbf{t}$ be the unitary vectors used in the MoM bases, rather than the reciprocal vectors typically used for Nyström testing. Moreover, while a mixed-order test grid is often used in a Nyström discretization, moment methods usually use a polynomial-complete testing scheme. In numerical tests described below it is found that converting from the Nyström to the moment-method discretization gives good results, but note that because a mixed-order testing scheme is used here the converted matrix will differ somewhat from the typical MoM matrix for the same problem.

3.3 Advantages of Nyström-Moment Method Conversion

The method presented here may be viewed as a more efficient method of calculating a moment method system matrix than direct computation of the integrals. Consider two cell domains Ω_m and Ω_n. Suppose that the moment method interaction $Z^{MoM}_{q_m,q_n}$ between basis function B_{q_n} on Ω_n and test function T_{q_m} on cell Ω_m is calculated numerically with an N_q-point quadrature rule, as

$$Z^{MoM}_{q_m,q_n} = \int_{\Omega_m} T_{q_m}(\mathbf{r}) \int_{\Omega_n} B_{q_n}(\mathbf{r}')K(\mathbf{r},\mathbf{r}')d\Omega' d\Omega \tag{3.26}$$

$$\approx \sum_{i_m=1}^{N_q} T_{q_m}(\mathbf{r}_{i_m})\mathcal{J}(\mathbf{r}_{i_m})\omega_{i_m} \sum_{i_n=1}^{N_q} B_{q_n}(\mathbf{r}_{i_n})K(\mathbf{r}_{i_m},\mathbf{r}_{i_n})\mathcal{J}(\mathbf{r}_{i_n})\omega_{i_n}. \tag{3.27}$$

With N_T test functions on Ω_m and N_B basis functions on Ω_n, assuming the same quadrature rule is used for each pair of functions B_{q_n} and T_{q_m}, this implies that the quantity $K(\mathbf{r}_{i_m},\mathbf{r}_{i_n})\mathcal{J}(\mathbf{r}_{i_n})$ for each point pair $(\mathbf{r}_{i_m},\mathbf{r}_{i_n})$ is computed $N_T \times N_B$ times. Moreover, the quantity $T_{q_m}(\mathbf{r}_{i_m})$ is computed N_B times for each Ω_n, and $B_{q_n}(\mathbf{r}_{i_n})$ computed N_T times for each Ω_m. Of course, efficient programming can eliminate certain redundant computations, but it is worth noting that when the MoM matrix is derived from a Nyström matrix as illustrated above, each of these quantities need only be computed once.

The utility of the Nyström-MoM conversion is also apparent in an experimental context. As will be seen below, selective conversion of Nyström system matrix blocks to MoM blocks can be easily carried out to determine the effect of using one method or the other on computing relations between different sources and fields. For example, in a problem with unknowns $\begin{bmatrix}\bar{\alpha}\\ \bar{\beta}\end{bmatrix}$ and forcing vector $\begin{bmatrix}\bar{V}_1\\ \bar{V}_2\end{bmatrix}$, related

by

$$\begin{bmatrix} [Z_{1,\alpha}^{LCN}] & [Z_{1,\beta}^{LCN}] \\ [Z_{2,\alpha}^{LCN}] & [Z_{2,\beta}^{LCN}] \end{bmatrix} \begin{bmatrix} \bar{\alpha}^{LCN} \\ \bar{\beta}^{LCN} \end{bmatrix} = \begin{bmatrix} \bar{V}_1^{LCN} \\ \bar{V}_2^{LCN} \end{bmatrix} \tag{3.28}$$

one can specifically convert blocks in the system matrix associated with $\bar{\alpha}$:

$$\begin{bmatrix} [Z_{1,\alpha}^{LCN}] & [Z_{1,\beta}^{LCN}] \\ [Z_{2,\alpha}^{LCN}] & [Z_{2,\beta}^{LCN}] \end{bmatrix} \begin{bmatrix} [C_\alpha^s] & [0] \\ [0] & [I] \end{bmatrix} \begin{bmatrix} \bar{\alpha}^{MoM} \\ \bar{\beta}^{LCN} \end{bmatrix} = \begin{bmatrix} \bar{V}_1^{LCN} \\ \bar{V}_2^{LCN} \end{bmatrix} \tag{3.29}$$

where $[0]$ signifies an appropriately sized matrix of zeros, and $[I]$ is an identity matrix. The field-side conversion for the $\bar{V}_1$ block can also be applied:

$$\begin{aligned} \begin{bmatrix} [C_1^f] & [0] \\ [0] & [I] \end{bmatrix} \begin{bmatrix} [Z_{1,\alpha}^{LCN}] & [Z_{1,\beta}^{LCN}] \\ [Z_{2,\alpha}^{LCN}] & [Z_{2,\beta}^{LCN}] \end{bmatrix} \begin{bmatrix} [C_\alpha^s] & [0] \\ [0] & [I] \end{bmatrix} \begin{bmatrix} \bar{\alpha}^{MoM} \\ \bar{\beta}^{LCN} \end{bmatrix} \\ = \begin{bmatrix} [C_1^f] & [0] \\ [0] & [I] \end{bmatrix} \begin{bmatrix} \bar{V}_1^{LCN} \\ \bar{V}_2^{LCN} \end{bmatrix} \end{aligned} \tag{3.30}$$

or

$$\begin{bmatrix} [Z_{1,\alpha}^{CMoM}] & [C_1^f][Z_{1,\beta}^{LCN}] \\ [Z_{2,\alpha}^{LCN}][C_\alpha^s] & [Z_{2,\beta}^{LCN}] \end{bmatrix} \begin{bmatrix} \bar{\alpha}^{MoM} \\ \bar{\beta}^{LCN} \end{bmatrix} = \begin{bmatrix} \bar{V}_1^{MoM} \\ \bar{V}_2^{LCN} \end{bmatrix} \tag{3.31}$$

where $[Z_{1,\alpha}^{CMoM}]$ is the converted-to-moment-method block $[C_1^f][Z_{1,\alpha}^{CMoM}][C_\alpha^s]$. The ability to convert blocks selectively can be advantageous when, for example, the unknown associated with $\bar{\alpha}$ can be represented by fewer DoF in a moment-method discretization, as in certain numerical tests described below. This enables one to experiment with different discretizations of the various interactions in a complicated problem, toggling different blocks to moment-method blocks as needed and comparing the conditioning or other properties of the resulting system matrices. In the eddy current problems such as those discussed below, for instance, blocks associated with the electric current $\mathbf{J}$ and magnetization $\mathbf{M}$ or, more often, only those

associated with $\mathbf{J}$, can be specifically converted to a moment-method discretization. The remaining unknowns, particularly those associated with charge density, are generally left as Nyström DoF, though their number may be reduced owing to the normal continuity of the moment-method basis functions representing $\mathbf{J}$.

3.4 Numerical Test Results

In this section are described the integral equations used for solving quasi-magnetostatic problems with eddy currents in magnetic-conducting material, as well as numerical results obtained using LCN and converted LCN-MoM discretizations.

3.4.1 Solution of Quasi-Magnetostatic Problems

Volume integral equation (VIE) modeling of magnetostatic problems is discussed in [26], and modeling of quasi-magnetostatic problems with eddy currents is discussed in [27]. Another formulation is developed from this in order to obtained a well-conditioned system in [28], where the problem is described by the following equations:

$$\begin{aligned}\mathbf{H}_s(\mathbf{r}) =& \chi_m^{-1}(\mathbf{r})\mathbf{M}(\mathbf{r}) - \iiint_V \boldsymbol{\nabla}\boldsymbol{\nabla}\cdot\left[G(\mathbf{r},\mathbf{r}')\mathbf{M}(\mathbf{r}')\right] dV' \\ & - \iiint_V \boldsymbol{\nabla} G(\mathbf{r},\mathbf{r}') \times \mathbf{J}(\mathbf{r}') dV',\end{aligned} \tag{3.32}$$

$$\begin{aligned}\mathbf{A}_s(\mathbf{r}) =& \frac{-\mathbf{J}(\mathbf{r})}{j\omega\sigma(\mathbf{r})} - \mu_0 \iiint_V G(\mathbf{r},\mathbf{r}')\mathbf{J}(\mathbf{r}')dV' - \mu_0 \iiint_V \boldsymbol{\nabla} G(\mathbf{r},\mathbf{r}') \times \mathbf{M}(\mathbf{r}')dV' \\ & - \frac{1}{j\omega\epsilon_0} \iiint_V \boldsymbol{\nabla} G(\mathbf{r},\mathbf{r}')\rho(\mathbf{r}')dV',\end{aligned} \tag{3.33}$$

$$0 = \boldsymbol{\nabla}\cdot\mathbf{J}(\mathbf{r}) + j\omega\rho(\mathbf{r}), \tag{3.34}$$

and

$$0 = \iiint_V \rho(\mathbf{r}) dv' \tag{3.35}$$

where

$$G(\mathbf{r}, \mathbf{r}') = \frac{1}{4\pi|\mathbf{r} - \mathbf{r}'|}. \tag{3.36}$$

In these equations, χ_m represents the magnetic susceptibility, equal to $\mu_r - 1$ where μ_r is the relative permeability. σ is the conductivity, and ϵ_0 and μ_0 signify, respectively, the permittivity and permeability of free space. The time-harmonic electric field intensity $\mathbf{E}$, magnetic field intensity $\mathbf{H}$, electric current density $\mathbf{J}$, magnetization $\mathbf{M}$, magnetic vector potential $\mathbf{A}$, and electric volume charge density ρ, use an $e^{+j\omega t}$ convention.

As in [28], the unknowns are scaled by the Jacobian. Let $\mathbf{r}_{n\ell q}$ be the qth quadrature point on the grid for the u^ℓ direction on the nth cell. The vector quantity $\mathbf{F}_\ell$, that is, the component of $\mathbf{F}$ in the u^ℓ direction, is related to the scalar unknown $f_{n\ell q}$ by

$$\mathbf{F}_\ell(\mathbf{r}_{n\ell q}) = f_{n\ell q} \frac{\mathbf{a}_\ell(\mathbf{r}_{n\ell q})}{\mathcal{J}_{n\ell q}} \tag{3.37}$$

where $\mathcal{J}_{n\ell q}$ is the Jacobian at $\mathbf{r}_{n\ell q}$. Scalar quantities ρ are related to the corresponding unknowns γ by

$$\rho(\mathbf{r}_{nq}) = \frac{\gamma_{nq}}{\mathcal{J}_{nq}}. \tag{3.38}$$

From (3.34) it follows that on some interface S between adjoining cells V_m and V_n in V

$$j\omega\rho^s(\mathbf{r}) = \hat{\mathbf{n}}_m \cdot \mathbf{J}_m(\mathbf{r}) + \hat{\mathbf{n}}_n \cdot \mathbf{J}_n(\mathbf{r}),\ \mathbf{r} \in S \tag{3.39}$$

where ρ^s is the electric surface charge density on S, $\mathbf{J}_\ell$ is the current density in cell V_ℓ, and $\hat{\mathbf{n}}_\ell$ is the outward normal to S from cell ℓ. Such charges accumulate

at interfaces of discontinuity in conductivity or permittivity. When using the Nyström method, however, non-physical boundary charges between cells in a homogeneous region can also appear. This is because the Nyström method, unlike the moment method, does not make use of basis functions that explicitly enforce the normal continuity of **J** at mesh element boundaries. In the augmented formulation used here, this means that enforcing (3.35) requires that fictitious boundary charges be modeled as separate degrees of freedom. Conversion of the LCN matrix blocks associated with **J** to moment-method matrix blocks using divergence-conforming basis functions eliminates these degrees of freedom.

A further reduction in the number of unknowns through the Nyström-MoM conversion is made possible by the interdependence of face bases defined on opposite sides of a shared face. In the mixed-order scheme described in Chapter 2, it was found that each volume element had $3 \cdot p(p+1)^2$ volume bases associated with it, and that each face had $(p+1)^2$ bases. For a mesh with N_V volumes and N_F faces, the moment method with divergence-conforming bases therefore gives us $(3 \cdot p \cdot N_V + N_F)(p+1)^2$ degrees of freedom. A Nyström method employing a mixed-order testing grid would have $3 \cdot N_V \cdot (p+2)(p+1)^2$ degrees of freedom for the same mesh. This implies that as long as $N_F < 6N_V$, i.e. if at least two of the cells share a face, the moment method will yield a system with fewer degrees of freedom.

3.4.2 Conducting Sphere

The availability of an analytic solution to the system in (3.32)-(3.36) for a magnetic conducting sphere makes it a good candidate for testing the proposed method (cf. [71]). Here a $1\,\mathrm{m}$ radius sphere of conductivity $10^5\,\mathrm{S\,m^{-1}}$ and relative permeability μ_r, excited by a uniform time-harmonic z-directed magnetic field of amplitude $1\,\mathrm{A\,m^{-1}}$, is simulated using a Nyström code with and without a Nyström-MoM

conversion. Tests are run for a sphere that is conducting only ($\mu_r = 1$) and for a sphere that is both magnetic and conducting ($\mu_r = 10$). The sphere is meshed with 32 and 256 hexahedral elements of 10th order.

3.4.2.1 Accuracy

Figure 3.1 shows the relative RMS error in the resulting **H** computed at a set of 102 points evenly spaced in θ and φ at $1.5\,\mathrm{m}$ from the center of the sphere. The problem frequency is $4\,\mathrm{Hz}$. The results demonstrate the greater accuracy that can be gained with a smaller number of unknowns by using a higher-order discretization and illustrate the ability of the Nyström-MoM conversion to decrease the number of degrees of freedom without sacrificing accuracy. When the simulation is run at basis order $p = 3$ using a 32-hex mesh, with the matrix block associated with **J**-**A** interactions converted to a moment-method discretization (as in (3.30), with $\bar{\alpha}$ containing **J** DoF and $\bar{V}_1$ containing the **A** DoF), the solution error is about two orders of magnitude lower than the error in a $p = 1$ Nyström solution for a 256-hex mesh, while requiring just under $70\,\%$ the number of unknowns.

3.4.2.2 Conditioning

The condition number for the sphere problem system matrix is plotted for the first few basis orders at $50\,\mathrm{Hz}$ in Figs. 3.2 and 3.3 and at $200\,\mathrm{Hz}$ in Figs. 3.4 and 3.5. In Figs. 3.3 and 3.5 a preconditioner based on matrix binormalization [28] is used to reduce the condition number. While the conditioning is significantly improved by the conversion before application of the preconditioner, the improvement is much less drastic after preconditioning.

3.4.3 Magnetic Conducting Torus

A torus with major radius $2\,\mathrm{m}$ and minor radius $1\,\mathrm{m}$ is used to assess the performance of the proposed method for a volume bounded by a multiply-connected surface. The torus is meshed with 6th-order hexahedral elements and the condition number computed both with and without matrix preconditioning for an eddy current frequency of $50\,\mathrm{Hz}$. Figure 3.6 indicates a significant improvement effected by the conversion using the numerically constrained bases. Figure 3.7, however, shows that this improvement is largely lost when a preconditioner is applied.

3.4.4 TEAM7 Problem

The Testing Electromagnetic Analysis Methods problem 7 (TEAM7) published by the International Compumag Society allows us to compare simulated field and current values for an asymmetric nonmagnetic conductor to measured results. The test case consists of a rectangular aluminum plate with an offset rectangular hole, excited by nearby coils at $50\,\mathrm{Hz}$. Details about the problem are discussed in [72]. In this paper the conducting plate is meshed with a single layer of 180 right hexahedra.

3.4.4.1 Accuracy

Figure 3.8 compares the simulated z-directed magnetic flux density to the result of physical measurement, showing close agreement especially at basis order 2. Likewise, the y-directed current density shown in Fig. 3.9 quickly approaches the measured solution as the basis order is increased.

3.4.4.2 Conditioning

The reduction in number of unknowns for the different basis orders is shown in Table 3.1. Figure 3.10 compares the condition number of the system matrix, with and without preconditioning, for the pure Nyström method and for the Nyström matrix with a converted **J**-**A** interaction block (again, as in (3.30), with $\bar{\alpha}$ containing **J** DoF and $\bar{V}_1$ containing the **A** DoF). Conversions are made using the bases discussed in Chapter 2. Once again, while the condition number is substantially reduced by the conversion, the reduction is not maintained after preconditioning.

3.5 Summary

In this chapter a simple and general conversion of matrix blocks in a locally corrected Nyström integral equation discretization to a moment method discretization is described. Application to quasi-magnetostatic problems yields accurate results for a variety of geometries and materials and lowers the number of unknowns required for simulation.

Two different basis function sets are used for the moment-method conversion, and the highly orthogonal functions presented in Chapter 2 are found to give an immediate improvement in the matrix conditioning. While the conditioning improvement over the pure Nyström discretization is significantly diminished by the use of a preconditioner, the solutions thus obtained show similar accuracy and require a smaller number of unknowns. Moreover, the general conversion shown above from the LCN method to the method of moments allows for quick and simple computation of moment method systems from an existing LCN matrix, making experimentation with different basis functions straightforward and fast.

TABLE 3.1: Number of Unknowns for Different Basis Orders and Solution Formulations for TEAM7 Problem

Basis Order p	Nyström		Constrained **J**	
	Source Unknowns	Field Unknowns	Source Unknowns	Field Unknowns
0	2,020	2,021	1,380	1,381
1	10,960	10,961	8,400	8,401
2	31,140	31,141	25,380	25,381
3	66,880	66,881	56,640	56,641

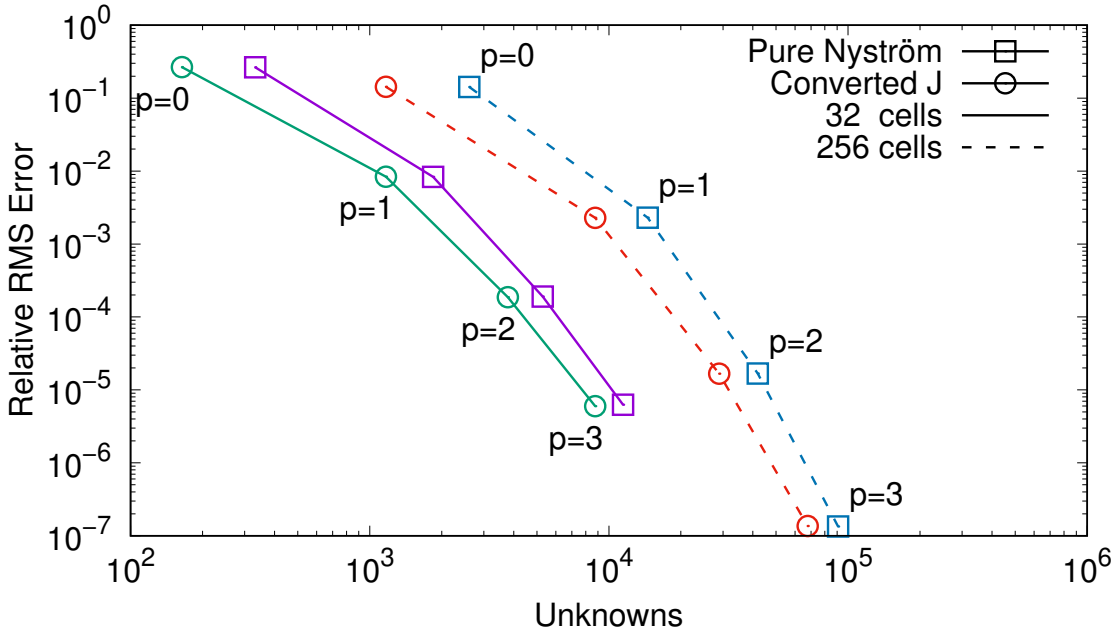

(a) $\mu_r = 1$

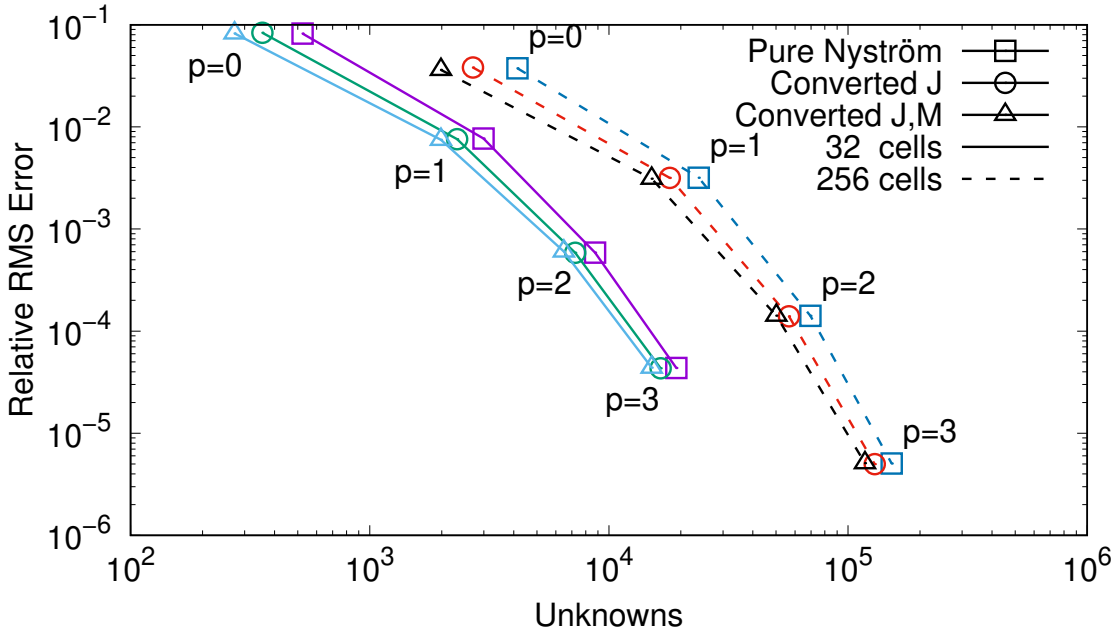

(b) $\mu_r = 10$

FIGURE 3.1: Relative RMS error in near-field $\mathbf{H}$ for $1\,\mathrm{m}$ radius sphere with $10^5\,\mathrm{S\,m^{-1}}$ conductivity at $4\,\mathrm{Hz}$. Integration tolerance is 10^{-12}.

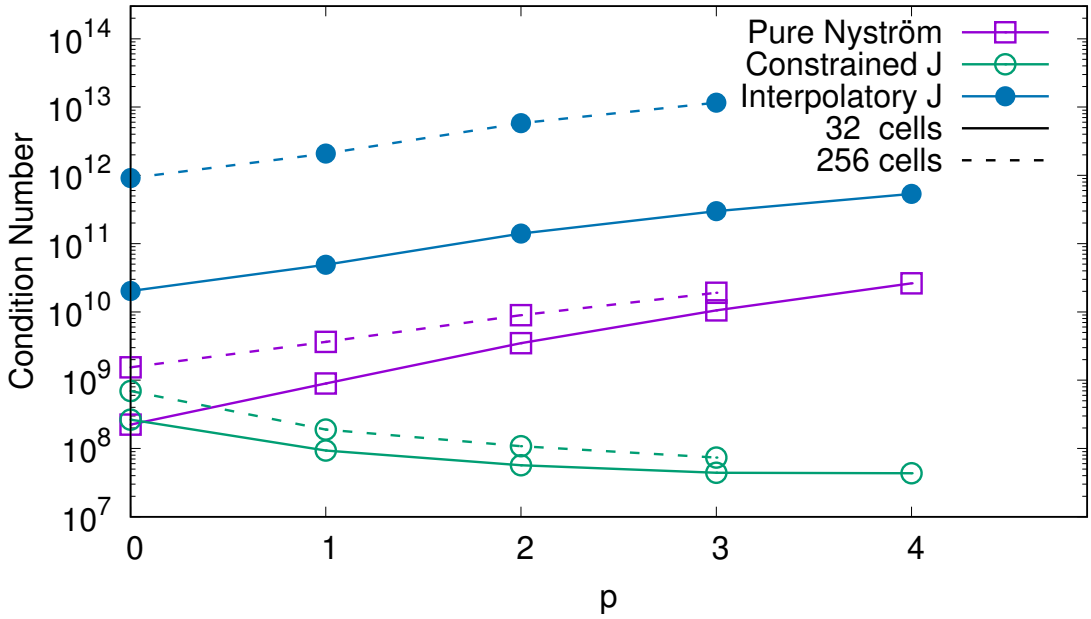

(a) $\mu_r = 1$

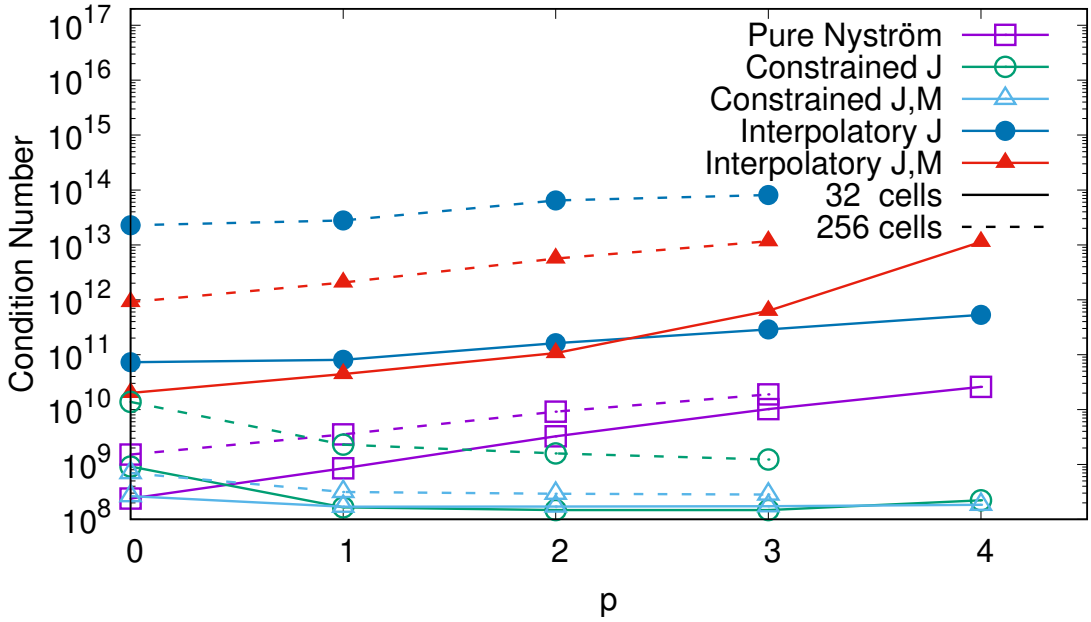

(b) $\mu_r = 10$

FIGURE 3.2: System matrix condition number versus basis order p for $1\,\mathrm{m}$ radius sphere with $10^5\,\mathrm{S\,m^{-1}}$ conductivity at $50\,\mathrm{Hz}$. Integration tolerance is 10^{-6}.

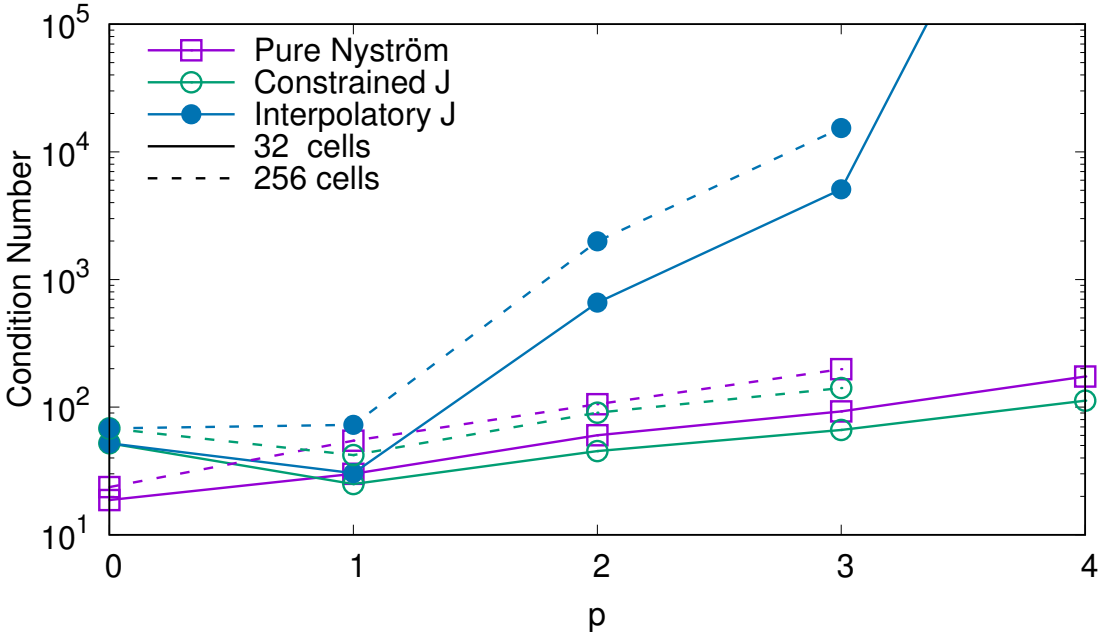

(a) $\mu_r = 1$

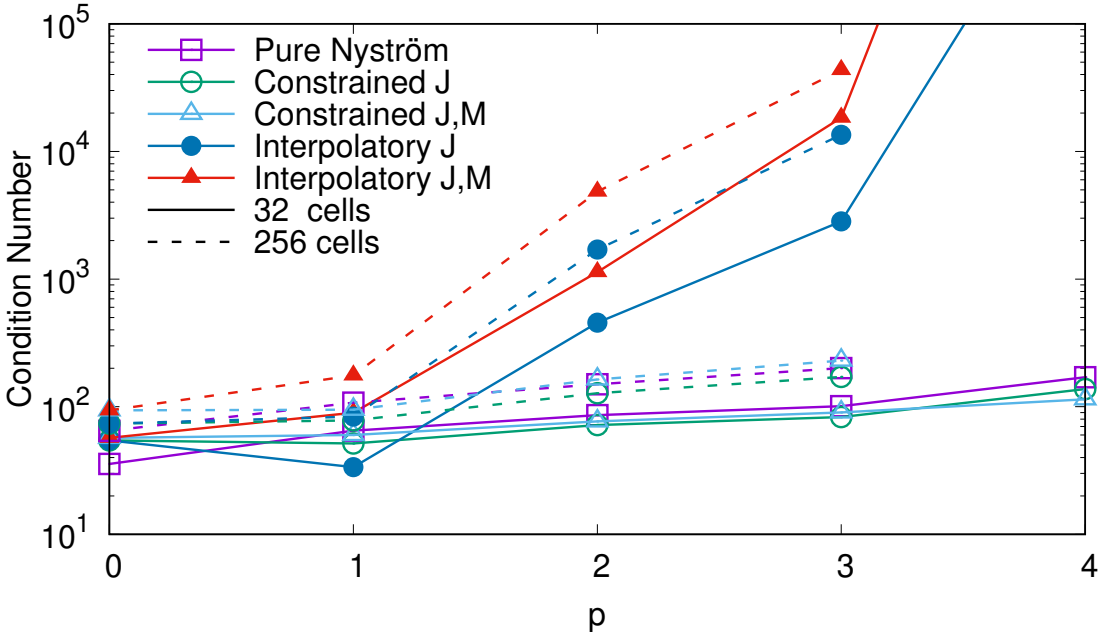

(b) $\mu_r = 10$

FIGURE 3.3: Preconditioned system matrix condition number versus basis order p for $1\,\mathrm{m}$ radius sphere with $10^5\,\mathrm{S\,m^{-1}}$ conductivity at $50\,\mathrm{Hz}$. Integration tolerance is 10^{-6}.

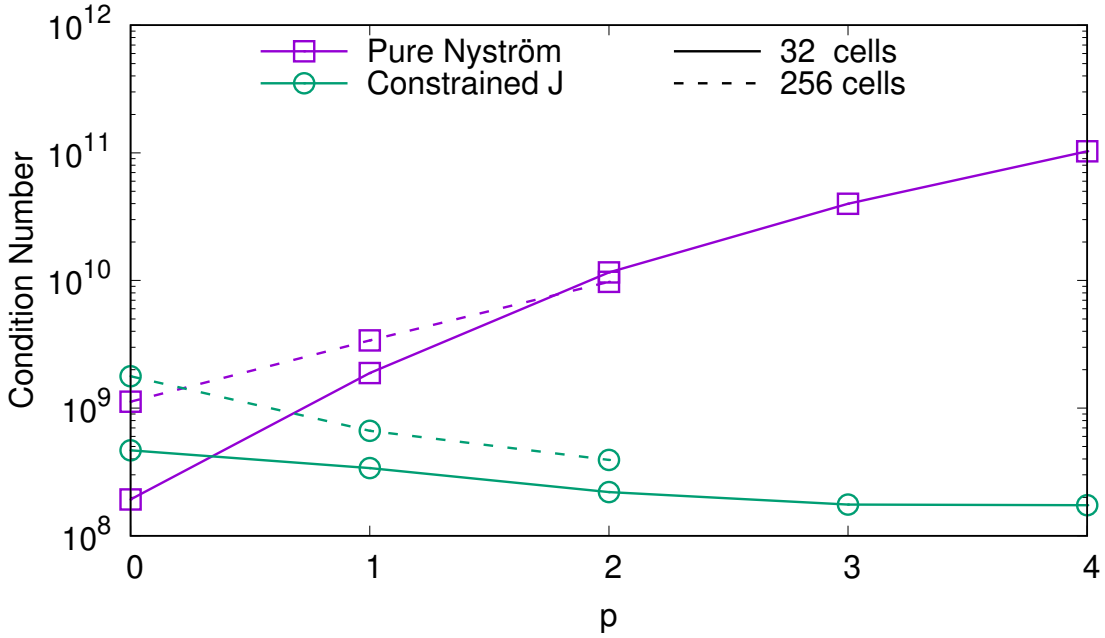

(a) $\mu_r = 1$

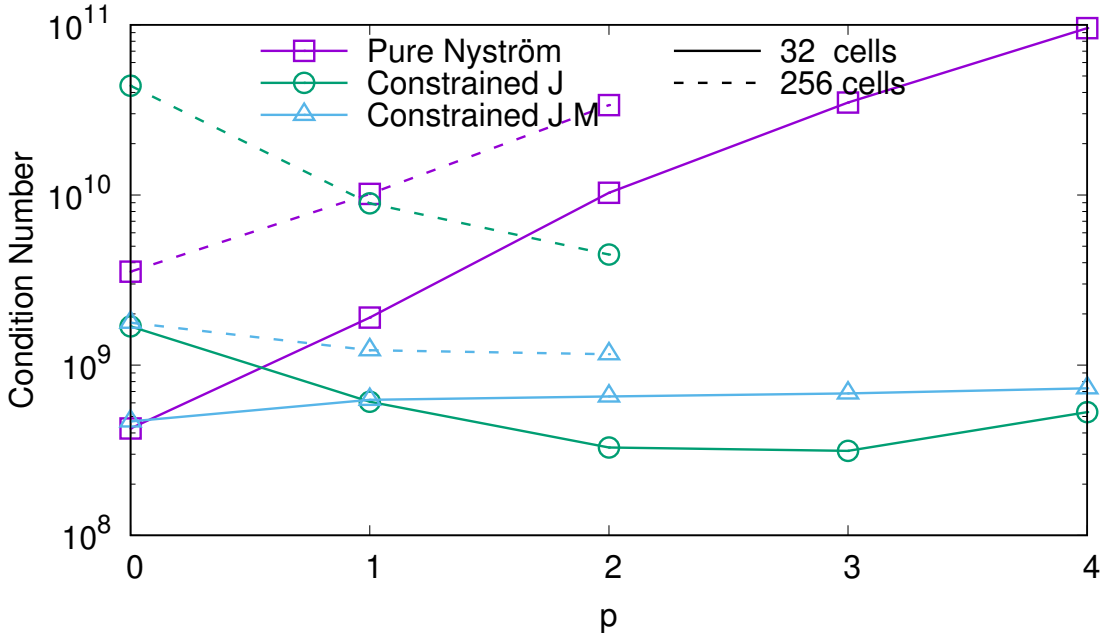

(b) $\mu_r = 10$

FIGURE 3.4: System matrix condition number versus basis order p for $1\,\mathrm{m}$ radius sphere with $10^5\,\mathrm{S\,m^{-1}}$ conductivity at $200\,\mathrm{Hz}$. Integration tolerance is 10^{-6}.

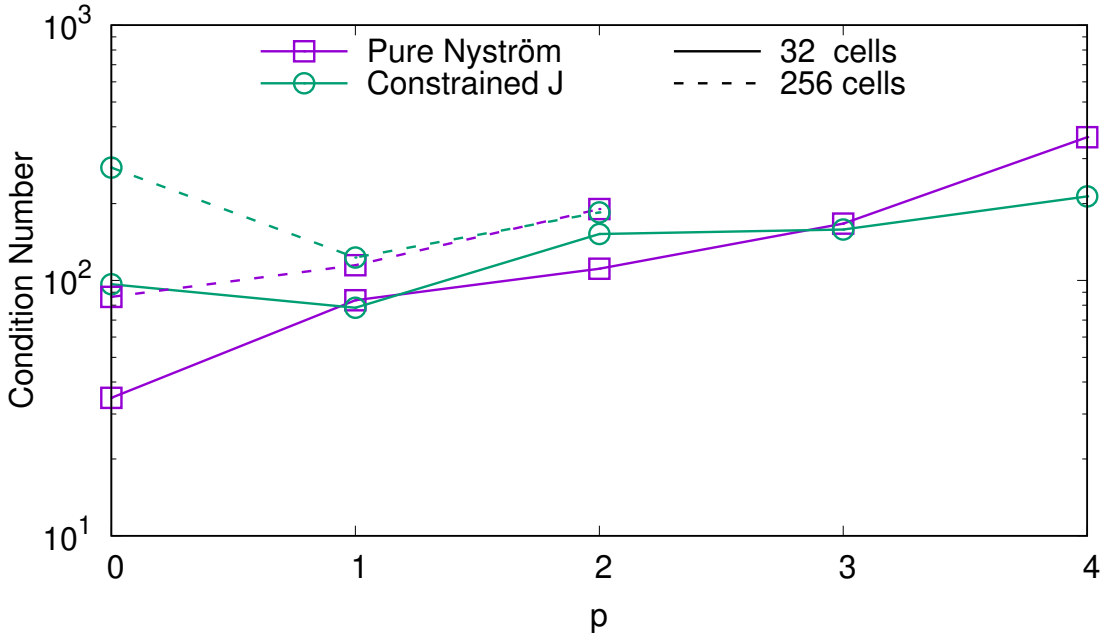

(a) $\mu_r = 1$

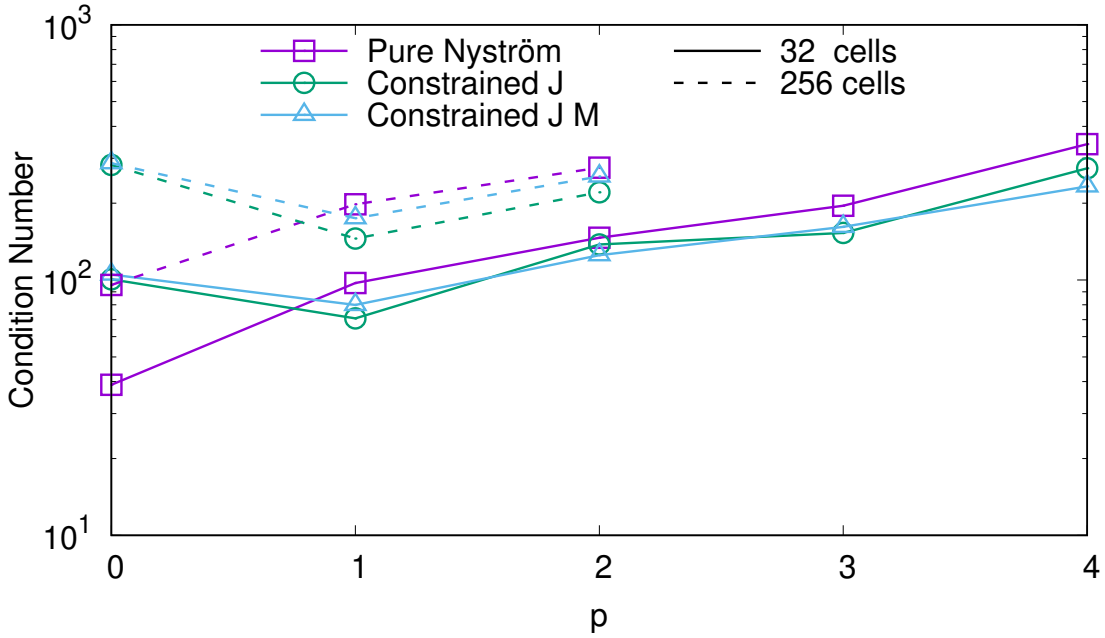

(b) $\mu_r = 10$

FIGURE 3.5: Preconditioned system matrix condition number versus basis order p for $1\,\mathrm{m}$ radius sphere with $10^5\,\mathrm{S\,m^{-1}}$ conductivity at $200\,\mathrm{Hz}$. Integration tolerance is 10^{-6}.

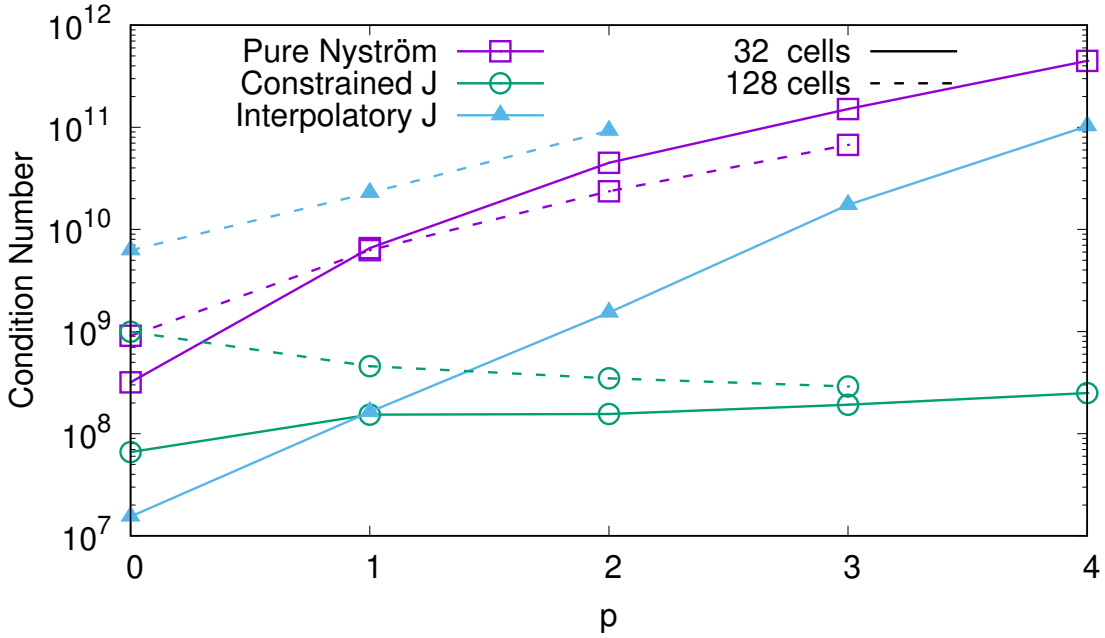

(a) $\mu_r = 1$

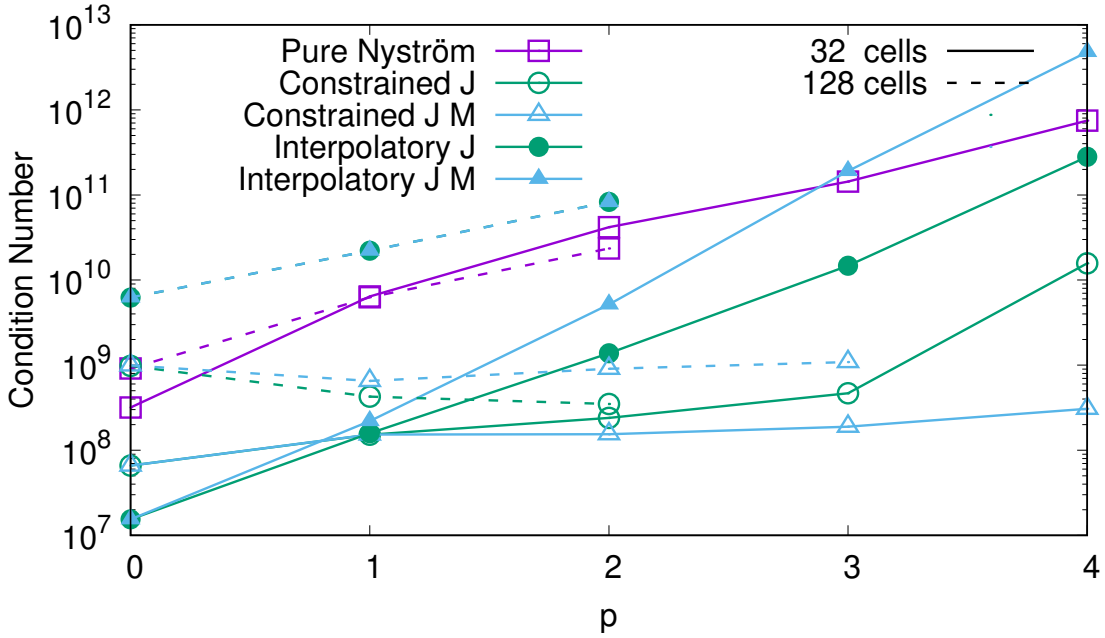

(b) $\mu_r = 10$

FIGURE 3.6: System matrix condition number versus basis order p for $2.0\,\mathrm{m}$ major radius, $1.0\,\mathrm{m}$ minor radius torus with $10^5\,\mathrm{S\,m^{-1}}$ conductivity at $50\,\mathrm{Hz}$. Integration tolerance is 10^{-6}.

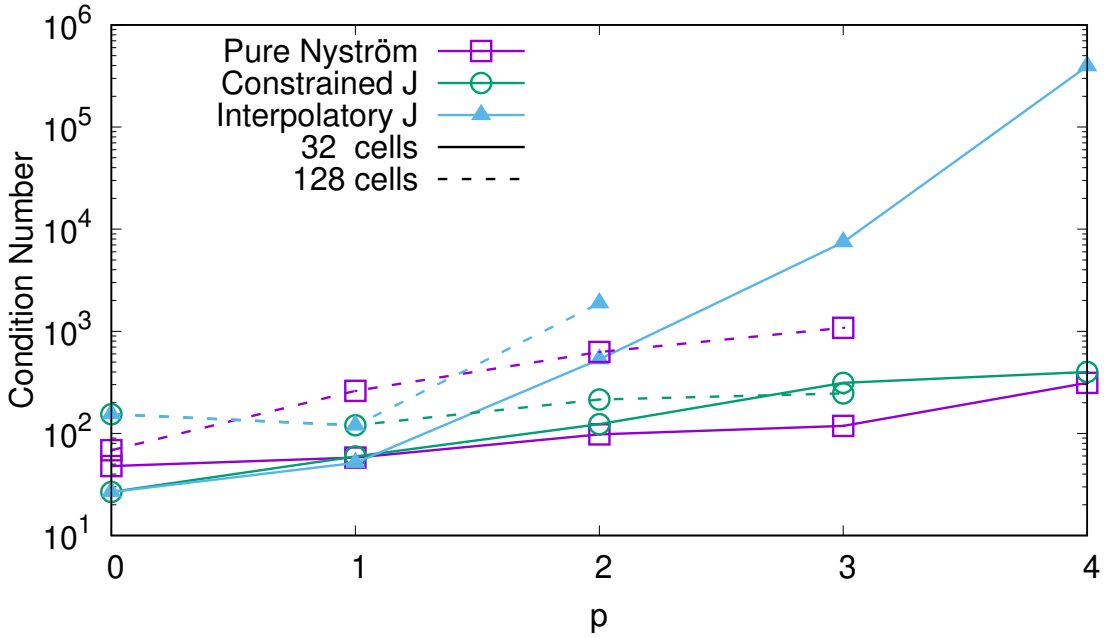

(a) $\mu_r = 1$

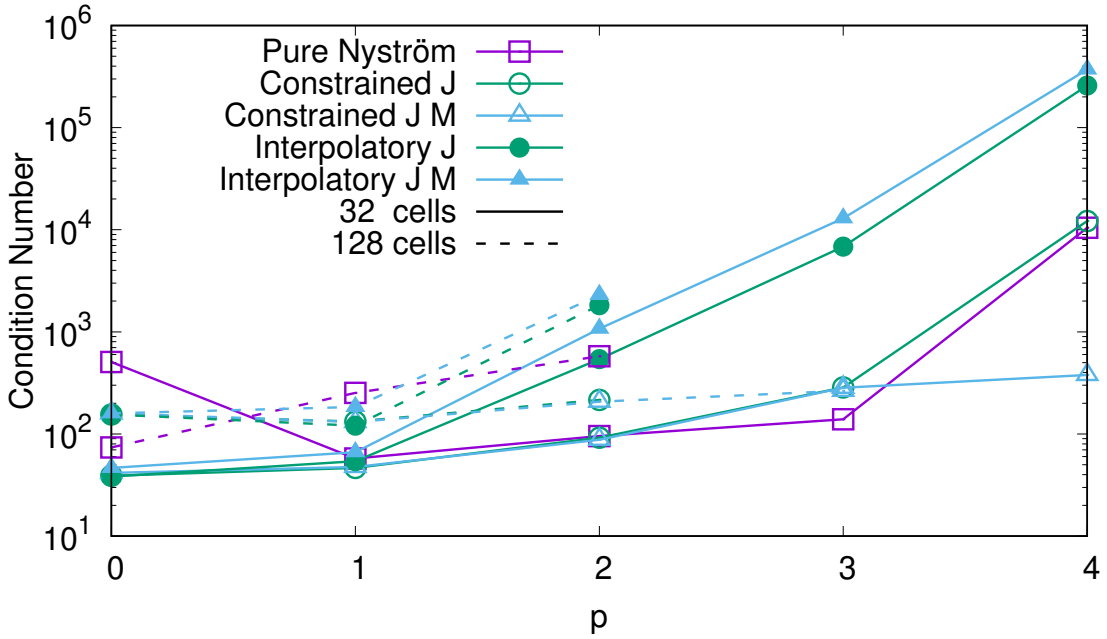

(b) $\mu_r = 10$

FIGURE 3.7: Preconditioned system matrix condition number versus basis order p for $2.0\,\mathrm{m}$ major radius, $1.0\,\mathrm{m}$ minor radius torus with $10^5\,\mathrm{S\,m^{-1}}$ conductivity at $50\,\mathrm{Hz}$. Integration tolerance is 10^{-6}.

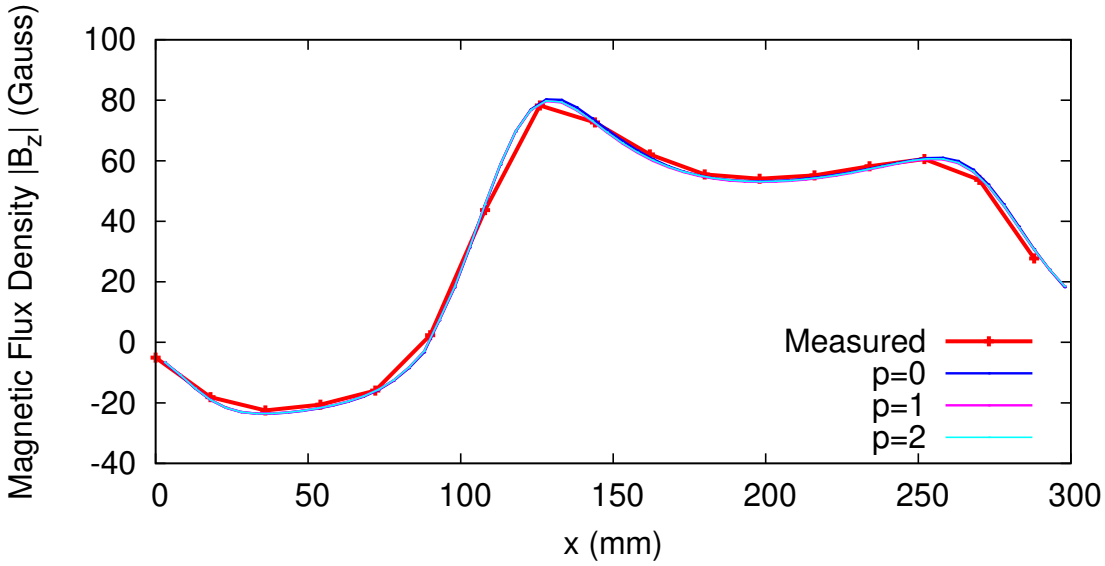

FIGURE 3.8: Z-directed magnetic flux density on line A1-B1 for TEAM7 test case at $50\,\mathrm{Hz}$ [72]. Integration tolerance is 10^{-3}.

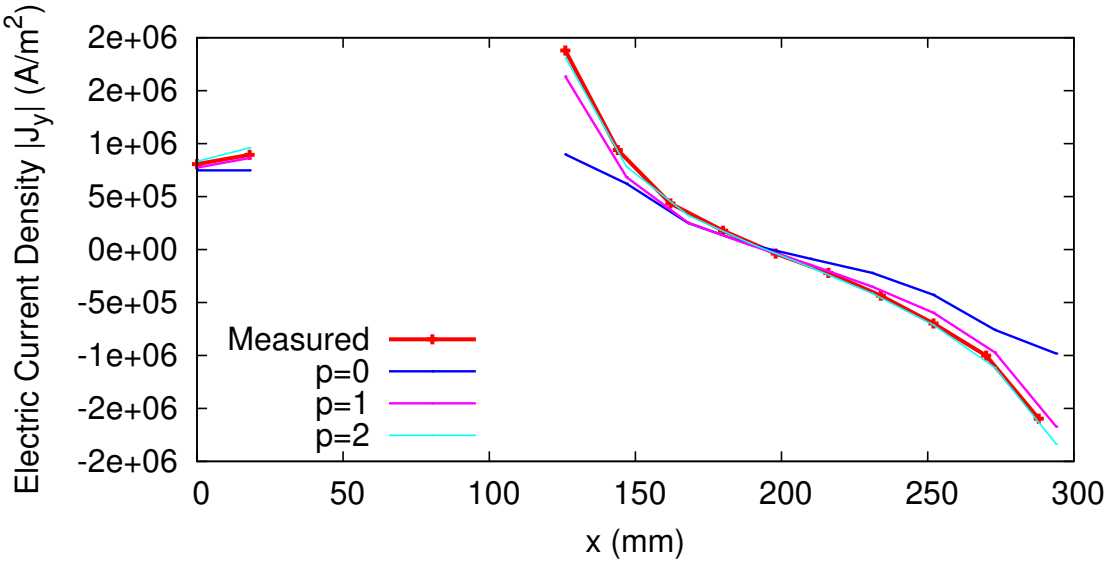

FIGURE 3.9: Y-directed electric current density on line A3-B3 for TEAM7 test case at $50\,\mathrm{Hz}$ [72]. Integration tolerance is 10^{-3}.

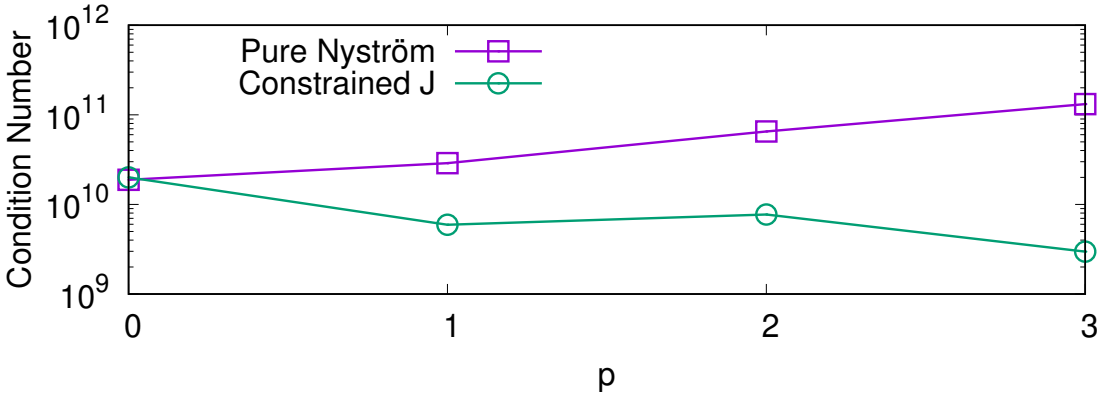

(a) Without Preconditioning

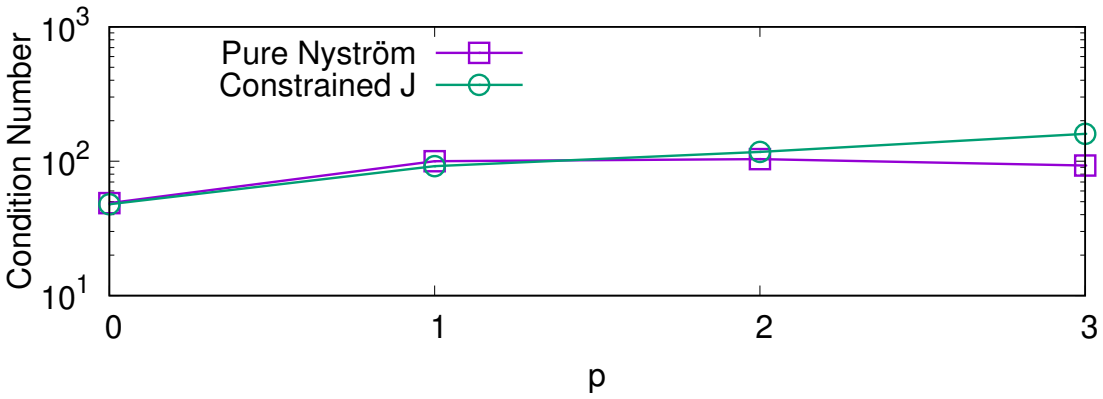

(b) With Preconditioning

FIGURE 3.10: System matrix condition number for TEAM7 problem. Integration tolerance is 10^{-3} to 10^{-5}.

CHAPTER 4. Impressed Current Corrosion Protection Simulation

In this chapter we look at the computational solution of Laplace's equation with a view to modeling the impressed-current corrosion protection (ICCP) systems used on nautical structures. Iterative approaches for solving problems with nonlinear boundary conditions are described and compared. Numerical tests show the accuracy attainable using a high-order locally corrected Nyström discretization, and iterative solver results are illustrated for different polarization curves.

4.1 Integral Equation Solution of Laplace's Equation

The general theory behind impressed-current cathodic protection systems is discussed in Section 1.2.1. In this section an integral equation describing the corrosion-related electric potential is derived. This method has long been known and a derivation may also be found in [73]. In a static or time-invariant problem the electric field intensity $\mathbf{E}$ can be written as the gradient of a scalar potential: $\mathbf{E} = -\boldsymbol{\nabla}\Phi$. In a medium with conductivity σ, the electric volume current density $\mathbf{J} = \sigma\mathbf{E}$ can therefore be expressed as $\mathbf{J} = -\sigma\boldsymbol{\nabla}\Phi$. From the continuity equation $\boldsymbol{\nabla}\cdot\mathbf{J} = -d\rho/dt$ it then follows that

$$\boldsymbol{\nabla}\cdot\big(\sigma\boldsymbol{\nabla}\Phi\big) = \frac{d\rho}{dt}. \tag{4.1}$$

In a charge-free region V with uniform conductivity σ this reduces to Laplace's equation:

$$\boldsymbol{\nabla}^2\Phi = 0. \tag{4.2}$$

When we use a static Green's function $G(\mathbf{r}, \mathbf{r}')$ with the property

$$\boldsymbol{\nabla}^2 G = -\delta(\mathbf{r} - \mathbf{r}'),$$

(for instance the free-space Green's function $G(\mathbf{r}, \mathbf{r}') = \frac{1}{4\pi|\mathbf{r}-\mathbf{r}'|}$), we can use Green's identities to derive an integral equation, as in [74]. By a vector identity

$$\boldsymbol{\nabla} \cdot (\Phi \boldsymbol{\nabla} G) = \Phi \boldsymbol{\nabla}^2 G + \boldsymbol{\nabla} G \cdot \boldsymbol{\nabla} \Phi \tag{4.3}$$

$$\boldsymbol{\nabla} \cdot (G \boldsymbol{\nabla} \Phi) = G \boldsymbol{\nabla}^2 \Phi + \boldsymbol{\nabla} G \cdot \boldsymbol{\nabla} \Phi. \tag{4.4}$$

Therefore

$$\begin{aligned} \iiint_V \left[\boldsymbol{\nabla}' \cdot (\Phi' \boldsymbol{\nabla}' G) - \boldsymbol{\nabla}' \cdot (G \boldsymbol{\nabla}' \Phi')\right] dV' &= \iiint_V \left(\Phi' \boldsymbol{\nabla}'^2 G - G \cancel{\boldsymbol{\nabla}'^2 \Phi'}\right)^{0} dV' \\ &= \iiint_V -\Phi' \delta(\mathbf{r} - \mathbf{r}') dV' \\ &= -\Phi(\mathbf{r}), \quad \mathbf{r} \in V \end{aligned} \tag{4.5}$$

where $\Phi' = \Phi(\mathbf{r}')$. Using the divergence theorem, this gives us

$$\oint_{\partial V} \Phi' \frac{\partial G}{\partial n'} dS' - \oint_{\partial V} G \frac{\partial \Phi'}{\partial n'} dS' = -\Phi(\mathbf{r}), \quad \mathbf{r} \in V \tag{4.6}$$

or

$$\Phi(\mathbf{r}) + \oint_{\partial V} \Phi' \frac{\partial G}{\partial n'} dS' = \oint_{\partial V} G(\mathbf{r}, \mathbf{r}') \frac{\partial \Phi'}{\partial n'} dS', \quad \mathbf{r} \in V \tag{4.7}$$

where $\hat{\mathbf{n}}$ is the outward normal from V. When $\mathbf{r}$ approaches the boundary $S = \partial V$, (4.7) becomes [73, 75]

$$\frac{1}{2}\Phi(\mathbf{r}) + \mathrm{P.V.} \oint_S \Phi(\mathbf{r}') \frac{\partial G}{\partial n'} dS' = \oint_S G(\mathbf{r}, \mathbf{r}') \frac{\partial \Phi'}{\partial n'} dS', \quad \mathbf{r} \in S \tag{4.8}$$

where $\mathrm{P.V.}$ denotes the principal value integral. Throughout the remainder of this paper, the principal value notation will be suppressed.

For interior problems, where V is finite and has a definite boundary S, any potential distribution $\Phi(\mathbf{r})$ satisfying (4.8) is a valid solution. For exterior problems, the exterior boundary can be thought of as the surface S together with a spherical surface S_∞ defined by $r = a$ with $a \to \infty$. In problems of interest here, where the net current entering or leaving the hull S is zero, $\hat{\mathbf{r}} \cdot \boldsymbol{\nabla}\Phi$ decays at least as $1/r^3$ as $r \to \infty$. Consequently, on S_∞ we are only concerned with the term $\oint\limits_{S_\infty} \Phi(\mathbf{r}')\frac{\partial G}{\partial n'}dS'$. As $r' \to \infty$, $\Phi(\mathbf{r}')$ approaches some constant Φ_∞. And so we have

$$\oint\limits_{\Omega} \Phi_\infty \frac{d}{dr'}\left(\frac{1}{4\pi r'}\right) \cdot (r')^2 d\Omega' = \frac{\Phi_\infty}{4\pi} \cdot (-4\pi) = -\Phi_\infty \tag{4.9}$$

as in [37].

The condition that the total current leaving the hull equals the total current returning to the hull is satisfied automatically in the interior problem, since the constraint

$$\oint_{\partial V} \frac{d\Phi}{dn} dS = 0 \tag{4.10}$$

is directly implied by Laplace's equation and the divergence theorem:

$$\oint_{\partial V} \frac{d\Phi}{dn} dS = \oint_{\partial V} \boldsymbol{\nabla}\Phi \cdot \mathbf{dS} = \int_V \boldsymbol{\nabla} \cdot \boldsymbol{\nabla}\Phi dV = \int_V \boldsymbol{\nabla}^2 \Phi dV = 0. \tag{4.11}$$

This is still true mathematically in the exterior problem, assuming integration over both S and S_∞, but to ensure the more specific condition that the net flux through S be zero, one must enforce (4.10) explicitly as a separate condition. In Neumann problems, where $\frac{d\Phi}{dn}$ is specified everywhere on S at the start, it is necessary for both interior and exterior problems that it be specified to satisfy (4.10).

It is sometimes convenient to use the outward surface normal to the structure

being modeled, here denoted $\hat{\mathbf{n}}_i$, rather than the normal $\hat{\mathbf{n}}$ pointing out of the electrolyte V. This gives us the following equation for exterior problems:

$$\frac{1}{2}\Phi(\mathbf{r}) - \oint_S \Phi(\mathbf{r}')\frac{\partial G}{\partial n_i'}dS' - \Phi_\infty = -\oint_S G(\mathbf{r},\mathbf{r}')\frac{\partial \Phi'}{\partial n_i'}dS', \quad \mathbf{r}\in S. \tag{4.12}$$

4.2 Boundary Conditions and Solution Uniqueness

For a constant $\Phi(\mathbf{r})$ in V, the integral on the left hand side of (4.8) or (4.12) becomes the measure of a solid angle. This can be seen by taking the observation point $\mathbf{r}$ as the coordinate origin, in which case the integral becomes:

$$\oint_S \frac{\partial}{\partial n'}\left(\frac{1}{4\pi r'}\right)dS' = -\frac{1}{4\pi}\oint_S \frac{\hat{\mathbf{r}}'\cdot\hat{\mathbf{n}}'}{r'^2}dS' = -\frac{1}{4\pi}\oint_S \sin\theta' d\theta' d\varphi'. \tag{4.13}$$

If we orient our coordinate axes so that the z-axis is normal to the surface this integral reduces to $\frac{2\pi}{4\pi}\cos\theta\big|_0^{\pi/2} = -\frac{1}{2}$. This causes the left hand side of (4.8) to vanish, so that the operator on the left hand side of (4.8) has a nontrivial null space of dimension 1, spanned by the vector $\Phi(\mathbf{r}) = \Phi_0 \neq 0$. Consequently, if any solution $\Phi_1(\mathbf{r})$ exists, then $\Phi_2(\mathbf{r}) = \Phi_1(\mathbf{r}) + \Phi_0$ is also a solution for any Φ_0, so that the problem is only determined to within an arbitrary additive constant. This indeterminacy can be eliminated by adding an absolute potential constraint, e.g., constraining the average potential to zero, or forcing the potential at some point to zero.

The same null space exists for the exterior problem. This can shown explicitly from (4.12) by again making Φ constant everywhere, evaluating the second term, and noting that the change in sign of $\hat{\mathbf{n}}$ reverses the sign of the second term. Thus the left-hand side becomes $\Phi_0 - \Phi_\infty$, and the entire left-hand side has the null space $\Phi(\mathbf{r}) = \Phi_0$ for $\mathbf{r}\in V$.

In a problem where an electrode is held at a fixed potential, the null space

$\Phi = \Phi_0$ is eliminated. In problems of the form (4.20) discussed below, where a polarization relation $\frac{d\Phi}{dn} = f(\Phi)$ is involved, the uniqueness of the solution depends on the polarization relation f. The argument Φ in $f(\Phi)$ is the potential relative to some test electrode used in the experimental determination of the polarization curves (e.g. a silver chloride electrode or saturated calomel electrode [34]). This implicit definition of a reference potential can make the solution unique. If, for instance, the standard hydrogen electrode is the reference for the cathodic polarization function f_C, then the potential Φ_C in the solution is defined relative to the standard hydrogen electrode potential. The solution can still be indeterminate if multiple points on the polarization curve or curves are capable of satisfying problem conditions, as may happen when, for instance, $f(\Phi)$ is not one-to-one. Note the importance of defining any polarization curves used in a problem relative to the same standard electrode. The different problem types and boundary conditions and the resulting null space and necessary constraints are tabulated in Table 4.1 (cf. [74]).

4.3 Numerical Solution of Integral Equation

In this paper, equation (4.8) is discretized on both sides using the locally corrected Nyström (LCN) method described in Chapter 3, with degrees of freedom $\Phi_j = \Phi(\mathbf{r}_j)$ and $\Psi_j = \frac{\partial\Phi}{\partial n}\big|_{\mathbf{r}=\mathbf{r}_j}$ related by matrices generated from the Green's function:

$$[H]\bar{\Phi} = [G]\bar{\Psi}. \tag{4.14}$$

The matrix entries are defined by

$$[H]_{ij} = \begin{cases} \omega_j \mathcal{J}(\mathbf{r}_j)\ \frac{\partial G(\mathbf{r}_i,\mathbf{r}')}{\partial n'}\Big|_{\mathbf{r}'=\mathbf{r}_j} & \mathbf{r}_i, \mathbf{r}_j \text{ not on same cell} \\ \frac{1}{2}\delta_{ij} + \tilde{\omega}^H_{i,j} & \mathbf{r}_i, \mathbf{r}_j \text{ on same cell} \end{cases} \tag{4.15}$$

$$[G]_{i,j} = \begin{cases} \omega_j \mathcal{J}(\mathbf{r}_j) G(\mathbf{r}_i, \mathbf{r}_j) & \mathbf{r}_i, \mathbf{r}_j \text{ not on same cell} \\ \tilde{\omega}_{i,j}^G & \mathbf{r}_i, \mathbf{r}_j \text{ on same cell.} \end{cases} \tag{4.16}$$

Here δ_{ij} is the Kronecker delta function and ω_j and $\mathcal{J}(\mathbf{r}_j)$ signify, respectively, the quadrature weight and Jacobian corresponding to the quadrature point $\mathbf{r}_j$ in the LCN discretization. The local correction quadrature weights $\tilde{\omega}_j^H$ and $\tilde{\omega}_j^G$ are calculated following the method outlined in Chapter 2 to integrate $\Phi \frac{\partial G}{\partial n}$ and $G \frac{\partial \Phi}{\partial n}$, respectively, over the cell containing $\mathbf{r}_i$. The overbars on the electric potential Φ and normal flux density $\Psi = \partial\Phi/\partial n$ indicate column vectors containing the relevant degrees of freedom Φ_j and Ψ_j.

The hull boundary S consists of three kinds of surface: *anodic* surfaces where a current is emitted from the hull, *cathodic* surfaces where current returns to the hull, and *insulating* surfaces where the normal current density is identically zero. The matrices may be partitioned accordingly into the blocks corresponding to degrees of freedom on the cathodic surfaces (Φ_C^n,Ψ_C^n), those on anodic surfaces (Φ_A^n,Ψ_A^n), and those on insulating surfaces (Φ_I^n,Ψ_I^n). Since $\Psi_I = 0$, the exterior problem can thus be discretized as

$$[H]\bar{\Phi} = \begin{bmatrix} [H_{CC}] & [H_{CA}] & [H_{CI}] & [-1] \\ [H_{AC}] & [H_{AA}] & [H_{AI}] & [-1] \\ [H_{IC}] & [H_{IA}] & [H_{II}] & [-1] \\ 0 & 0 & 0 & 0 \end{bmatrix} \begin{bmatrix} \bar{\Phi}_C \\ \bar{\Phi}_A \\ \bar{\Phi}_I \\ \Phi_\infty \end{bmatrix} = \begin{bmatrix} [G_{CC}] & [G_{CA}] \\ [G_{AC}] & [G_{AA}] \\ [G_{IC}] & [G_{IA}] \\ [S_C] & [S_A] \end{bmatrix} \begin{bmatrix} \bar{\Psi}_C \\ \bar{\Psi}_A \end{bmatrix} = [G]\bar{\Psi} \tag{4.17}$$

where the row vector $[A] = \begin{bmatrix} [S_C] & [S_A] \end{bmatrix}$, which is added to enforce (4.10) in the exterior problem, is defined by

$$[S]_j = \omega_j \mathcal{J}(\mathbf{r}_j). \tag{4.18}$$

The interior problem does not require this constraint, and (4.17) reduces to

$$\begin{bmatrix} [H_{CC}] & [H_{CA}] & [H_{CI}] \\ [H_{AC}] & [H_{AA}] & [H_{AI}] \\ [H_{IC}] & [H_{IA}] & [H_{II}] \end{bmatrix} \begin{bmatrix} \bar{\Phi}_C \\ \bar{\Phi}_A \\ \bar{\Phi}_I \end{bmatrix} = \begin{bmatrix} [G_{CC}] & [G_{CA}] \\ [G_{AC}] & [G_{AA}] \\ [G_{IC}] & [G_{IA}] \end{bmatrix} \begin{bmatrix} \bar{\Psi}_C \\ \bar{\Psi}_A \end{bmatrix}. \tag{4.19}$$

4.3.1 Neumann Problems

In an interior Neumann problem, $\bar{\Psi}$ is given, so that the right hand side is known and (4.19) can be solved directly for $\bar{\Phi}$. For the solution to make sense physically, Ψ must be chosen such that (4.10) is satisfied at the outset. This is also true for the exterior problem, so that the final row in (4.17) is not required. Moreover, if one lets $\Phi_\infty = 0$, then the exterior Neumann problem also reduces to (4.19), though unlike the interior problem there is no arbitrary constant Φ offset. This offset can be eliminated in the interior problem by replacing a linearly dependent row in $[H]$ with a direct constraint on the potential at some point or points, or by appending such a constraint as an additional row in the matrix. One could, for example, demand that Φ equal zero at some point, or that the average value of Φ on S have some specific value.

4.3.2 Nonlinear Boundary Conditions

Of particular interest in this paper is a more general form of (4.17):

$$\begin{bmatrix} [H_{CC}] & [H_{CA}] & [H_{CI}] & [-1] \\ [H_{AC}] & [H_{AA}] & [H_{AI}] & [-1] \\ [H_{IC}] & [H_{IA}] & [H_{II}] & [-1] \\ [0] & [0] & [0] & 0 \end{bmatrix} \begin{bmatrix} \bar{\Phi}_C \\ \bar{\Phi}_A \\ \bar{\Phi}_I \\ \Phi_\infty \end{bmatrix} = \begin{bmatrix} [G_{CA}] & [G_{CC}] \\ [G_{AA}] & [G_{AC}] \\ [G_{IA}] & [G_{IC}] \\ [S_C] & [S_A] \end{bmatrix} \begin{bmatrix} f_C(\bar{\Phi}_C) \\ f_A(\bar{\Phi}_A) \end{bmatrix}. \tag{4.20}$$

The functions f_A and f_C are the anodic and cathodic *polarization curve* functions relating the potential Φ to the normal current density on the corresponding surface. When f_A and f_C are constant, (4.20) reduces to the Neumann problem in (4.17). In general, however, f_A and f_C are not constant or even linear, so an iterative solution method is often required, as discussed below.

4.4 Iterative solution

Many practical corrosion problems require solution of (4.20), where f_A is a constant function and f_C is nonlinear. An example of such a polarization function f_C is the Butler-Volmer equation [34, 52], which is nonlinear but can be written analytically. As shown in [53, 54], different materials and physical conditions can give rise to much more complicated curves, which must often be determined experimentally.

In general, an iterative technique must be used to solve problems involving these nonlinear boundary conditions. A simple iterative method given in [34] takes an initial guess of $\bar{\Phi}_0$ or $\bar{\Psi}_0$, solves the resulting linear equation, and uses the solution as the initial guess in the next iteration. The process is repeated until subsequent solutions agree. More sophisticated approaches use a Newton-Raphson iteration, which generally converges more quickly. In what follows the application of the Newton-Raphson method to nonlinear corrosion problems is described, followed by the presentation of a method for rendering the Newton-Raphson iteration more efficient for problems with small cathodic areas.

4.4.1 Iterative Solution Using the Newton-Raphson Method

A popular approach to finding the corrosion-related hull potential Φ is to solve (4.20) using the Newton-Raphson method [55, 56]. In order to find $\bar{\Phi}$ such that

$[G]f(\bar{\Phi}) - [H]\bar{\Phi} = 0$, we define

$$F(\bar{\Phi}) = [G]f(\bar{\Phi}) - [H]\bar{\Phi} \tag{4.21}$$

Then we can solve $F(\bar{\Phi}) = 0$ iteratively. We compute the Jacobian matrix

$$[J_m] = \left.\frac{\partial F}{\partial \bar{\Phi}}\right|_{\bar{\Phi}=\bar{\Phi}_m} = \begin{bmatrix}[G] & [0]\end{bmatrix} \text{diag}\left(\left.\left[\frac{df}{d\bar{\Phi}}\right]\right|_{\bar{\Phi}=\bar{\Phi}_m}\right) - [H] \tag{4.22}$$

beginning with an initial guess $\bar{\Phi}_0$. The zero columns contained in $[0]$ are appended to $[G]$ in order to give a matrix with the same dimensions as $[H]$. Each subsequent iteration is calculated as

$$\bar{\Phi}_{m+1} = \bar{\Phi}_m - [J_m]^{-1}F_m \tag{4.23}$$

until $F(\bar{\Phi})$ is sufficiently small.

4.4.2 Newton-Raphson with Schur Complement

Inversion of the full Jacobian matrix at every iteration can be cumbersome. Various methods have been proposed to reduce the size of the matrix to be inverted at each step [55, 56]. In this paper is proposed another approach in which, by a proper rearrangement and partitioning of the matrices $[H]$ and $[G]$, the inversion of the Jacobian matrix can be performed by manipulating and inverting blocks of the matrix using the Schur complement [76]. In a problem where large portions of S are either insulated or have a constant, non Φ-dependent current density, the unknowns in $\bar{\Phi}$ can be arranged as $\begin{bmatrix}\bar{\Phi}^{nc} \\ \bar{\Phi}^{co}\end{bmatrix}$ where $\bar{\Phi}^{nc}$ contains unknowns on surfaces where $f'(\Phi)$ is not identically zero and $\bar{\Phi}^{co}$ contains the remaining unknowns for which $f'(\Phi)$ is identically zero. Applying this rearrangement to (4.22) we now

have

$$[J_m] = \left.\frac{\partial F}{\partial \bar{\Phi}}\right|_{\bar{\Phi}=\bar{\Phi}_m} = \begin{bmatrix} [G^{nc,nc}] & [0] \\ [G^{co,nc}] & [0] \end{bmatrix} \text{diag}\left(\begin{bmatrix} f'(\bar{\Phi}_m^{nc}) \\ 0 \end{bmatrix} \right) - \begin{bmatrix} [H^{nc,nc}] & [H^{nc,co}] \\ [H^{co,nc}] & [H^{co,co}] \end{bmatrix} \tag{4.24}$$

$$= \begin{bmatrix} [J_m^{nc,nc}] & [J^{nc,co}] \\ [J_m^{co,nc}] & [J^{co,co}] \end{bmatrix} \tag{4.25}$$

$$= \begin{bmatrix} \left([G^{nc,nc}] f'(\bar{\Phi}_m^{nc}) - [H^{nc,nc}]\right) & -[H^{nc,co}] \\ \left([G^{co,nc}] f'(\bar{\Phi}_m^{nc}) - [H^{co,nc}]\right) & -[H^{co,co}] \end{bmatrix} \tag{4.26}$$

When a matrix is partitioned as in (4.24) into the form

$$[T] = \begin{bmatrix} [A] & [B] \\ [C] & [D] \end{bmatrix}$$

where $[A]$ and $[D]$ are square matrices and $[D]$ is invertible, the Schur complement of $[D]$ in $[T]$, written as $[T]/[D] = [A] - [B][D]^{-1}[C]$, can be used to streamline the computation of $[T]^{-1}$ when the blocks $[B]$ and $[D]$ are constant but $[A]$ and $[C]$ vary between iterations. Since

$$\begin{bmatrix} [A] & [B] \\ [C] & [D] \end{bmatrix} = \begin{bmatrix} [I] & [B][D]^{-1} \\ [0] & [I] \end{bmatrix} \begin{bmatrix} [A] - [B][D]^{-1}[C] & 0 \\ 0 & [D] \end{bmatrix} \begin{bmatrix} [I] & [0] \\ [D]^{-1}[C] & [I] \end{bmatrix}, \tag{4.27}$$

therefore

$$\begin{bmatrix} [A] & [B] \\ [C] & [D] \end{bmatrix}^{-1} = \begin{bmatrix} [I] & [0] \\ -[D]^{-1}[C] & [I] \end{bmatrix} \begin{bmatrix} ([A]-[B][D]^{-1}[C])^{-1} & [0] \\ [0] & [D]^{-1} \end{bmatrix} \begin{bmatrix} [I] & -[B][D]^{-1} \\ [0] & [I] \end{bmatrix} \tag{4.28}$$

$$= \begin{bmatrix} ([T]/[D])^{-1} & -([T]/[D])^{-1}[B][D]^{-1} \\ -[D]^{-1}[C]([T]/[D])^{-1} & [D]^{-1}+[D]^{-1}[C]([T]/[D])^{-1}[B][D]^{-1} \end{bmatrix} \tag{4.29}$$

where $[I]$ is an $[A]$- or $[D]$-sized identity matrix as appropriate. Thus the matrix $[D]^{-1}$ need only be inverted for the first iteration, and used in successive iterations along with $[B]$, $[C]$, and $([T]/[D])^{-1}$ to find the inverse of each $[J_m]$. In this way each iteration, apart from the first, requires the inversion of only a $N_{nc} \times N_{nc}$ matrix.

The Schur complement $[J_m]/[(-H^{co,co})]$ can be written explicitly as

$$[J_m]/[(-H^{co,co})] =$$
$$\left([G^{nc,nc}]f'(\bar{\Phi}_m^{nc}) - [H^{nc,nc}]\right) - [H^{nc,co}][H^{co,co}]^{-1}\left([G^{co,nc}]f'(\bar{\Phi}_m^{nc}) - [H^{co,nc}]\right) \tag{4.30}$$

For convenience, we denote $[J_m]/[(-H^{co,co})]$ by $[J_m^{SC}]$. The following procedure is then used:

1. Use initial guess $\bar{\Phi}_m = \begin{bmatrix} \bar{\Phi}_m^{nc} \\ \bar{\Phi}_m^{co} \end{bmatrix}$, with $m = 0$.
2. Compute and partition $[H]$ and $[G]$.
3. Compute inverse of $[H^{co,co}]$.
4. Compute
$$\begin{bmatrix} \bar{F}_m^{nc} \\ \bar{F}_m^{co} \end{bmatrix} = [H] \begin{bmatrix} \bar{\Phi}_m^{nc} \\ \bar{\Phi}_m^{co} \end{bmatrix} - \begin{bmatrix} [G] & [0] \end{bmatrix} f\left(\begin{bmatrix} \bar{\Phi}_m^{nc} \\ \bar{\Phi}_m^{co} \end{bmatrix} \right) \tag{4.31}$$
5. Use inverse computed above to compute $[J_m^{SC}]$ as in (4.30).

6. Compute $\delta\bar{\Phi}_m^{nc} = [J_m^{SC}]^{-1}\left(\bar{F}^{nc} - [H^{nc,co}][H^{co,co}]^{-1}\bar{F}^{co}\right)$.
7. Compute $\delta\bar{\Phi}_m^{co}$ as

$$-[H^{co,co}]^{-1}\Big[\bar{F}^{co} + \left([G^{co,nc}]f'(\bar{\Phi}_m^{nc}) - [H^{co,nc}]\right)[J_m^{SC}]^{-1}\left([H^{nc,co}][H^{co,co}]^{-1}\bar{F}^{co} - \bar{F}^{nc}\right)\Big].$$

8. Compute $\begin{bmatrix}\bar{\Phi}_{m+1}^{nc}\\ \bar{\Phi}_{m+1}^{co}\end{bmatrix} = \begin{bmatrix}\bar{\Phi}_m^{nc}\\ \bar{\Phi}_m^{co}\end{bmatrix} - \begin{bmatrix}\delta\bar{\Phi}_m^{nc}\\ \delta\bar{\Phi}_m^{co}\end{bmatrix}$.
9. Compute $\bar{F}_{m+1} = H\bar{\Phi}_{m+1} - Gf(\bar{\Phi}_{m+1})$.
10. If the residual $|\bar{F}_{m+1}|$ is larger than tolerance, increment m and return to step 5. Else solution is $\bar{\Phi}_{m+1}$.

The matrix $-[H^{co,co}]$ can be inverted and stored, and in typical problems $[J_m^{SC}]$ will be relatively small, making direct inversion more feasible. It is hoped that this approach will allow for effective use of fast solvers in solving large problems with nonlinear boundary conditions.

4.5 Modeling of Water Surface

When a vessel is at or near the surface, the interface between the conductive seawater and the insulating air can be modeled as an image plane. The boundary condition at this interface, which can typically be treated as a plane surface, is that the normal component of the current at the interface must be zero. We can thus solve the problem using the method above for an infinite conductor via the method of images. If all sources and hull boundaries below the surface are mirrored across the interface by equal sources and potentials, the boundary conditions are satisfied and the problem can be solved for the potential and current below the water surface without needing to mesh the water surface itself. As far as the electrical sources, potentials, and fields are concerned, this is equivalent to treating the

water surface as a perfect magnetic conductor (PMC). The corresponding Green's function can be used to solve the electrostatic problem (cf. [62]).

4.6 Numerical Test Results

In this section are detailed several simulations and results demonstrating the performance of the method proposed here. First we investigate general test cases to verify the accuracy and convergence properties of the solution. Nonlinear problems are also investigated to compare the efficiency of the different iterative solution techniques described above. Finally, problems involving structures at or near the electrolyte boundary are solved using an image method.

4.6.1 Sphere with Robin Boundary Conditions

We look first at a benchmark problem investigated in [73], where a $1\,\mathrm{m}$ radius sphere is embedded in an infinite medium with $\sigma = 1\,\mathrm{S\,m^{-1}}$. The flux boundary condition on the sphere is given by

$$\frac{d\Phi}{dn} = \Phi(\theta) + \cos\theta + 3,\ r = 1\,\mathrm{m}, 0 \leq \theta \leq \pi. \tag{4.32}$$

The analytic solution

$$\Phi = -3 - \frac{1}{3r^2}\cos\theta,\ \ r \geq 1\,\mathrm{m} \tag{4.33}$$

has $\partial\Phi/\partial r = \frac{2}{3}r^{-3}\cos\theta$, which is equivalent to (4.32) at $r = 1\,\mathrm{m}$.

In Fig. 4.1, the RMS error of the computed surface potential is plotted against the number of unknowns in the problem. At lower basis orders the exponential convergence is consistent and becomes more rapid as the basis order is increased. The stagnation at higher orders, occurring at an error of about 10^{-9} to 10^{-8}, is thought to be caused by numerical difficulties in computing the integral

$\oint_s \Phi(\mathbf{r}')\boldsymbol{\nabla}' G \cdot \hat{\mathbf{n}}' dS'$ on the curvilinear cells used to mesh the sphere. Essentially the same effect has been noted for the magnetic field integral equation (MFIE) operator [11]. Details on the cause of this difficulty are briefly discussed in Appendix B.

4.6.2 Iterative Solution with Nonlinear Boundary Conditions

The behavior of the polarization curve naturally has a significant effect on the efficacy and speed of solution techniques. To demonstrate this we look at $20\,\mathrm{m} \times 10\,\mathrm{m} \times 1\,\mathrm{m}$ box in an infinite electrolyte of conductivity $4\,\mathrm{S\,m^{-1}}$. $1\,\mathrm{m} \times 1\,\mathrm{m}$ electrodes are placed at the opposite ends of each $10\,\mathrm{m} \times 1\,\mathrm{m}$ face, one anode and one cathode on each face, with both cathodes on the same side and both anodes on the same side, as shown in Fig. 4.2. A uniform current density is assigned to each anode, while the cathode follows a nonlinear polarization curve. Two polarization curves used are plotted in Fig. 4.3 and Fig. 4.4, along with the number of iterations required and the final average (Φ, J) values on the cathode for each initial Φ value imposed on the cathodes. The Newton-Raphson method is used with an adaptive relaxation (cf. [77]).

The variation in the required number of iterations shows the impact of the initial guess on the efficiency of the solution. Moreover, the Newton-Raphson iteration does not necessarily converge to the nearest solution point if multiple valid solutions exist, as is shown in Fig. 4.4.

4.6.3 Comparison of Iterative Methods

We compare the performance of the Newton-Raphson iterative solution with and without the Schur complement approach presented here by applying them to a sphere of radius $1\,\mathrm{m}$ with anodic and cathodic surfaces at opposite ends. The anodic current density is a constant $1\,\mathrm{A\,m^{-2}}$, and the cathode obeys the polarization relation $d\Phi/dn = 0.2\Phi$. The timing tests are run to exactly 10 iterations using

MATLAB on a Dell Optiplex desktop computer. Results are shown for a sphere with a cathodic surface defined by $\theta \geq 140°$ and an anodic surface by $\theta \leq 40°$ in Fig. 4.5. In this problem, where about $18\,\%$ of the surface DoF are cathodic, the use of the Schur complement gives about a $40\,\%$ reduction in computation time. In Fig. 4.6, a similar test is performed with the cathodic surface defined by $\theta \geq 175°$ and the anodic surface by $\theta \leq 5°$. Here, with only about $9\,\%$ to $17\,\%$ of the surface DoF cathodic (depending on the discretization), the time reduction due to the Schur complement is about $50\,\%$.

In the given problem, where the electrode and insulator surfaces are alike refined and maintain their relative sizes, all three methods show a similar growth in computation time with the order p of the quadrature rule. In a practical problem, where some parts may need to be meshed in more detail, the consequently greater number of DoF associated with a cathodic or insulating surface could make the Schur complement approach either significantly faster than or roughly equivalent to the bare Newton-Raphson method.

It is worth noting that unlike the problems discussed in the previous chapters, these problems do not rely on conformal meshing. This fact is found to be helpful in some problems where the water surface and other distant boundaries must be modeled in addition to the hull.

4.6.4 Semi-Cylindrical Hull at Water Surface

To illustrate the imaging technique used when the structure is near the boundary of a semi-infinite electrolyte, we look at a problem described in [60] involving a $100\,\mathrm{m}$ semi-cylindrical hull with $1\,\mathrm{m}$ radius, with the axis lying on the x-axis, even with the surface of an electrolyte with $\sigma = 4\,\mathrm{S\,m^{-1}}$. The hull is insulating except for the ends, each of which sources or sinks $20\,\mathrm{A}$ of current. The electrolyte is bounded

at $500\,\mathrm{m}$ on each side in the x and y directions, with a depth of $1000\,\mathrm{m}$. The mesh geometry is shown in Fig. 4.7.

The electric field is calculated as the difference in electric potential between $1\,\mathrm{m}$-spaced points along the probe line $20\,\mathrm{m}$ below the axis of the hull. Results are compared for the interior problem as well as an exterior problem where the submerged portion of the hull alone is meshed and imaged as described in Section 4.5. Figure 4.8 shows the close resemblance between the two solutions, and Fig. 4.9 shows the smoother behavior of the imaged solution as the field points become more distant from the hull itself. The apparent cause of the more jagged appearance of the interior problem solution is the coarse meshing of the water surface near the field points.

4.6.5 Dipole in Tank

The image method discussed in Section 4.5 for problems near the water surface is here applied to a problem examined in [78], where two small electrodes are immersed $75\,\mathrm{cm}$ in a $914.4\,\mathrm{cm}$-diameter cylindrical tank filled with an electrolyte with conductivity $1.35\,\mathrm{mS\,cm^{-1}}$, and the electrodes source and sink a current of $4.69\,\mathrm{mA}$. With the x-y plane coincident with the water surface, the origin on the axis of the tank, $\hat{\mathbf{z}}$ pointing downward into the electrolyte, the positive and negative electrodes are modeled as vertical $1\,\mathrm{mm}$-radius, $3\,\mathrm{mm}$-high cylinders centered at coordinates $(-125\,\mathrm{cm}, 0\,\mathrm{cm}, 75\,\mathrm{cm})$ and $(125\,\mathrm{cm}, 0\,\mathrm{cm}, 75\,\mathrm{cm})$, respectively. The electric field is measured on a line extending from $(-400\,\mathrm{cm}, 0\,\mathrm{cm}, 125\,\mathrm{cm})$ to $(400\,\mathrm{cm}, 0\,\mathrm{cm}, 125\,\mathrm{cm})$, and the differential voltage $\Delta\Phi$ in the x and z directions is calculated as the potential difference between points spaced $2.5\,\mathrm{cm}$ apart.

The results computed with the LCN method with $p = 1$, shown in Fig. 4.10 for a tank depth of $137.5\,\mathrm{cm}$ and in Fig. 4.11 for a tank depth of $262.5\,\mathrm{cm}$, are seen to be in good agreement with the results presented in [78]. The results obtained when

the water surface is meshed, moreover, are seen to be equivalent to those obtained when the water surface is treated as an image plane. As seen in Fig. 4.12, the image plane results are noticeably smoother.

4.7 Summary

In this chapter surface integral techniques for calculating both the electric potential and currents resulting from impressed-current corrosion protection systems have been presented. Numerical results show the degree of accuracy and high-order convergence achievable with the locally corrected Nyström discretization of the surface integral equation. A new approach for iterative solution of problems with nonlinear boundary conditions has also been presented, and is shown to improve the efficiency of the Newton-Raphson iteration process.

TABLE 4.1: Solution Uniqueness and Required Constraints for Different Problem Types

BC\ Problem type	**Interior**	**Exterior**
Dirichlet	• Has unique solution for $\partial\Phi/\partial n$ • No Φ_∞ DoF • No current neutrality constraint required	
Neumann	• Solution Φ unique except arbitrary additive constant (requires additional constraint on Φ) • $\partial\Phi/\partial n$ must be explicitly chosen to satisfy net current neutrality	• Solution Φ unique • No Φ_∞ DoF • $\partial\Phi/\partial n$ must be explicitly chosen to satisfy net current neutrality
Dirichlet on $S_1 \subsetneq S$ Neumann on $S - S_1$	• Has unique solution Φ • Neutrality constraint not required • No Φ_∞ DoF	• Has unique solution Φ • Neutrality constraint required
$\frac{\partial\Phi}{\partial n} = f(\Phi)$, f nonlinear	• Uniqueness of solution Φ dependent on f • Neutrality constraint not required • No Φ_∞ DoF	• Uniqueness of solution Φ dependent on f • Neutrality constraint required

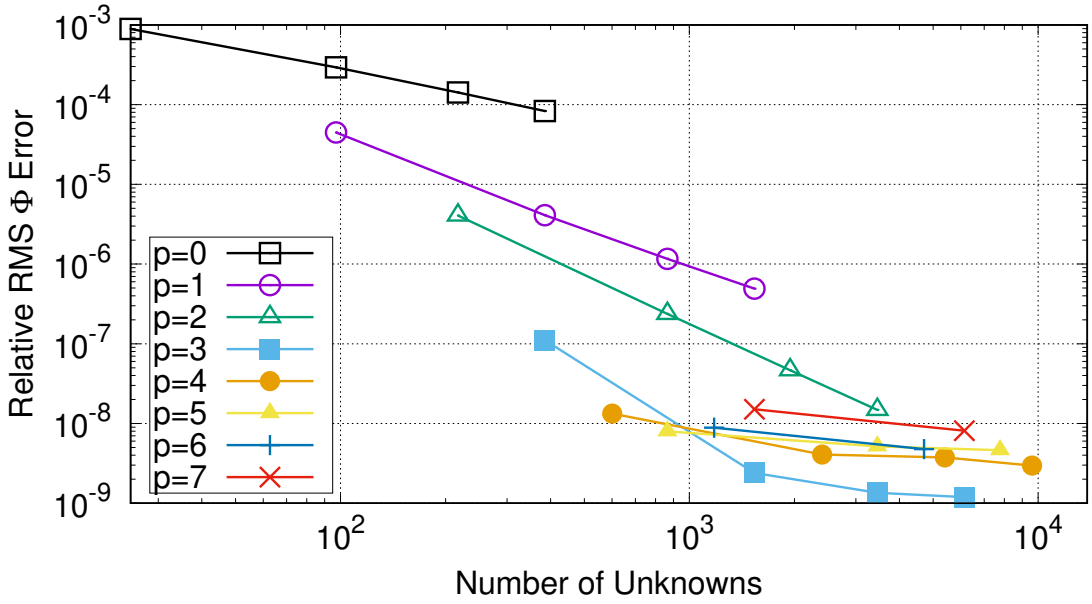

FIGURE 4.1: Relative RMS error vs. number of unknowns for exterior sphere problem. Integration tolerance is 10^{-13}.

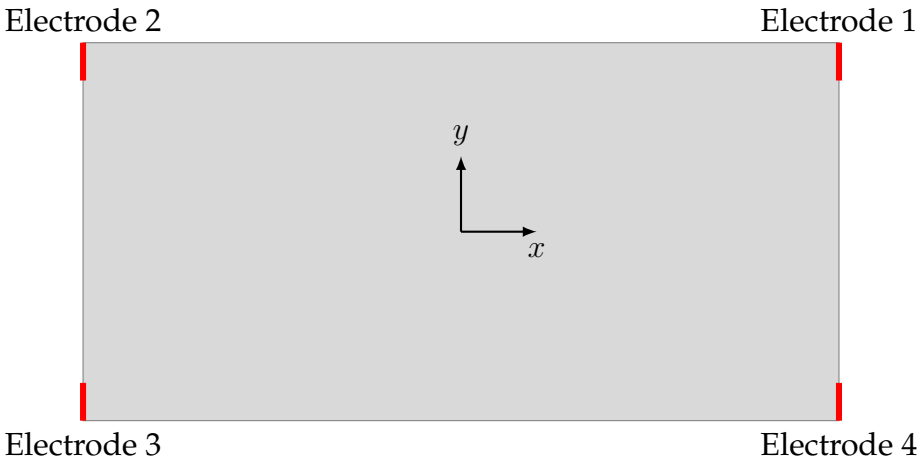

(a) Top view with electrode numbering.

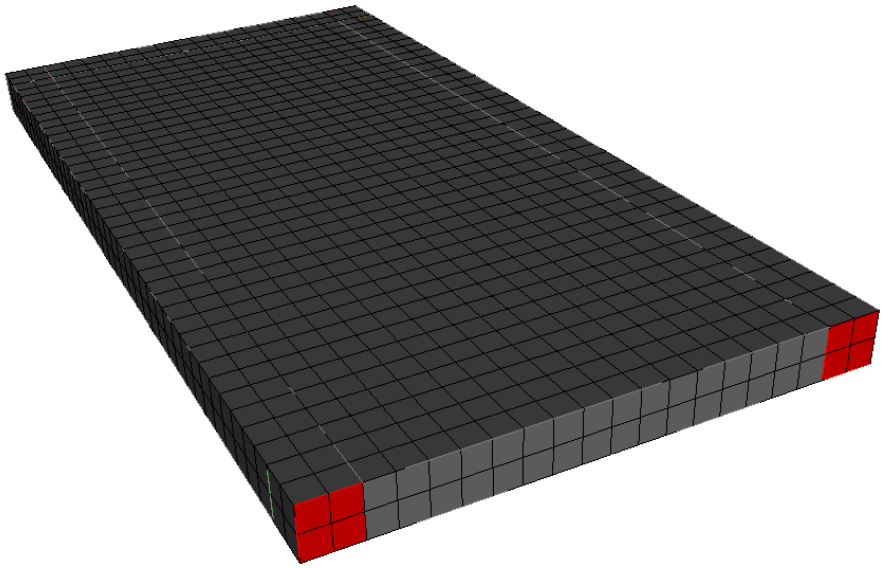

(b) Surface mesh.

FIGURE 4.2: Box ship geometry and electrode location.

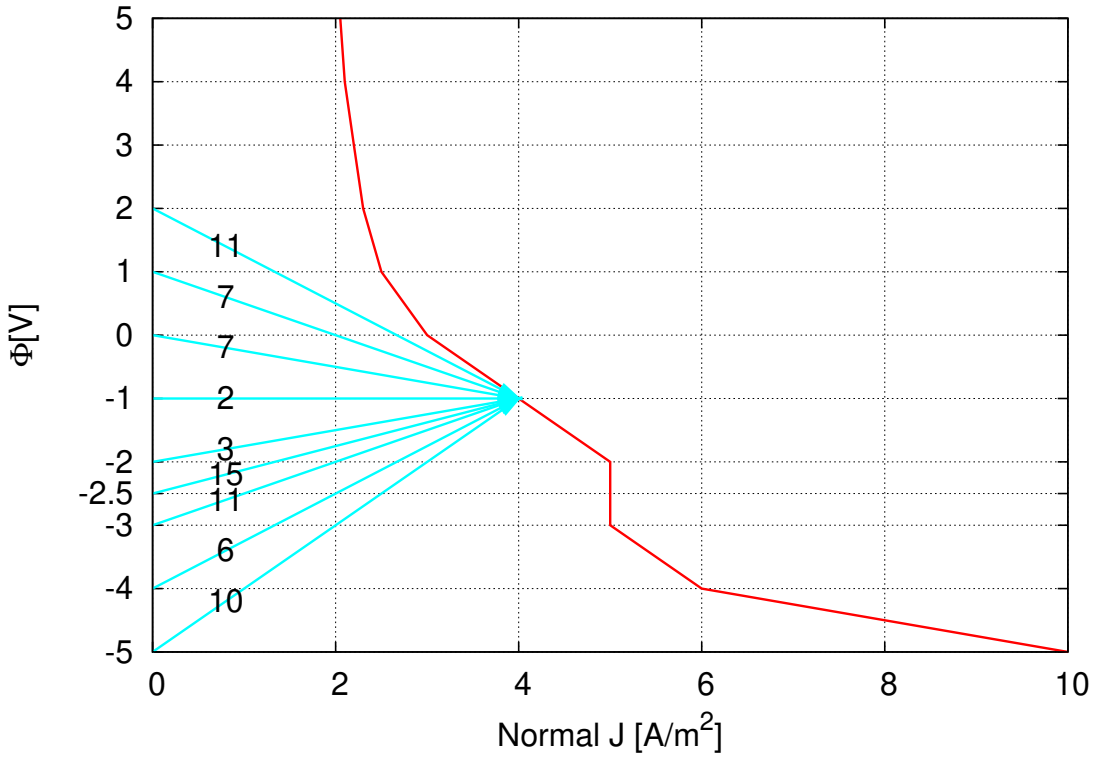

FIGURE 4.3: Iterative convergence for box ship problem with arbitrary monotonic polarization curve beginning from different initial Φ values. Initial Φ values are at arrow tails on y-axis. Arrow tip indicates average potential and normal current density of final solution. Arrow labels signify number of iterations. Anode current density is $4\,\mathrm{A\,m^{-2}}$. Integration tolerance is 10^{-6}.

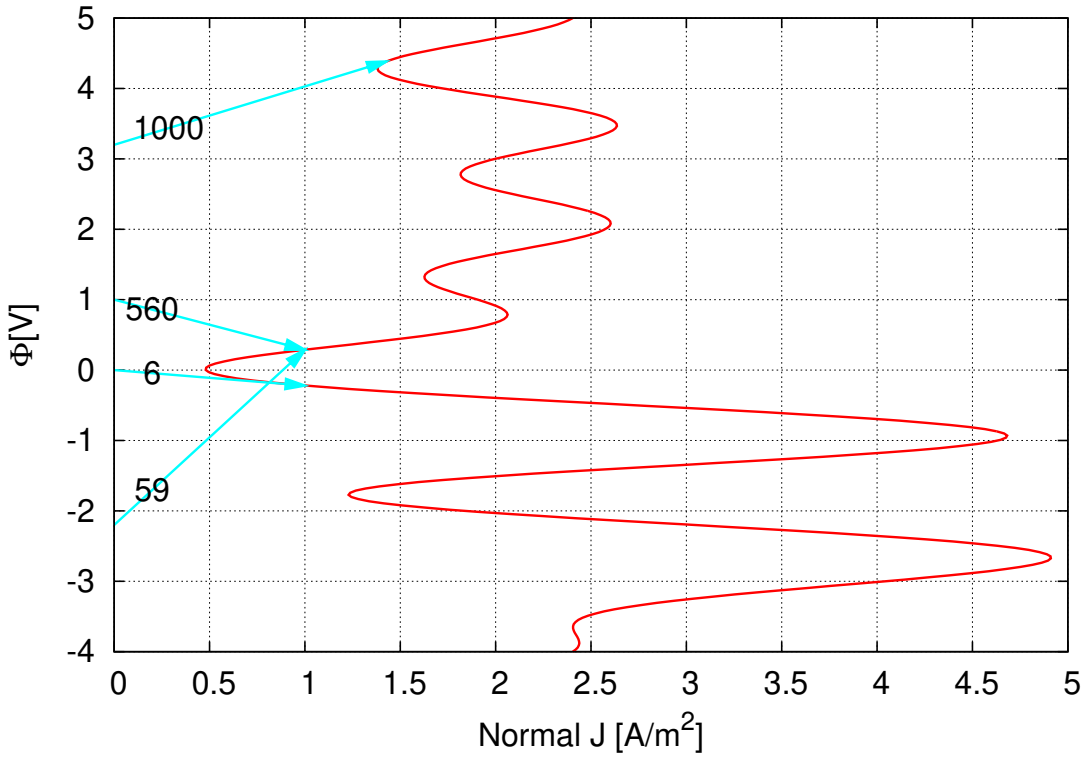

FIGURE 4.4: Iterative convergence for box ship problem with non-injective polarization curve beginning from different initial Φ values. Initial Φ values are at arrow tails on y-axis. Arrow tip indicates average potential and normal current density of final solution. Arrow labels signify number of iterations. Anode current density is $1\ \mathrm{A\,m^{-2}}$ and problem is limited to 1000 iterations. Integration tolerance is 10^{-6}.

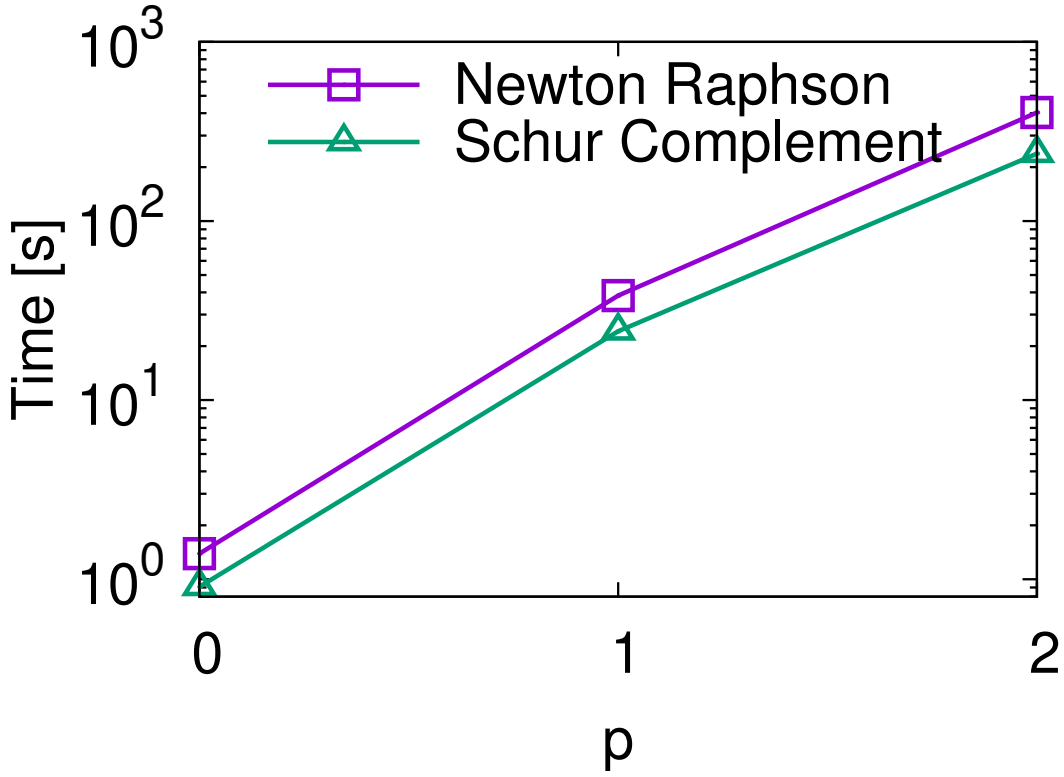

FIGURE 4.5: Timing comparison of different iterative methods for $1\,\mathrm{m}$ sphere with $40°$ anodic/cathodic regions at poles.

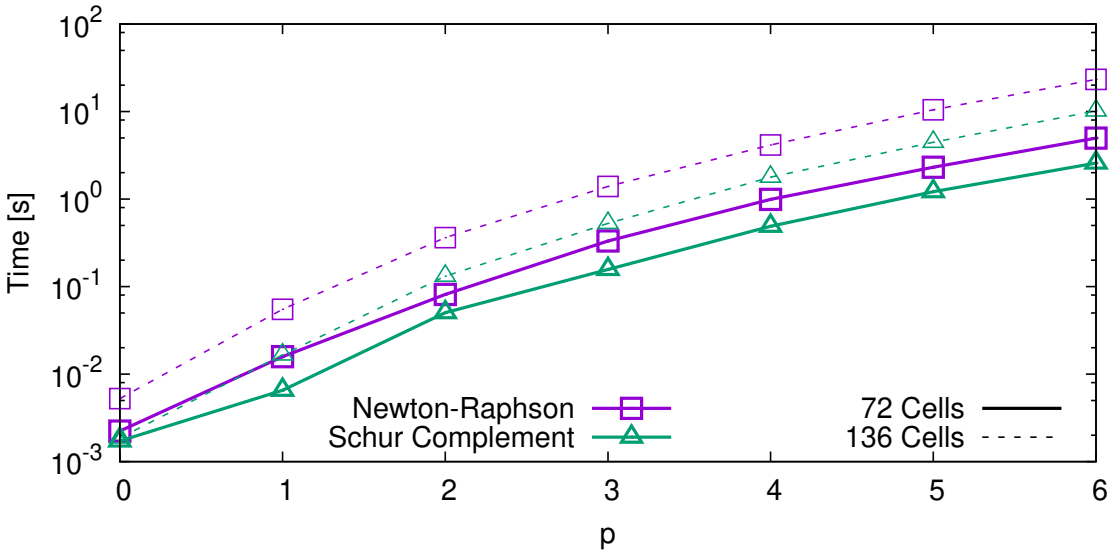

FIGURE 4.6: Timing comparison of different iterative methods for $1\,\mathrm{m}$ sphere with $5°$ anodic/cathodic regions at poles.

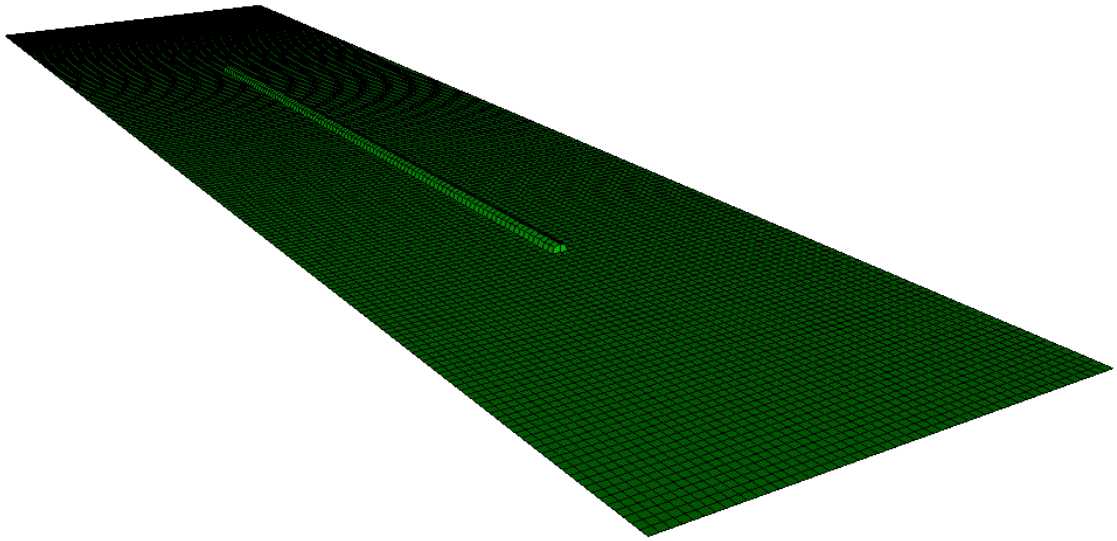

(a) Hull and nearby water surface (viewed from within tank)

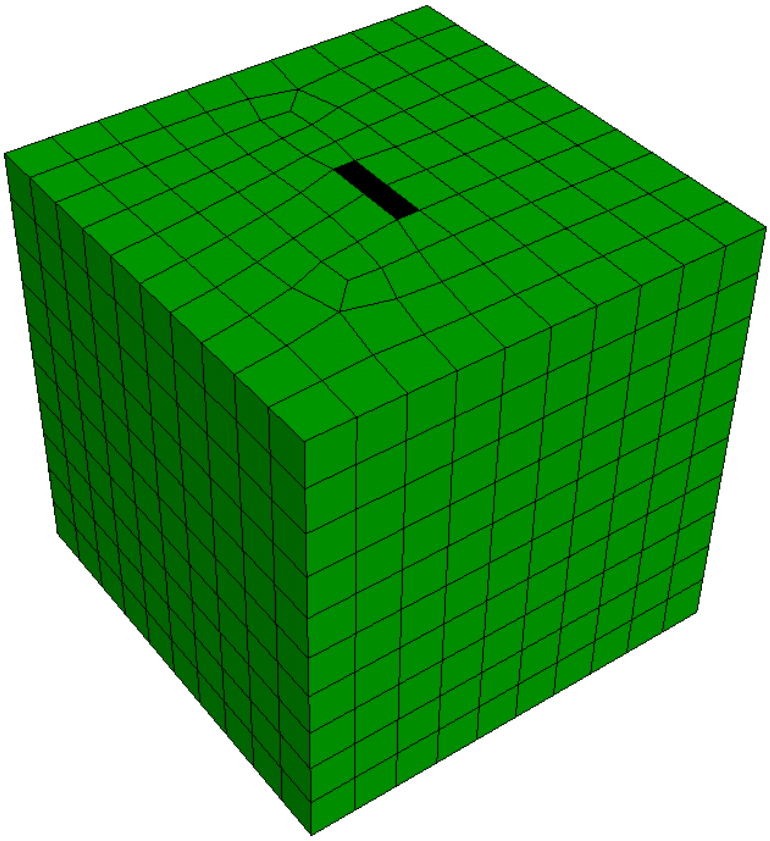

(b) Far water surface and tank boundaries

FIGURE 4.7: Surface mesh used for semi-cylindrical hull problem.

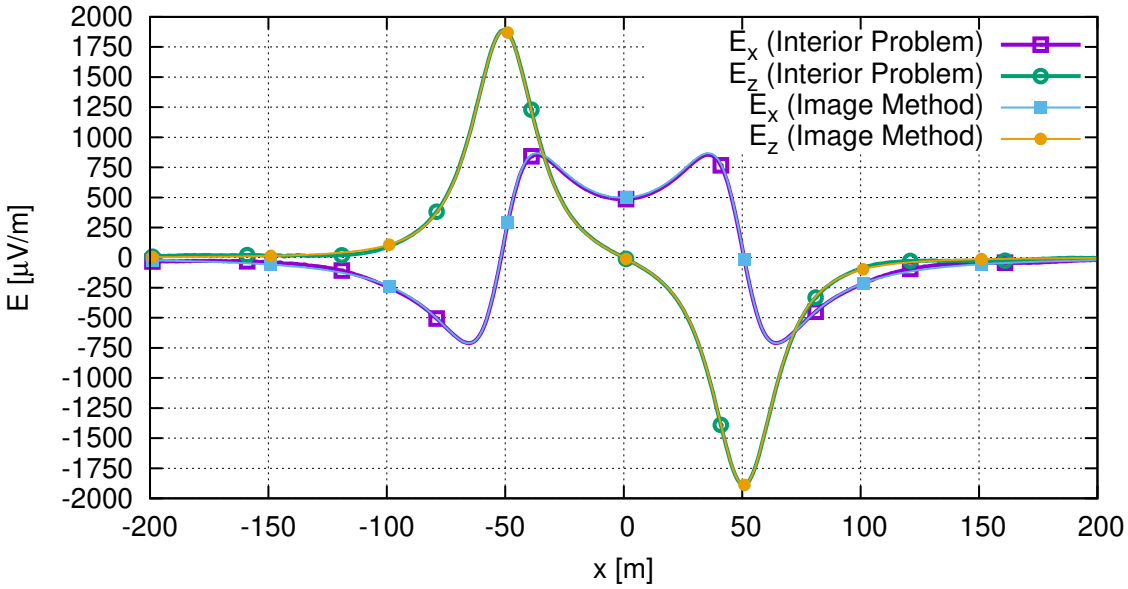

FIGURE 4.8: Electric field at a depth of $20\,\mathrm{m}$ below x-axis for semi-cylindrical hull problem [60, Fig. 11]. Integration tolerance is 10^{-6}.

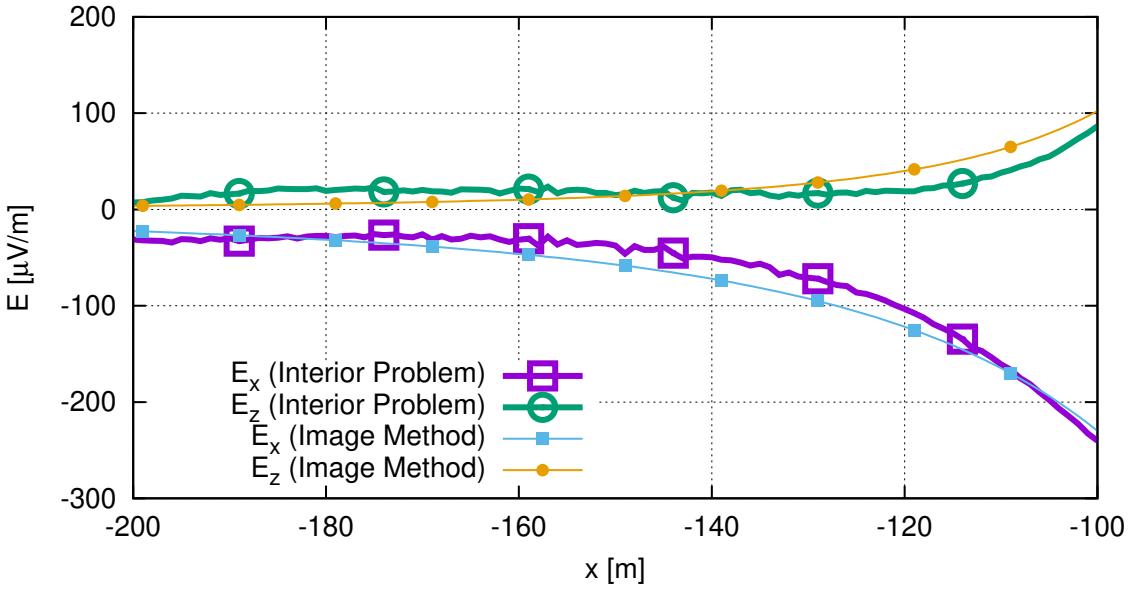

FIGURE 4.9: Magnified electric field at a depth of $20\,\mathrm{m}$ below x-axis for semi-cylindrical hull problem [60, Fig. 11]. Integration tolerance is 10^{-6}.

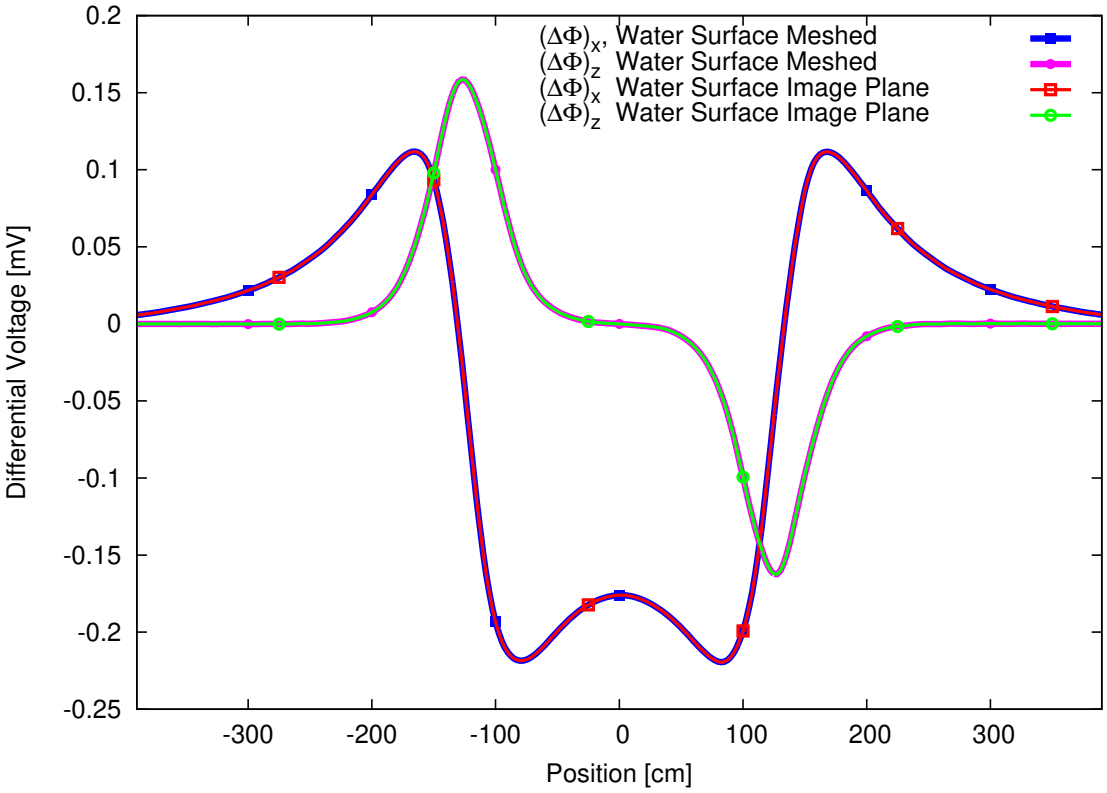

FIGURE 4.10: x- and z- directed potential differential for dipole immersed in $137.5\,\mathrm{cm}$-deep tank (cf. [78, Fig. 4]). Integration tolerance is 10^{-4}.

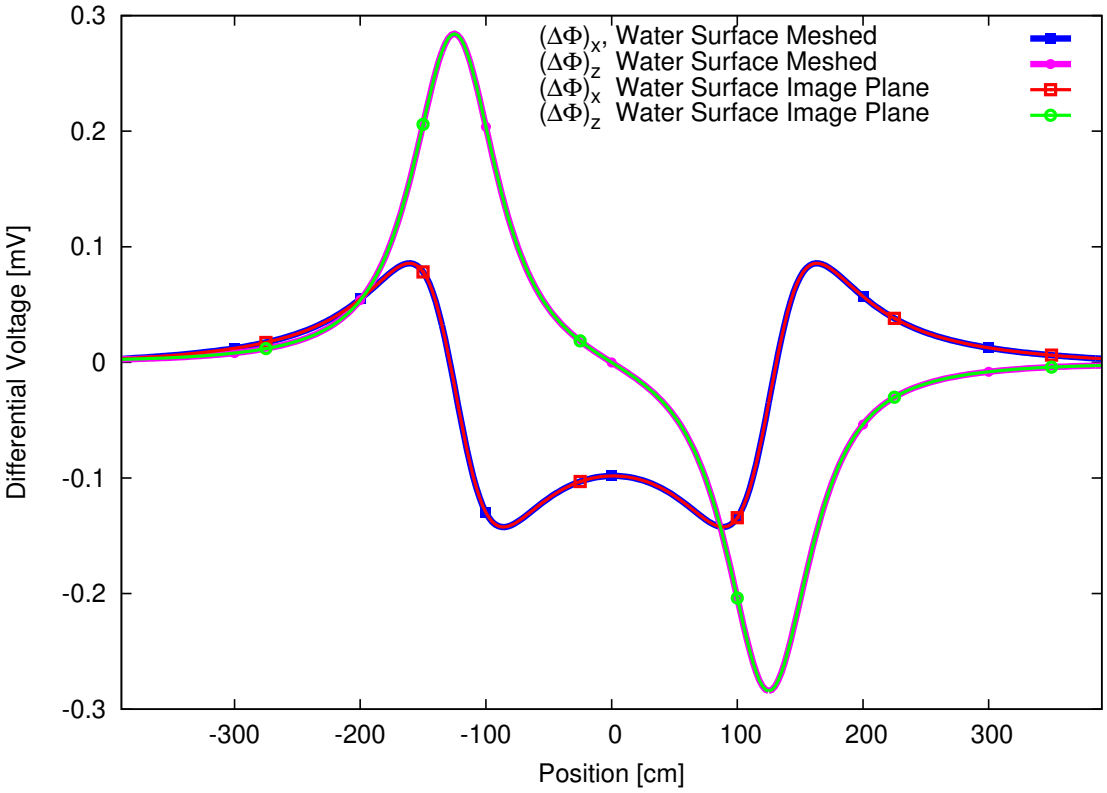

FIGURE 4.11: x- and z- directed potential differential for dipole immersed in $262.5\,\mathrm{cm}$-deep tank (cf. [78, Fig. 4]). Integration tolerance is 10^{-4}.

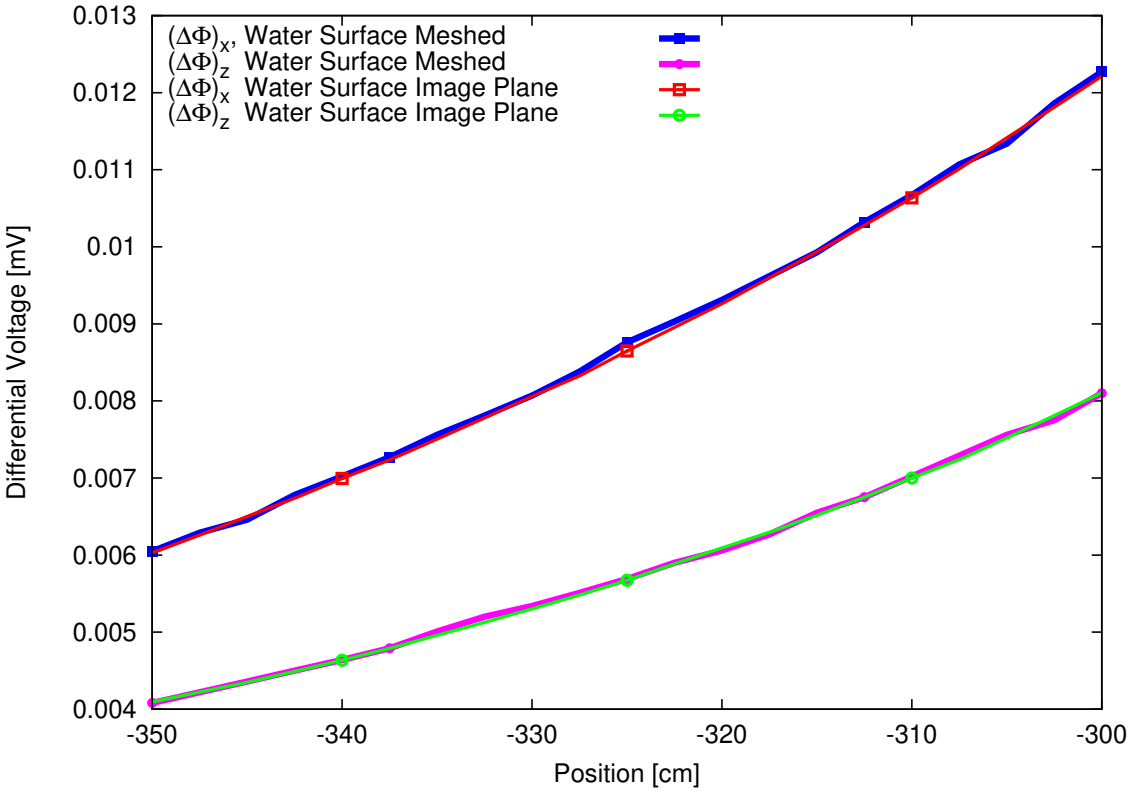

FIGURE 4.12: x- and z- directed potential differential for dipole immersed in $262.5\,\mathrm{cm}$-deep tank (cf. [78, Fig. 4]). Integration tolerance is 10^{-4}.

CHAPTER 5. Prediction of Corrosion-Related Magnetic Fields

Impressed-current corrosion protection (ICCP) systems on marine structures produce electric currents both within the structures and through the surrounding media, radiating magnetic fields referred to here as *corrosion-related magnetic* (CRM) fields. Since the currents are distributed in the surrounding electrolyte, accurate prediction of the currents and resulting fields often involves modeling of the medium itself using a technique such as the finite element method.

This section investigates the relationship between the CRM fields and the solution to the surface integral equation discussed in the previous chapter. Different strategies for calculating the CRM fields from the surface potential are investigated along with their respective advantages and limitations. Complications that arise from the presence of the water surface are addressed, and a solution is proposed and tested.

5.1 Uniqueness of CRM Field

The total field produced by the entire corrosion-protection system is not in general uniquely determined by the boundary conditions considered in Chapter 4. In the static problem with a structure surrounded by an electrolyte V, we are given the following

$$\boldsymbol{\nabla} \times \mathbf{H} = \mathbf{J},\ \mathbf{r} \in V \tag{5.1}$$

$$\boldsymbol{\nabla} \cdot \mathbf{H} = 0,\ \mathbf{r} \in V \tag{5.2}$$

where the conduction current density $\mathbf{J} = -\sigma \boldsymbol{\nabla} \Phi$ is known from the solution to the electrostatic problem. Suppose some solution $\mathbf{H}_1$ exists for this system. Now

take any field $\mathbf{H}_2$ such that $\boldsymbol{\nabla} \cdot \mathbf{H}_2 = \boldsymbol{\nabla} \times \mathbf{H}_2 = 0$. Such a field could be created by a source outside V (e.g. circuits or permanent magnets within the hull). Now the field created by superposing $\mathbf{H}_1$ and $\mathbf{H}_2$ will also be a field satisfying (5.1) and (5.2). Thus only part of the total $\mathbf{H}$-field is determined by the volume currents in V (cf. [63, 4.17]). Note that in this chapter we are concerned with calculating only those magnetic fields radiated by the ICCP currents, both those flowing through the electrolyte and those flowing within the structure.

Some commercial software allows the user to place wires within the structure that carry the necessary current between the electrodes, and from the current in these wires the resulting field can be calculated using the Biot-Savart law [60]. A similar method is presented below in which the normal current density distribution, found by solving the exterior electrostatic problem, is imposed as a Neumann boundary condition on an interior problem bounded by the same surface. In this way, an internal volume current distribution can be found that correctly sources and sinks the electrode currents, and from which an exterior field can be calculated. The result will in general differ from what would be calculated if the exact structural currents were used to calculate the fields using the Biot-Savart law, but when these exact currents are not known or modeling is inconvenient then the above method gives a good approximation.

Another method is to replace the volume and hull sources with a row of current monopoles connected by thin wires [58,60]. This "discrete source" approach allows for a rapid approximation of the CRM fields, especially at greater distances from the hull, though the placement of monopole sources for a good result is not so straightforward as the methods mentioned previously.

5.2 Calculation of CRM Fields from Surface Potential

For a vessel with surface S in a homogeneous conducting region V, the magnetic field can be computed from the surface potential with no need of volume integral methods. For the computation of the magnetic field $\mathbf{H}$ at any point in V we look first at the Helmholtz decomposition of $\mathbf{H}$ (bearing in mind that $\boldsymbol{\nabla} \cdot \mathbf{H} = 0$)

$$\begin{aligned} \mathbf{H}(\mathbf{r}) &= -\boldsymbol{\nabla}\Phi + \boldsymbol{\nabla} \times \mathbf{A} \\ &= \frac{1}{4\pi}\left[\boldsymbol{\nabla} \oint_S \frac{\hat{\mathbf{n}}' \cdot \mathbf{H}(\mathbf{r}')}{|\mathbf{r}-\mathbf{r}'|} dS' + \boldsymbol{\nabla} \times \left(\int_V \frac{\boldsymbol{\nabla}' \times \mathbf{H}(\mathbf{r}')}{|\mathbf{r}-\mathbf{r}'|} dV' - \oint_S \hat{\mathbf{n}}' \times \frac{\mathbf{H}(\mathbf{r}')}{|\mathbf{r}-\mathbf{r}'|} dS' \right) \right] \end{aligned} \tag{5.3}$$

where $\hat{\mathbf{n}}'$ signifies the normal vector pointing out of V. From this is derived the formula [63]

$$\begin{aligned} \mathbf{H}(\mathbf{r}) =& \frac{1}{4\pi} \int_V \mathbf{J}' \times \boldsymbol{\nabla}' \left(\frac{1}{|\mathbf{r}-\mathbf{r}'|} \right) dV' - \frac{1}{4\pi} \oint_S (\hat{\mathbf{n}}' \times \mathbf{H}') \times \boldsymbol{\nabla}' \left(\frac{1}{|\mathbf{r}-\mathbf{r}'|} \right) dS' \\ & - \frac{1}{4\pi} \oint_S (\hat{\mathbf{n}}' \cdot \mathbf{H}') \, \boldsymbol{\nabla}' \left(\frac{1}{|\mathbf{r}-\mathbf{r}'|} \right) dS'. \end{aligned} \tag{5.4}$$

As pointed out in [63], the surface integral terms account for sources outside V, in this case sources within the hull. This portion of the magnetic field is referred to here as the *structural current* magnetic field $\mathbf{H}^{struct}$. The remaining volume integral in (5.4) gives the *volume current* magnetic field $\mathbf{H}^{vol}$ due to the volume current density $\mathbf{J}$ in V. The total field is then given by $\mathbf{H} = \mathbf{H}^{vol} + \mathbf{H}^{struct}$. The volume integral expression for $\mathbf{H}^{vol}$ can be reduced to a surface integral, as in [59] when V is homogeneous:

$$\mathbf{H}^{vol}(\mathbf{r}) = -\frac{\sigma}{4\pi} \oint_S \Phi(\mathbf{r}') \frac{\hat{\mathbf{n}}' \times (\mathbf{r}-\mathbf{r}')}{|\mathbf{r}-\mathbf{r}'|^3} dS'. \tag{5.5}$$

where $\hat{\mathbf{n}}'$ points out of V into the hull. This is the primary method used in this paper to calculate the magnetic field due to volume currents in V.

5.2.1 Calculation of Structural Current Field

Accurate calculation of the near-field structural magnetic field requires explicit knowledge and modeling of the corrosion current flow within the vessel. This may be very complex to determine, depending on hull shape and composition and on the configuration of the ICCP system. An approximation of the structural magnetic field may be obtained, however, by solving the exterior problem, if necessary, to find the normal current density on all electrodes. Once this is known, the opposite normal current density may be imposed as a Neumann boundary condition on the interior problem with the same geometry. The resulting interior surface potential can then be used to calculate the structural magnetic field via (5.5).

The process can be outlined as follows. First, solve (4.17) for the normal flux density Ψ on the surface of the structure:

$$\begin{bmatrix} [H_{ext}] & -[1] \\ [0] & 0 \end{bmatrix} \begin{bmatrix} \bar{\Phi}_{ext} \\ \Phi_{\infty} \end{bmatrix} = \begin{bmatrix} [G_{ext}] \\ [S] \end{bmatrix} \bar{\Psi}_{ext}. \tag{5.6}$$

Next, solve the interior Neumann problem:

$$[H_{int}]\bar{\Phi}_{int} = [G_{int}](-\bar{\Psi}_{ext}). \tag{5.7}$$

Then the structural field $\mathbf{H}^{struct}$ is calculated as

$$\mathbf{H}^{struct}(\mathbf{r}) = -\frac{\sigma}{4\pi} \oint_S \Phi_{int}(\mathbf{r}') \frac{\hat{\mathbf{n}}' \times (\mathbf{r} - \mathbf{r}')}{|\mathbf{r} - \mathbf{r}'|^3} dS' \tag{5.8}$$

where $\hat{\mathbf{n}}'$ points out of the hull into the electrolyte.

5.2.2 Problems in a Semi-Infinite Electrolyte

Although the boundary conditions on the electrostatic problem at the electrolyte boundary allow for the use of image methods when a vessel is at or near the water surface, the lack of any similar boundary conditions on the corrosion-related magnetic fields necessitates some other method for calculating $\mathbf{H}^{vol}$. As shown in [60], one approach is to mesh the water surface to some distance from the ship, and add walls and a bottom enclosing the volume of electrolyte containing the majority of the corrosion currents. The current flow in a finite box, however, differs from the current distribution that would result in a semi-infinite medium, and so the magnetic field computed by artificially bounding the electrolyte with a large box will differ from the desired solution. This can be remedied to some degree by extending the boundaries of the box far from the ship; the result does converge toward the correct solution as the boundaries are extended, but naturally this significantly increases the number of unknowns in the problem.

We present an alternative approach here that uses the image method solution to the electrostatic problem. From this solution we can calculate the potential at any point on the water surface, and from the potential thus computed we can calculate the magnetic field using (5.5) where the water surface is included in S.

If we let the electrolyte be bounded below the water surface by a hemisphere of radius a, we see that the integrand in (5.5) on this hemispherical surface tends to zero as $a \to \infty$. Let the hull be contained within the sphere $r \leq b$. Now taking $\mathbf{r}$ such that $|\mathbf{r}| = a$, $\hat{\mathbf{n}} \times (\mathbf{r} - \mathbf{r}')$ can be shown to have a magnitude not greater than $\frac{b}{a}|\mathbf{r} - \mathbf{r}'|$. And so for large a the maximum magnitude of $\frac{\hat{\mathbf{n}} \times (\mathbf{r} - \mathbf{r}')}{|\mathbf{r} - \mathbf{r}'|^3}$ is approximately $\frac{b}{a^3}$, and as this falls off faster than $1/a^2$, the portion of the integral in (5.5) over the hemisphere tends to zero as $a \to \infty$. The volume current field can then be

calculated as

$$\mathbf{H}^{vol}(\mathbf{r}) = -\frac{\sigma}{4\pi}\left(\int\limits_{S_{hull}} \Phi(\mathbf{r}')\frac{\hat{\mathbf{n}}' \times (\mathbf{r}-\mathbf{r}')}{|\mathbf{r}-\mathbf{r}'|^3}dS' + \int\limits_{S_{water}} \Phi(\mathbf{r}')\frac{\hat{\mathbf{n}}' \times (\mathbf{r}-\mathbf{r}')}{|\mathbf{r}-\mathbf{r}'|^3}dS'\right) \tag{5.9}$$

where S_{hull} is the submerged surface of the structure, S_{water} is the surface of the electrolyte, and Φ is calculated from the electrostatic problem with an image-plane Green's function. Once Φ and $\partial\Phi/\partial n$ are found on S_{hull} using an image method, the integral over S_{water} is computed as

$$-\frac{\sigma}{4\pi}\int\limits_{S_{water}} \frac{\hat{\mathbf{n}}' \times (\mathbf{r}-\mathbf{r}')}{|\mathbf{r}-\mathbf{r}'|^3}\left[\int\limits_{S_{hull}}\left(-\Phi''\frac{\partial G^{im}}{\partial n''} + \frac{\partial \Phi''}{\partial n''}G^{im}(\mathbf{r}',\mathbf{r}'')\right)dS''\right]dS' \tag{5.10}$$

where $\Phi'' = \Phi(\mathbf{r}'')$ and G^{im} is the PMC image-plane Green's function used to solve the electrostatic problem. In practice, this method naturally requires truncation of the water surface integration. It is shown below that truncation at several ship lengths away gives good results.

Note that the term Φ_∞ can be omitted in calculating Φ, since the integrand in (5.5) is zero for a constant Φ. Moreover, if the integral is only computed over the hull and the water surface, then Φ_∞ must be omitted to obtain an accurate result.

One possible strategy for approximating the field due to the integral over the water surface beyond the truncation is to use a multipole expansion [74], noting that the normal flux density on the hull surface is mathematically equivalent to a surface charge density (cf. [74]). The monopole moment of the hull is zero since the net surface charge is zero. The potential due to the dipole moment decays as $1/r^2$. The potential due to quadrupole and higher-order terms drops off faster than $1/r^2$, and numerical tests in Section 5.5.3 also suggest that the effect of the quadrupole moment on the near magnetic field decreases quickly as a increases. We will therefore focus on the dipole moment. Let $\mathbf{p}$ be the dipole moment of the

structure calculated as

$$\mathbf{p} = \int_S -\frac{\partial \Phi}{\partial n'} \mathbf{r}' dS'. \tag{5.11}$$

The static potential at $\mathbf{r}$ due to a dipole centered at $\mathbf{r}'$ can be calculated as

$$\Phi(\mathbf{r}) = \frac{\mathbf{p} \cdot (\mathbf{r} - \mathbf{r}')}{4\pi |\mathbf{r} - \mathbf{r}'|^3}. \tag{5.12}$$

Let the structure be located at $\mathbf{r}_s = z_s \hat{\mathbf{z}}$. Take a point $\mathbf{r}_f$, where the horizontal distance between $\mathbf{r}_f$ and $\mathbf{r}_s$ is not great (i.e. $\mathbf{r}_f$ is approximately above or below the ship). Let the xy plane be the water surface with the electrolyte occupying the $z > 0$ region ($\hat{\mathbf{n}} = -\hat{\mathbf{z}}$). The magnetic field at $\mathbf{r}_f$ due to the integral over the water surface beyond $\rho = a$ can be approximated as:

$$\mathbf{H}_{dipole} = -2\frac{\sigma}{4\pi} \int\limits_{S_{water}, \rho > a} \frac{\mathbf{p} \cdot (\mathbf{r} - \mathbf{r}_s)}{|\mathbf{r} - \mathbf{r}_s|^3} \cdot \frac{-\hat{\mathbf{z}} \times (\mathbf{r}_f - \mathbf{r})}{4\pi |\mathbf{r} - \mathbf{r}_f|^3} dS. \tag{5.13}$$

The factor of 2 is present to account for the identical image dipole at $-z_s \hat{\mathbf{z}}$. At a point at a depth z_f, directly above or below a vessel at depth $z_s \neq z_f$, this becomes

$$\mathbf{H}_{dipole}(z_f) = \frac{\sigma}{8\pi} \cdot \frac{\hat{\mathbf{n}} \times \mathbf{p}}{(z_s^2 - z_f^2)^2} \left((z_s^2 + z_f^2) - \frac{2z_s^2 z_f^2 + a^2(z_s^2 + z_f^2)}{\sqrt{a^2 + z_s^2}\sqrt{a^2 + z_f^2}} \right). \tag{5.14}$$

In the case that $z_f = z_s$, (5.13) simplifies to

$$\mathbf{H}_{dipole}(z_s) = \frac{\sigma}{8\pi} \left(\frac{2a^2 + z_s^2}{4(a^2 + z_s^2)^2} \right) \hat{\mathbf{n}} \times \mathbf{p}. \tag{5.15}$$

For a ship at the surface ($z_s \approx 0$) the field at depth $z_f > 0$ computed by (5.14) reduces to

$$\mathbf{H}_{dipole}(z_f) = \frac{\sigma}{8\pi} \cdot \frac{\hat{\mathbf{n}} \times \mathbf{p}}{z_f^2} \left(1 - \frac{a}{\sqrt{a^2 + z_f^2}} \right). \tag{5.16}$$

One could easily add the value $\mathbf{H}_{dipole}$ calculated with the appropriate equation

above to correct the truncated integral at field points approximately above or below the ship. On the other hand, once the water surface mesh is large enough to give a good prediction of the overall shape of $\mathbf{H}(\mathbf{r})$ near the hull, the offset $\mathbf{H}_{dipole}$ is quite small, as shown in Section 5.5.3.

5.3 Approximation of CRM Fields Using Discrete Sources

Integration over the hull surface can be avoided by replacing the structure with a row of current monopoles. This *discrete source* approach, discussed in [58,60], gives reasonable accuracy in medium- and far-field calculations of magnetic fields. In this section is outlined a simple technique for calculating the monopole strengths for a given set of discrete sources to approximate the magnetic field. The method is later illustrated in a symmetric problem and compared with an analytic solution.

A current monopole here is considered as a point from which current flows uniformly in all directions. Thus a monopole at the origin emitting a current I would result in a current density

$$\mathbf{J}(r) = \frac{I}{(4\pi r^2)}\hat{\mathbf{r}}. \tag{5.17}$$

Since $\mathbf{E} = \mathbf{J}/\sigma$, the static electric potential Φ at a distance R from the current monopole is then given by (cf. [79])

$$\Phi = \frac{I}{4\pi\sigma R}. \tag{5.18}$$

In [80], the loss of charge from a current monopole is remedied by connecting a semi-infinite wire to the monopole to supply current. This wire creates its own magnetic field. For the problem to be physically realistic, the total current entering and exiting monopoles must be zero, and so for a monopole of strength I there

must be another monopole or monopoles of collective strength $-I$. In the case of two monopoles, supplied with currents I and $-I$, the wires supplying them can be placed in such a way that the portions going off to infinity coincide, so that only the segment of wire connecting the two sources radiates a net magnetic field. In effect, the monopoles can be thought of as sources and sinks where the current is brought to or from each by a series of wires connecting them.

From the wires connecting the monopoles the magnetic field at a point $\mathbf{r}$ can be calculated using the Biot-Savart Law. With a proper choice of arrangement and shape of these connecting wires, the magnetic field so calculated can give a good approximation of the CRM fields in the medium and far field.

5.3.1 Calculation of Monopole Strengths

Once the number N_m and locations $\{\mathbf{r}_i^m\},\ i = 1 \dots N_m$ of monopole sources have been chosen, the electric potential Φ is calculated at N_p points $\{r_j\}$ in V. This can be done using the boundary element method described in Chapter 4. Applying (5.18) to each monopole, we can express the potential Φ^{DS} at a given point $\mathbf{r}$ due to the discrete sources as

$$\Phi^{DS}(\mathbf{r}) = \sum_{i=1}^{N_m} \frac{I_i}{4\pi\sigma|\mathbf{r} - \mathbf{r}_i^m|} \tag{5.19}$$

Ideally, we want $\Phi^{DS} = \Phi^{SIE}$ where Φ^{SIE} is the potential computed in the electrostatic problem. Moreover, the net current out of and into the monopoles must be zero. This gives us a system of $N_p + 1$ equations in N_m unknowns:

$$\sum_{i=1}^{N_m} \frac{I_i}{4\pi\sigma|\mathbf{r}_j - \mathbf{r}_i^m|} = \Phi^{SIE}(\mathbf{r}_j),\ j = 1, 2, \dots N_p \tag{5.20}$$

$$\sum_{i=1}^{N_m} I_i = 0. \tag{5.21}$$

Numerical test results shown below in Section 5.5.1 indicate that a convenient method of approximating $\mathbf{H}$ is to solve (5.20) and then project the solution vector $\bar{I}$ onto the subspace of monopole strengths that sum to zero. This subspace is just the null space of the $1 \times N_m$ matrix $[\bar{1}]$ whose entries are all 1. If we let $[A]$ denote the unitary $N_m \times (N_m - 1)$ matrix whose columns span $\ker([\bar{1}])$, then the projection $\bar{I}'$ onto the null space is computed as

$$\bar{I}' = [A][A]^T \bar{I} \tag{5.22}$$

5.3.2 Magnetic Field Computation

Once the monopole strengths I_i are calculated, the magnetic field $\mathbf{H}$ can be computed for arbitrary points in space using the Biot-Savart law:

$$\mathbf{B}(\mathbf{r}) = \frac{\mu}{4\pi} \int_C \frac{I(\mathbf{r}')d\mathbf{r}' \times (\mathbf{r} - \mathbf{r}')}{|\mathbf{r} - \mathbf{r}'|^3} \tag{5.23}$$

where C is a wire connecting the monopoles. When the wire is in straight segments, $\mathbf{B}$ can be computed exactly. If the current I in a straight wire runs from $\mathbf{r}_1$ to $\mathbf{r}_2$, the field at $\mathbf{r}$ is found by a simple formula. Let $\hat{\mathbf{u}}$ be the unit vector pointing from $\mathbf{r}_1$ to $\mathbf{r}_2$. And let $u_1 = (\mathbf{r} - \mathbf{r}_1) \cdot \hat{\mathbf{u}}$ and $u_2 = (\mathbf{r} - \mathbf{r}_2) \cdot \hat{\mathbf{u}}$. Finally, let $v = |\hat{\mathbf{u}} \times (\mathbf{r} - \mathbf{r}_1)|$ and let $\hat{\boldsymbol{\varphi}}' = v^{-1}\hat{\mathbf{u}} \times (\mathbf{r} - \mathbf{r}_1)$. The Biot-Savart law then reduces to (cf. [80]):

$$\mathbf{B}(\mathbf{r}) = \frac{\mu I}{4\pi v} \hat{\boldsymbol{\varphi}}' \left(\frac{u'}{\sqrt{v^2 + u'^2}} \Bigg|_{u'=u1}^{u'=u2} \right) \tag{5.24}$$

For a wire joining several monopoles (numbered beginning at the endpoint), the current I_n on the segment C_n between the nth and $n+1$th monopoles is given by

$$I_n = \sum_{i=0}^{n} I_i^m \tag{5.25}$$

where I_i^m denotes the monopole strength.

5.4 Comparison of Methods

In this paper three different methods have been referred to for calculating the magnetic field radiated by the structural currents in an ICCP system. Discrete current monopoles can be used to approximate the total field due to both the volume currents and the structural currents at once. This is referred to as the *discrete source method*. Alternatively, if the configuration of the current-carrying wires in the ICCP system is known, at least approximately, the structural current field can be calculated using the Biot-Savart law. This method is mentioned in [60], and is referred to below as the *wire method*. The third method is that presented in Section 5.2.1 of this paper, where the structural currents within the vessel are approximated by solving an interior problem with Neumann boundary conditions equal and opposite to those found by solving the exterior problem. This method is referred to in this section as the *interior surface integral equation (SIE) method*.

A few observations can be made about these different methods. Evidently, the *discrete source* method greatly simplifies the problem, and is intended for medium- and far-field analysis [58]. When the anodic and cathodic regions are small, the *wire method* will likely give a result quite close to the reality, provided that the wires are connected to the hull at or near the electrodes, since in this case very little current will flow through the hull far from the electrodes. In situations such as that depicted in Fig. 5.1, however, where the exposed surface is at some distance from the connection of the ICCP system to the hull, the current flow through the hull (C to B in the figure) is neglected. This will in general have some effect on accuracy, even if the interior wiring of the protection system (B to A in the figure) is modeled accurately. Likewise, the *interior SIE method*, which allows the interior current to flow through the entire vessel as though through a homogeneous conductor, will

not precisely match the actual ICCP current flow, which will in reality be confined to certain conducting regions within the hull.

Table 5.1 summarizes certain advantages and limitations of the three methods. The superiority of one method or another will naturally depend on the particular problem, and further work is required to determine the circumstances that recommend each approach.

5.5 Numerical Test Results

In this section the accuracy of the surface-integral and discrete-source methods for computing the magnetic field are verified by comparison to the problem in Section 4.6.1. The magnetic field is then calculated for the problem in Section 4.6.4, where different methods and hull configurations are used to show the difference in the magnetic field prediction. Finally, the volume-current magnetic field is calculated for a structure at or near the electrolyte boundary, showing the efficacy of the method proposed in Section 5.2.2 using a mesh of the water surface with an image-method solution of the electrostatic problem.

5.5.1 Benchmark Problem

The benchmark problem presented in [73] admits an analytic solution for the magnetic field. The symmetry of the problem makes placement of current monopoles relatively easy, and so we present results computed with both the surface integral and discrete source methods.

From the analytic solution for the surface potential Φ given in [73]

$$\Phi(r,\theta) = -\left(3 + \frac{1}{3r^2}\cos\theta\right) \tag{5.26}$$

we can compute the current density at an arbitrary point in space:

$$\mathbf{J}(r,\theta) = -\sigma\boldsymbol{\nabla}\Phi = -\frac{\sigma}{3}\left(2\frac{\cos\theta}{r^3}\hat{\mathbf{r}} + \frac{\sin\theta}{r^3}\hat{\boldsymbol{\theta}}\right). \tag{5.27}$$

It is found that $\mathbf{J} = \boldsymbol{\nabla} \times \mathbf{H}$ is satisfied by

$$\mathbf{H}(r,\theta) = \left(-\frac{\sigma\sin\theta}{3r^2}\right)\hat{\boldsymbol{\varphi}}. \tag{5.28}$$

The problem is solved numerically using surface meshes consisting of 96, 384 and 864 10th order quadrilateral cells. The relative RMS error for the results calculated with the proposed method is shown in Fig. 5.2. The $\mathbf{H}$ field is calculated at 102 field points evenly spaced at a distance of $1.5\,\mathrm{m}$ from the center of the sphere, as in Section 3.4.2.1.

The behavior of the discrete source solution for the same problem is shown in Fig. 5.3. The magnetic field intensity $\mathbf{H}$ is calculated at different distances r from the sphere center and at different polar angles θ. By some trial and error, it is found that placing two monopoles at $z = \pm 14\,\mathrm{cm}$ gives a good result. The number and location of the points $\mathbf{r}_j$ in (5.20) are chosen in two ways. First, we take 2 points at $(x, y, z) = (2\,\mathrm{m}, 0, \pm 2\,\mathrm{m})$. Solving (5.20) and enforcing neutrality as in Section 5.3.1 gives us monopole strengths of $\pm 14.969\,\mathrm{A}$. If we instead take the points $\mathbf{r}_j$ to be the centers of the 384 cells, the monopole strengths are then found to be $\pm 14.971\,\mathrm{A}$. The latter approach is found to give slightly better accuracy, though both methods stagnate at about $0.1\,\%$ error as r grows. Relative error in Fig. 5.3 is computed as

$$\left|\frac{H_\varphi^{analytic} - H_\varphi^{DS}}{H_\varphi^{analytic}}\right|$$

The surface integral results for the same field points are also plotted for comparison in Fig. 5.3. Interestingly, the discrete source method gives better accuracy for

points on the surface of the sphere, though it is quickly overtaken by the surface integral result when the field point is off the surface.

5.5.2 Semi-Cylindrical Hull at Water Surface

The semi-cylindrical hull problem described in [60] allows us to compare CRM fields to published results for a less symmetric test case. The details of the problem have already been described in Section 4.6.4.

Figure 5.5 shows the y-directed magnetic flux density $\mathbf{B} = \mu_0 \mathbf{H}$ resulting from the volume currents and from the structural currents flowing within the hull. The structural current fields are computed using the *interior SIE method* described in Sections 5.2.1 and 5.4. The plots agree well with those presented for the same problem in [60], where fields due to structural currents are accounted for by specially placed wires or discrete sources. The volume current fields are calculated using the surface integral computation (5.5) with the electrolyte bounded by a box extending $500\,\mathrm{m}$ in the $\pm x$ and $\pm y$ directions, and $1000\,\mathrm{m}$ below the surface.

Figures 5.6 and 5.7 compare the predicted $\mathbf{H}^{vol}$ where the medium is bounded at different distances using the approach in [60] to the result using the image method proposed in Section 5.2.2 with the water surface terminated at different distances a from the point on the water surface directly above the center of the hull. In the former method, the electrolyte is bounded at the water surface $z = 0$, at a depth $z = d$, and horizontally at $x = d$, $x = -d$, $y = d$, $y = -d$ where d has a value of $200\,\mathrm{m}$, $500\,\mathrm{m}$, or $1000\,\mathrm{m}$. In the latter method, the image method is used to solve the electrostatic problem using the mesh shown in Fig. 5.4a. The resulting solution is used to compute the potential at quadrature points for a $p = 2$ fixed-point quadrature over the mesh of the water surface shown in Fig. 5.4b, which is truncated at a radius a with a value of $100\,\mathrm{m}$, $200\,\mathrm{m}$, $300\,\mathrm{m}$, or $400\,\mathrm{m}$. It is found that while both methods converge toward the $\approx -50\,\mathrm{nT}$ value below the hull found

in [60], the image method has a consistent time requirement of about 10 minutes, while the alternate method requires a solution time ranging from 41 minutes to 114 minutes, for the calculations shown in Figs. 5.6 and 5.7.

The *interior SIE method* for calculating the structural currents is tested for a few different hull configurations. Problems where the current is allowed to flow above the water line, either through a half-cylinder mirroring the submerged portion (see Fig. 5.8a) or through a $1\,\mathrm{m}$-high box formed by extruding the top hull boundary in the z direction (see Fig. 5.8b), are compared to problems where the submerged portion alone is meshed with a solid hull, a semi-cylindrical shell with $0.5\,\mathrm{m}$-thick conductive walls (Fig. 5.8c), and a semi-cylindrical shell with $0.25\,\mathrm{m}$-thick conductive walls (Fig. 5.8d). In the "semi-cylindrical shell" cases, all surfaces are still insulated except the outermost ends of the hull, which source and sink $20\,\mathrm{A}$ as before, and the structural current flow is confined to a homogeneous $0.25\,\mathrm{m}$- or $0.5\,\mathrm{m}$-thick shell.

The y-directed structural $\mathbf{B}$-fields near the hull differ somewhat for the different configurations tested, as is shown in Fig. 5.9 on a line between $x = \pm 40\,\mathrm{m}$ at a depth of $20\,\mathrm{m}$ directly below the hull axis. For reference, the field due to $20\,\mathrm{A}$ flowing in a thin wire along the hull axis is computed using the Biot-Savart law and plotted in Fig. 5.9.

When the electrolyte is truncated and an interior problem is solved for the volume currents, the *interior SIE method* (which in this case actually solves an *exterior* Neumann problem to find the structural currents) does not in general give a good result. This is because the structural currents, not confined to the hull but free to take any path above the water surface, will be distributed much farther from the ship than in reality, resulting in a substantially different field prediction.

5.5.3 Rectangular Box Problem

In this section the $20\,\mathrm{m} \times 10\,\mathrm{m} \times 1\,\mathrm{m}$ box described in Section 4.6.2 is used to verify the method presented in Section 5.2.2 for approximating the magnetic field radiated by ICCP volume currents at or near the boundary of a semi-infinite electrolyte. The box has four $1\,\mathrm{m} \times 1\,\mathrm{m}$ electrodes placed at the corners, each parallel to the y-z plane. The box is placed at a depth of $d \geq 0$, its boundaries defined by $|x| \leq 10\,\mathrm{m}$, $|y| \leq 5\,\mathrm{m}$, $d \leq z \leq d + 1\,\mathrm{m}$, in a semi-infinite electrolyte of conductivity $4\,\mathrm{S\,m^{-1}}$ bounded by the plane $z = 0$. The four corner electrodes are numbered 1-4 as diagrammed in Fig. 4.2.

In the following tests, the result computed by the method presented in Section 5.2.2 is compared with the solution obtained when the electrolyte is bounded at $x = \pm 1000\,\mathrm{m}$, $y = \pm 1000\,\mathrm{m}$, $z = 1000\,\mathrm{m}$. The depth d takes values $0\,\mathrm{m}$, $2\,\mathrm{m}$, and $20\,\mathrm{m}$. The field is calculated at a row of points from $(-100\,\mathrm{m}, 0\,\mathrm{m}, d + 20\,\mathrm{m})$ to $(100\,\mathrm{m}, 0\,\mathrm{m}, d + 20\,\mathrm{m})$. The integration over the water surface using the image method as in Section 5.2.2 is truncated at a radius $a = 30, 50, 100, 200\,\mathrm{m}$.

In Fig. 5.10, a uniform $20\,\mathrm{A\,m^{-2}}$ current density is present on electrodes 1 and 4, balanced by $-20\,\mathrm{A\,m^{-2}}$ on electrodes 2 and 3. Figures 5.11 and 5.12, respectively, show the x- and z-directed fields when the electrodes are assigned current densities $\{20\,\mathrm{A\,m^{-2}}, -20\,\mathrm{A\,m^{-2}}, 20\,\mathrm{A\,m^{-2}}, -20\,\mathrm{A\,m^{-2}}\}$, which gives the problem a zero dipole moment. In both cases, the $\mathbf{H}$ computed from the image method Φ converges toward the bounded electrolyte solution as a increases. We see in Fig. 5.11 that the case with no dipole moment does not show the offset present in Fig. 5.10, which makes sense given the rapid decay of fields due to a quadrupole moment mentioned in Section 5.2.2.

Figures 5.13, 5.14, and 5.15 show the field components for a configuration with electrode currents $\{20\,\mathrm{A\,m^{-2}}, -10\,\mathrm{A\,m^{-2}}, -20\,\mathrm{A\,m^{-2}}, 10\,\mathrm{A\,m^{-2}}\}$. As above, the fields converge toward the result computed with the bounded electrolyte as a increases,

giving very close agreement when the surface integration is terminated at about 10 ship lengths from the origin. Note that the z-directed fields plotted in Figs. 5.12 and 5.15 do not depend on the value of a used. This is because the normal to the water surface is in the $\hat{\mathbf{z}}$ direction, which implies that the integration of $\Phi\hat{\mathbf{n}}' \times \boldsymbol{\nabla}' G$ over S_{water} in (5.9) will not have a z component.

5.6 Summary

The corrosion-related magnetic fields radiated by an impressed current cathodic protection system can be calculated by various methods. In this chapter the high-order Nyström solution to the electrostatic problem in Chapter 4 is used to compute the magnetic field due to the corrosion currents through the electrolyte surrounding a submerged structure. A technique for approximating the magnetic field due to currents flowing within the structure is also presented and found to compare well with other methods and with an analytic solution for a benchmark problem. In addition, a method for efficiently calculating the magnetic field in a semi-infinite electrolyte is shown to give accurate results and a significant reduction in solution time.

TABLE 5.1: Comparison of Structural **H** Computation Methods

Method	Advantages	Disadvantages
Wire	• Simple and accurate Biot-Savart law calculation • Can accurately model internal wire configuration	• Requires some knowledge of interior • User must manually specify configuration • May neglect portions of hull current
Discrete Source	• Does not require complete SIE solution • Approximates entire field • Rapid calculation for each probe point	• Less accurate in near-field • Sensitive to monopole placement
Interior SIE	• Automatic current continuity with exterior problem • Does not rely on user for wire placement	• Requires second solution of system • Structural current flow does not closely match reality in general

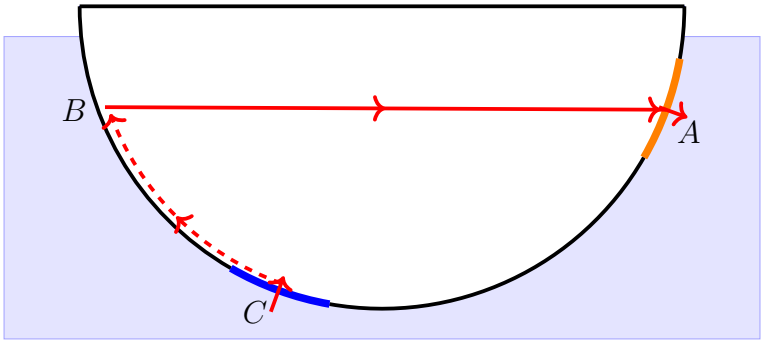

FIGURE 5.1: Current flow in cathodic protection system connected to anode at A, connected to hull at B, with exposed cathodic surface at C.

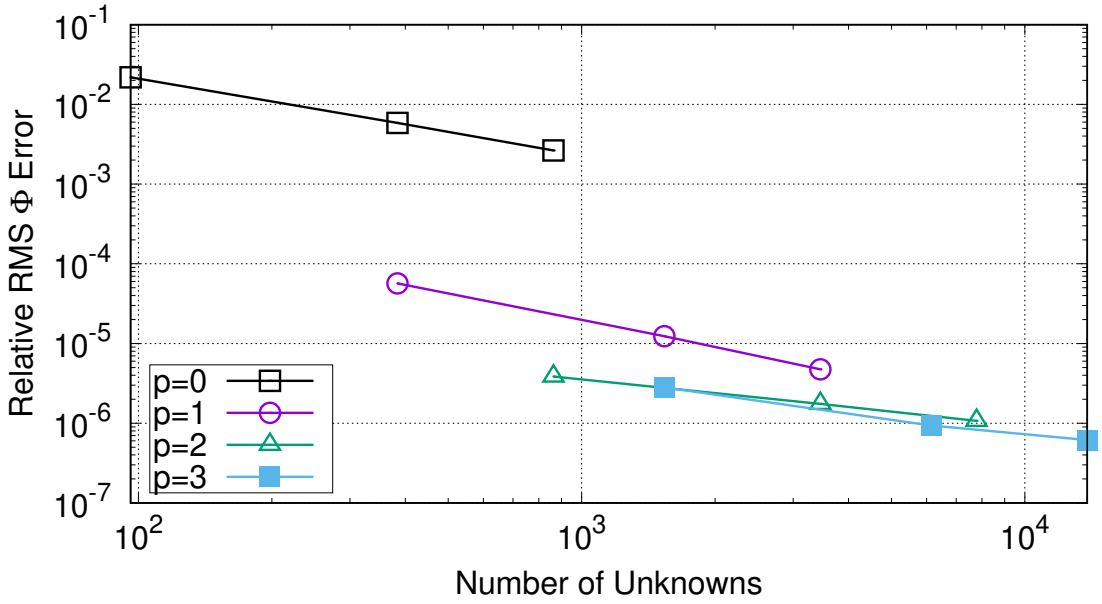

FIGURE 5.2: Relative RMS error of CRM fields for benchmark problem in [73] meshed with 96, 384 and 864 10th order quadrilateral cells. Integration tolerance is 10^{-6}.

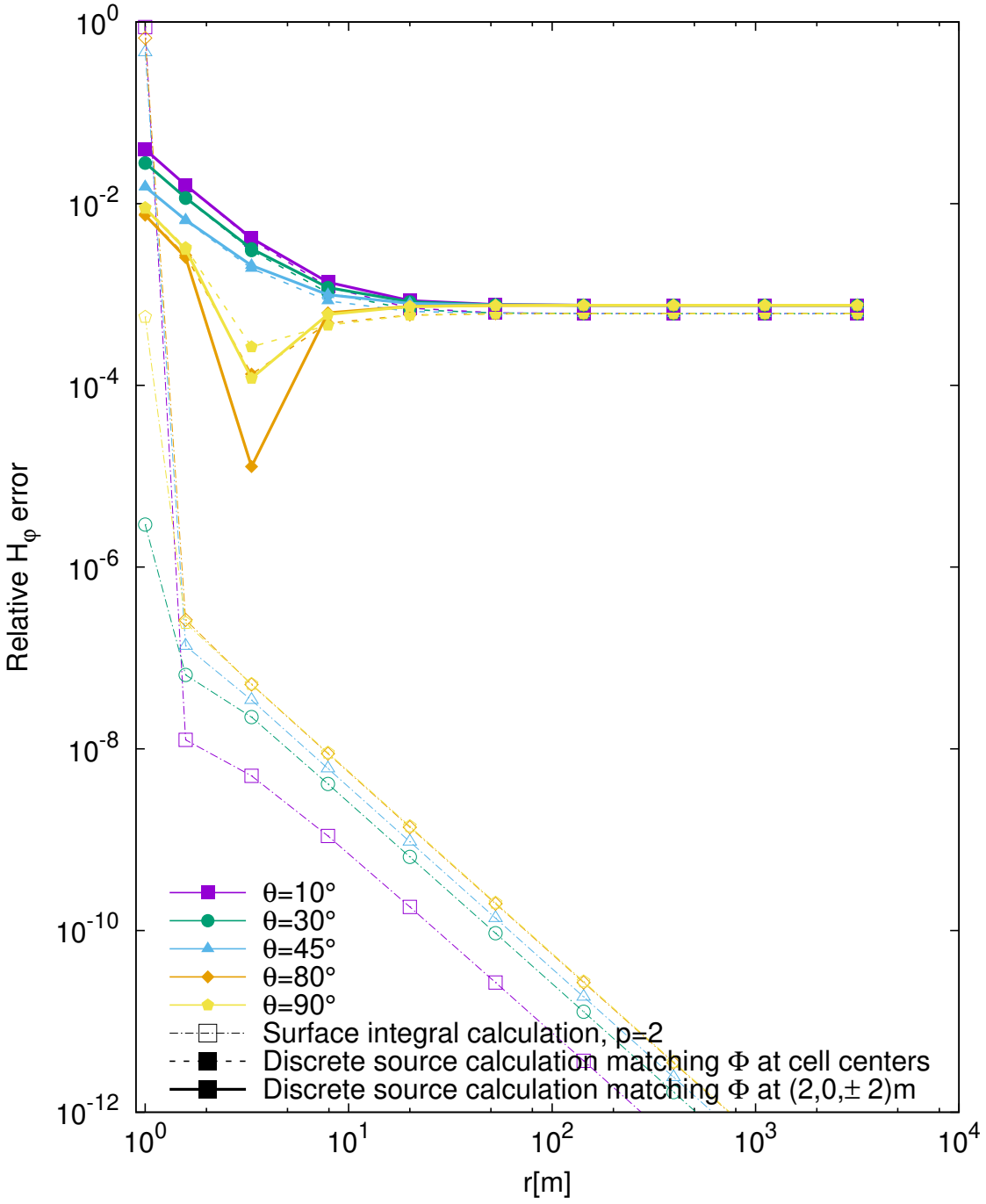

FIGURE 5.3: Relative H_φ error $\left|\frac{H_\varphi^{Computed}-H_\varphi^{Analytic}}{H_\varphi^{Analytic}}\right|$ for sphere benchmark problem using discrete source method with monopoles at $z = \pm 14\,\mathrm{cm}$ and using surface integral calculation. Sphere discretized with 384 10th order quadrilateral cells.

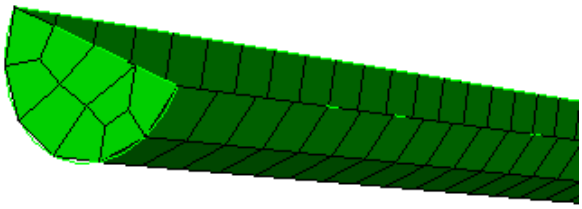

(a) Hull Mesh

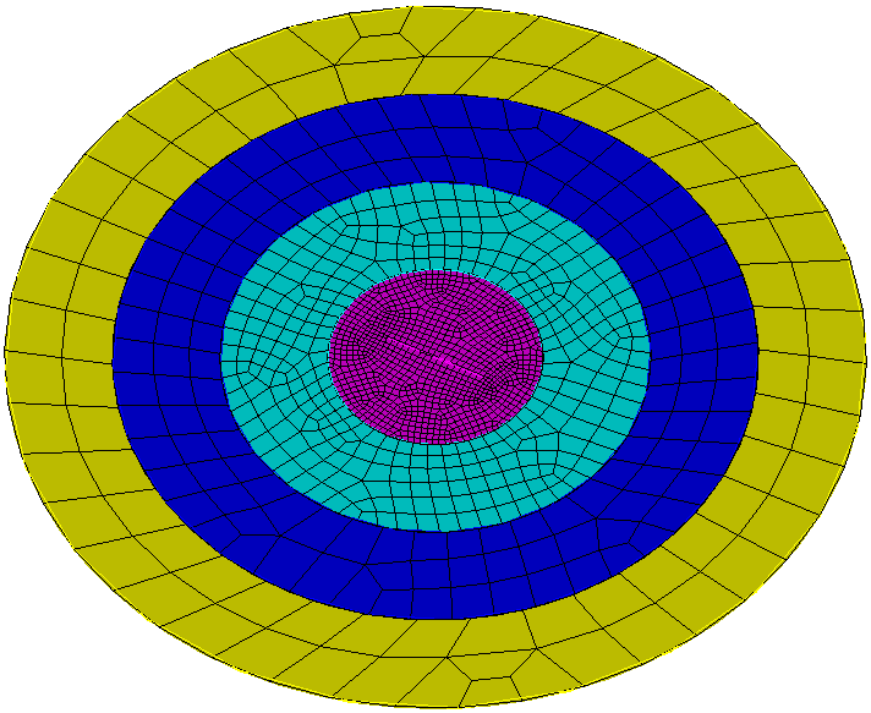

(b) Water Surface Mesh

FIGURE 5.4: Meshes used for CRM calculation with image method.

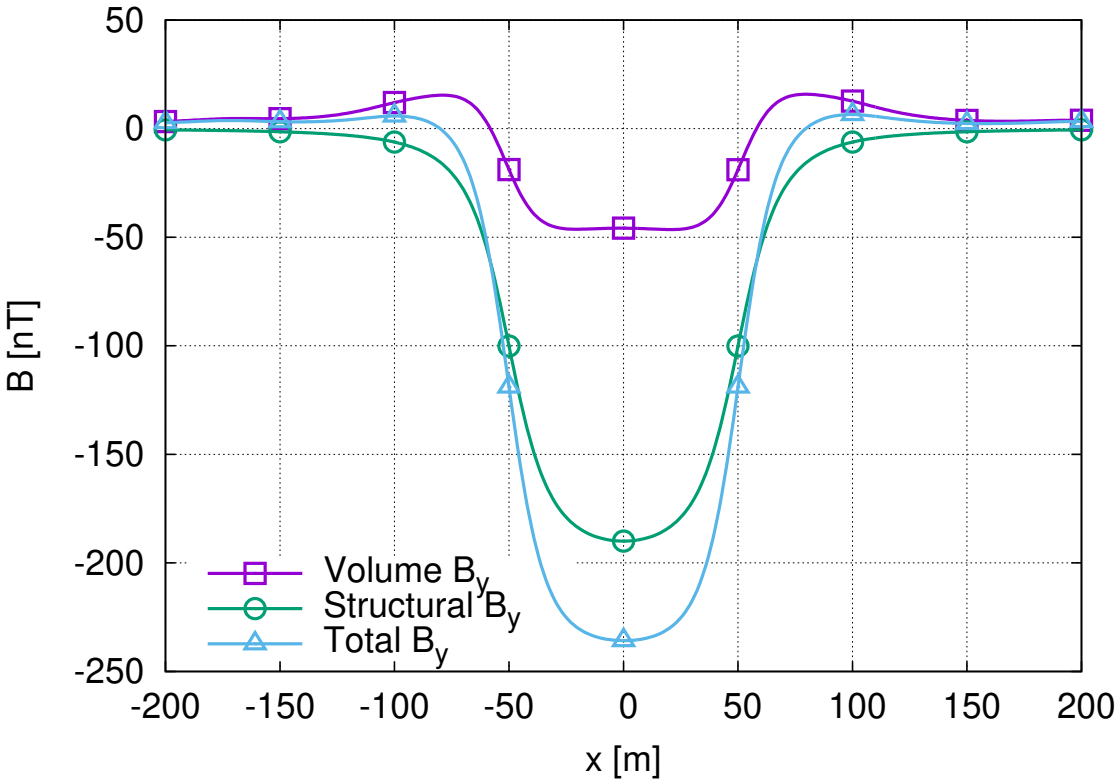

FIGURE 5.5: y-directed **B**-field at a depth of $20\,\mathrm{m}$ below x-axis for CRM semi-cylindrical hull problem (cf. [60, Fig. 10]). Integration tolerance is 10^{-6}.

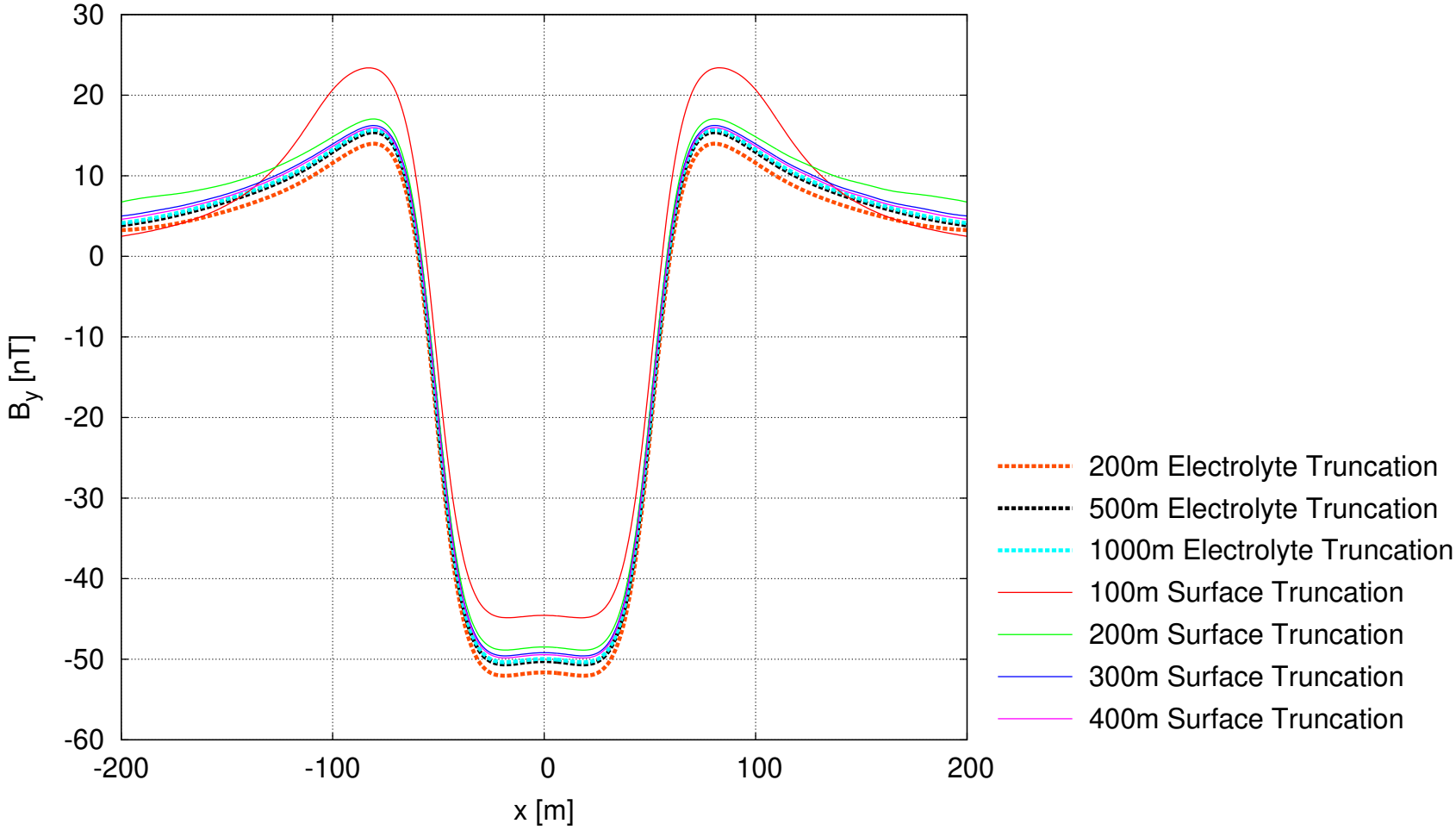

FIGURE 5.6: y-directed **B**-field at a depth of $20\,\mathrm{m}$ below x-axis for CRM semi-cylindrical hull problem. Comparison of methods and discretizations. Integration tolerance is 10^{-6}.

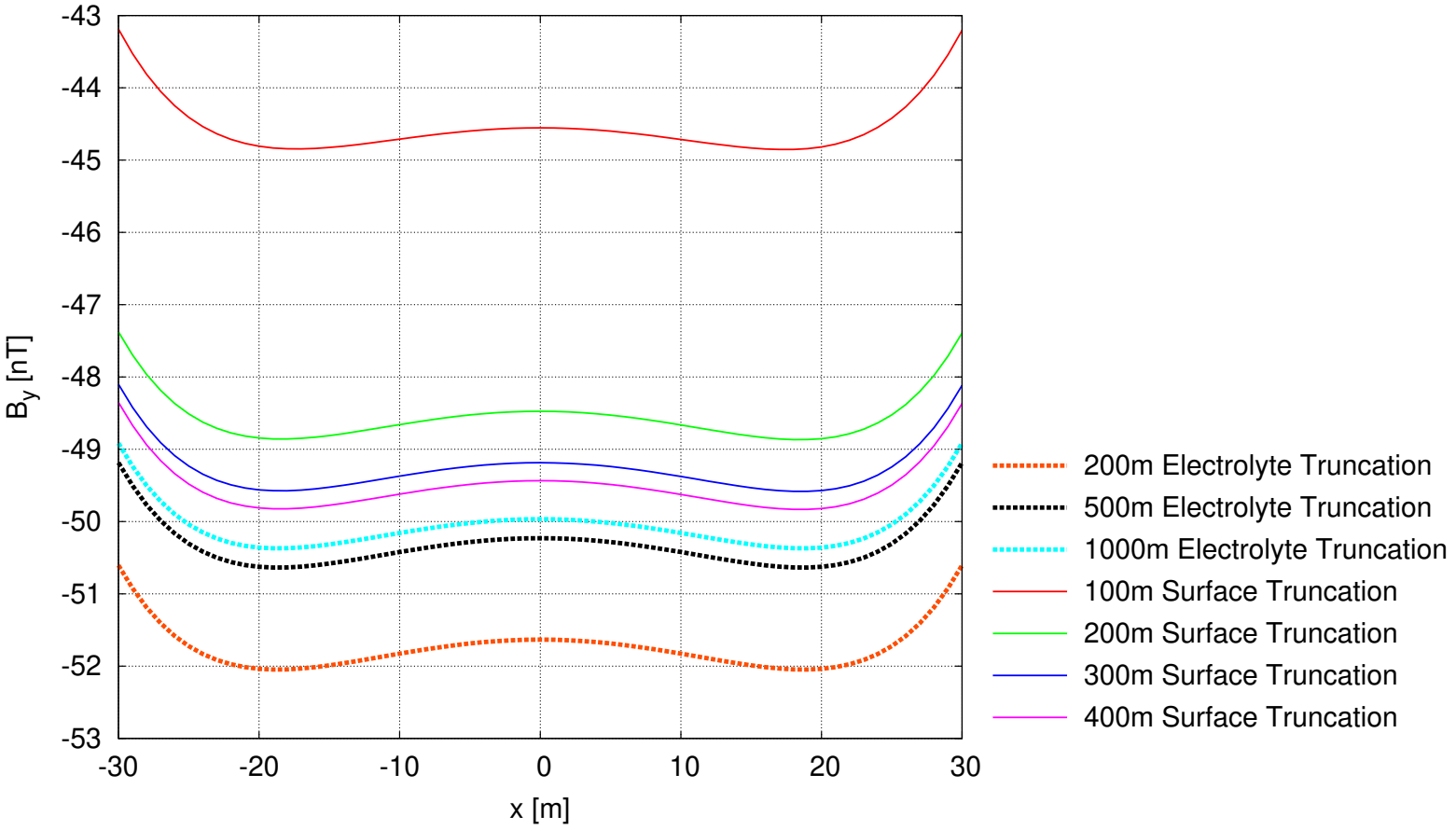

FIGURE 5.7: Magnified plot of y-directed B-field at a depth of $20\,\mathrm{m}$ below x-axis for CRM semi-cylindrical hull problem. Comparison of methods and discretizations. Integration tolerance is 10^{-6}.

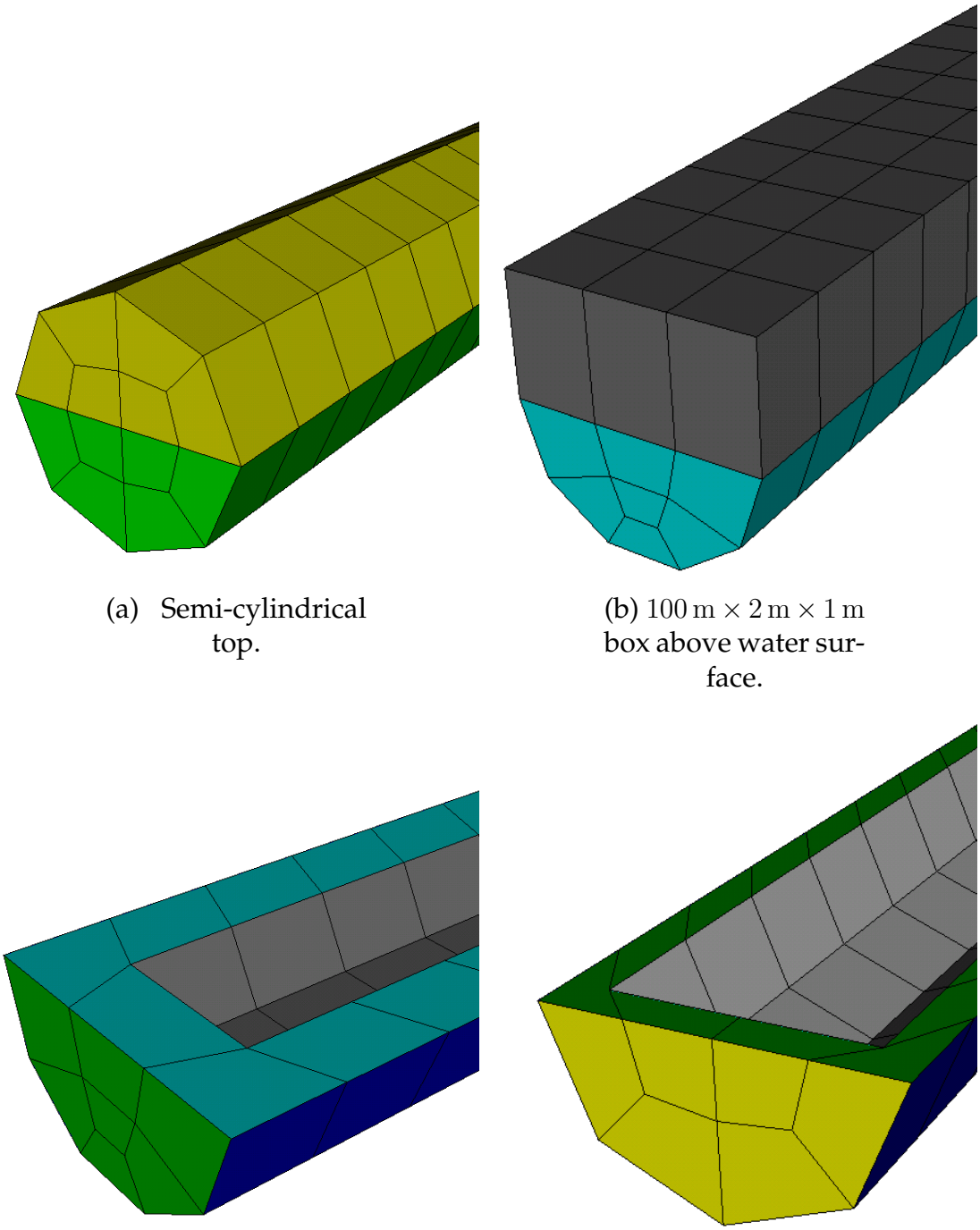

(a) Semi-cylindrical top.

(b) $100\,\mathrm{m} \times 2\,\mathrm{m} \times 1\,\mathrm{m}$ box above water surface.

(c) Semi-cylindrical shell, $0.5\,\mathrm{m}$ thickness.

(d) Semi-cylindrical shell, $0.25\,\mathrm{m}$ thickness.

FIGURE 5.8: Hull geometries used to compute structural current **H** for structure with semi-cylindrical hull.

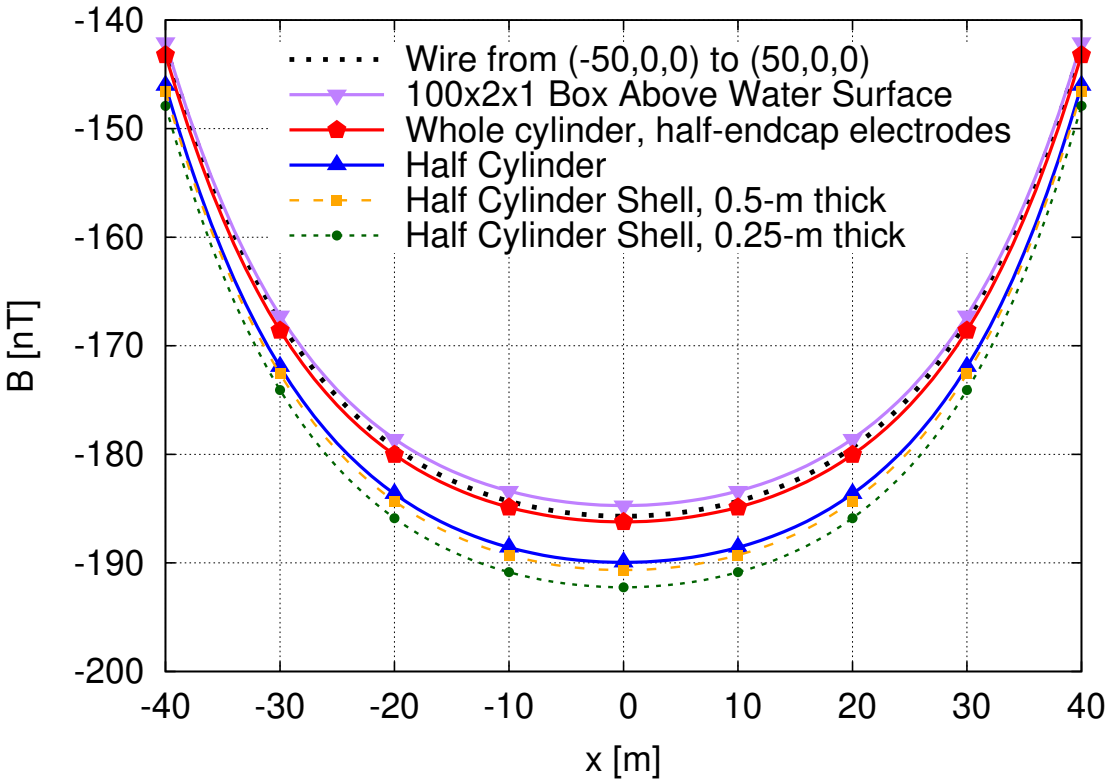

FIGURE 5.9: y-directed Structural **B**-field at a depth of $20\,\mathrm{m}$ below x-axis for different structural current configurations. Integration tolerance is 10^{-6}.

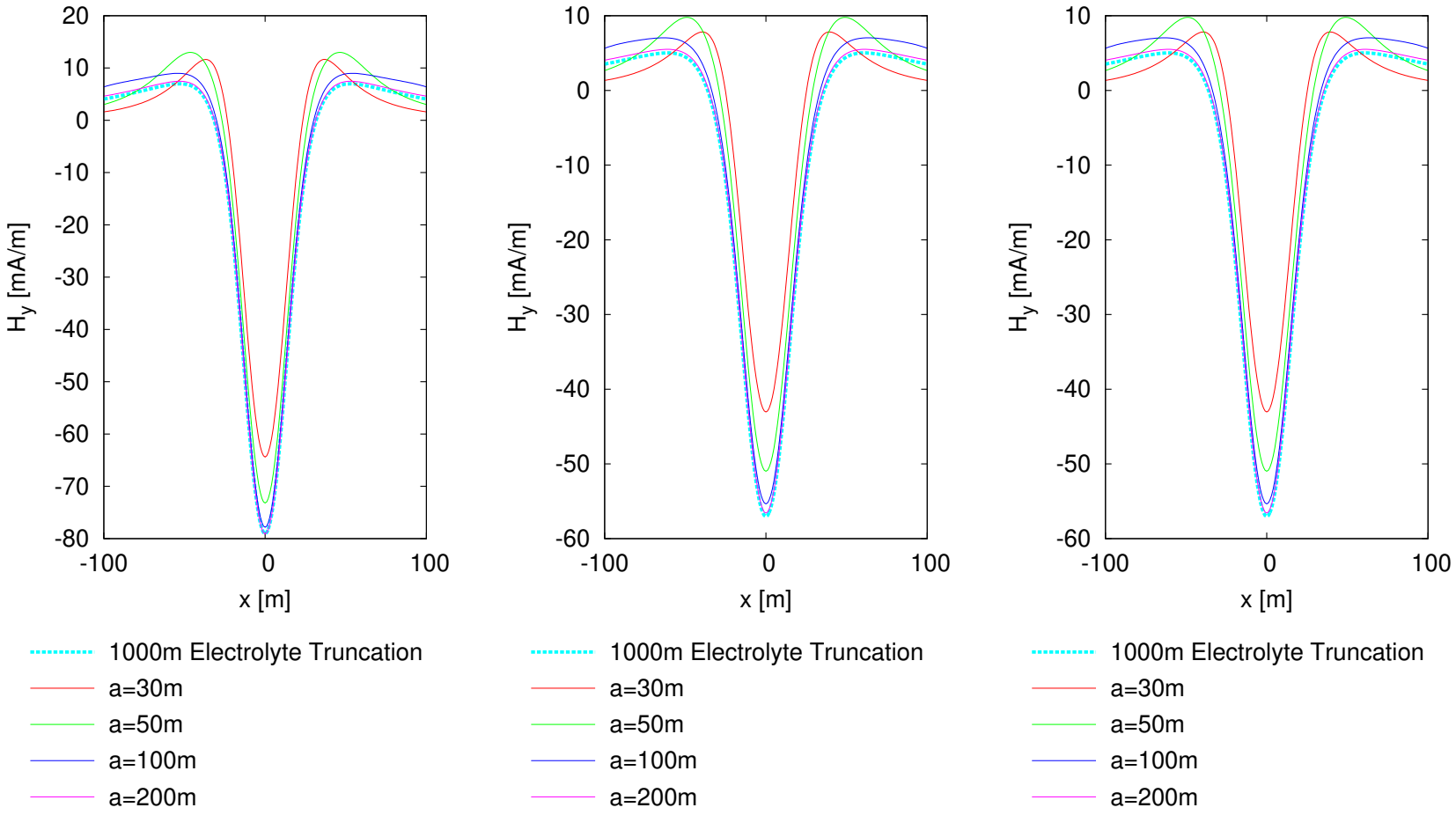

(a) Depth=$0\,\mathrm{m}$ (b) Depth=$2\,\mathrm{m}$ (c) Depth=$20\,\mathrm{m}$

FIGURE 5.10: y-directed magnetic field intensity $\mathbf{H}$ for rectangular box problem. Electrode currents $\{20\,\mathrm{A}, -20\,\mathrm{A}, -20\,\mathrm{A}, 20\,\mathrm{A}\}$. Integration tolerance is 10^{-6}.

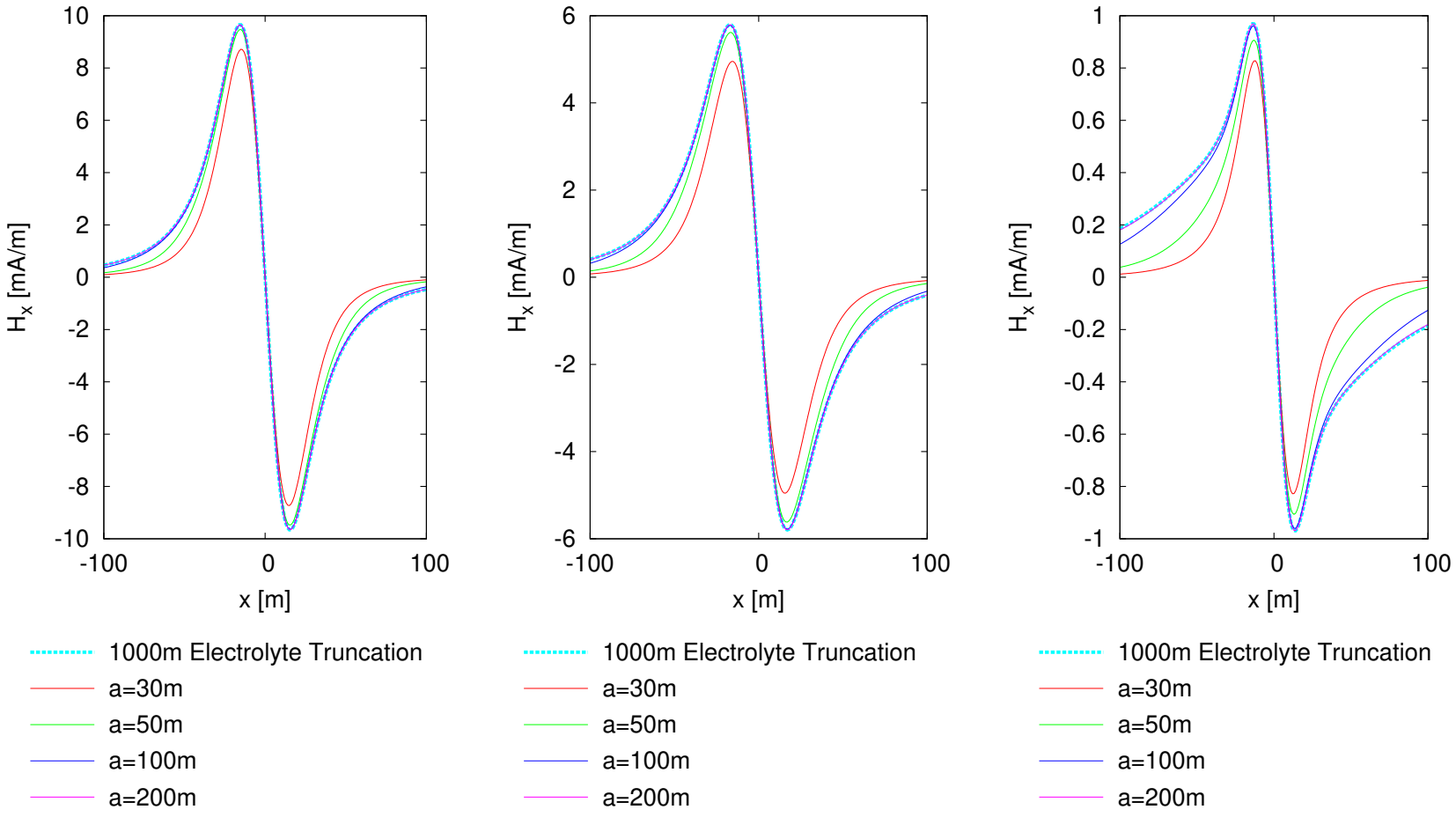

(a) Depth=$0\,\mathrm{m}$ (b) Depth=$2\,\mathrm{m}$ (c) Depth=$20\,\mathrm{m}$

FIGURE 5.11: x-directed magnetic field intensity $\mathbf{H}$ for rectangular box problem. Electrode currents $\{20\,\mathrm{A}, -20\,\mathrm{A}, 20\,\mathrm{A}, -20\,\mathrm{A}\}$(quadrupole). Integration tolerance is 10^{-6}.

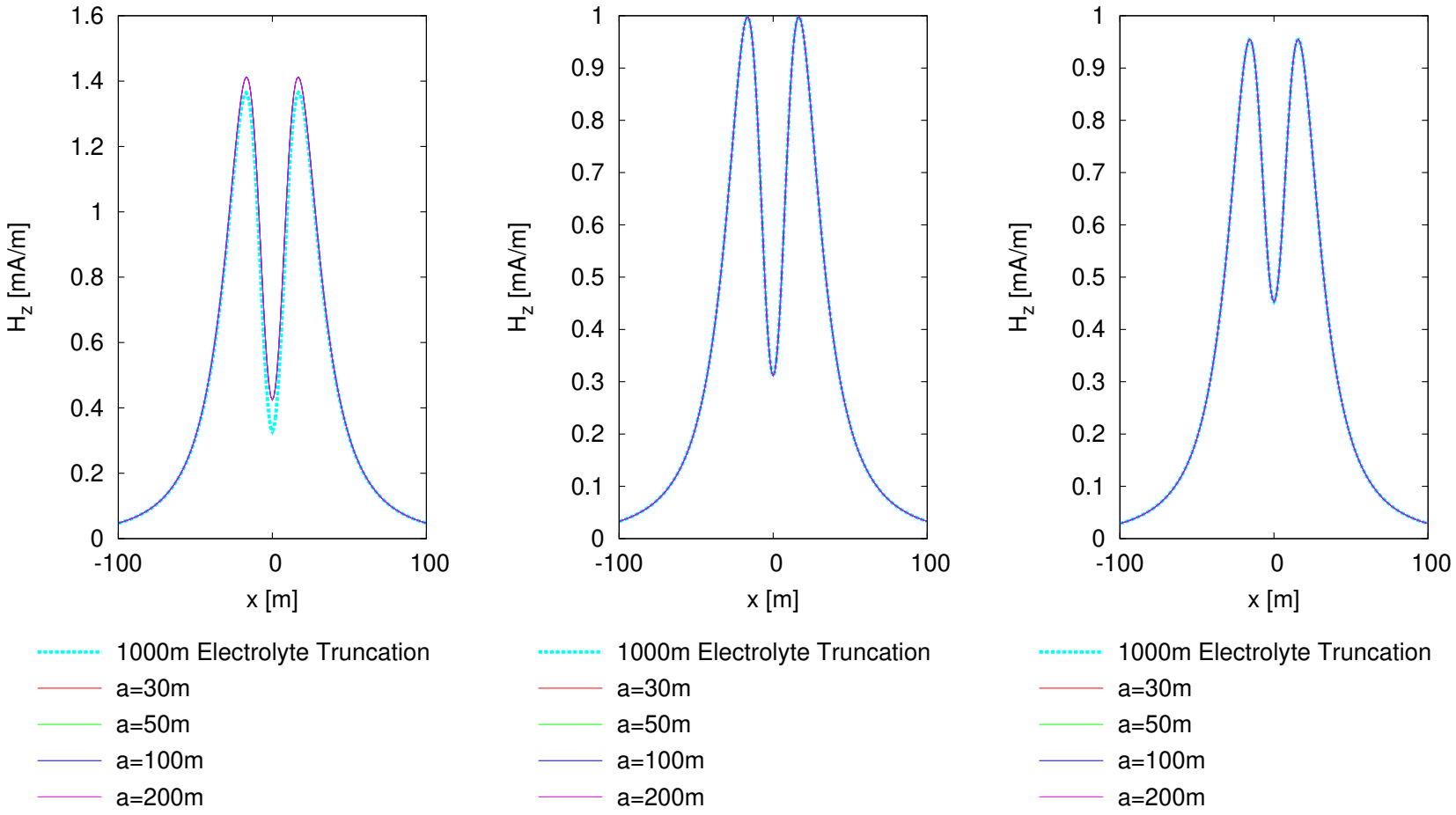

(a) Depth=$0\,\mathrm{m}$ (b) Depth=$2\,\mathrm{m}$ (c) Depth=$20\,\mathrm{m}$

FIGURE 5.12: z-directed magnetic field intensity $\mathbf{H}$ for rectangular box problem. Electrode currents $\{20\,\mathrm{A}, -20\,\mathrm{A}, 20\,\mathrm{A}, -20\,\mathrm{A}\}$(quadrupole). Integration tolerance is 10^{-6}.

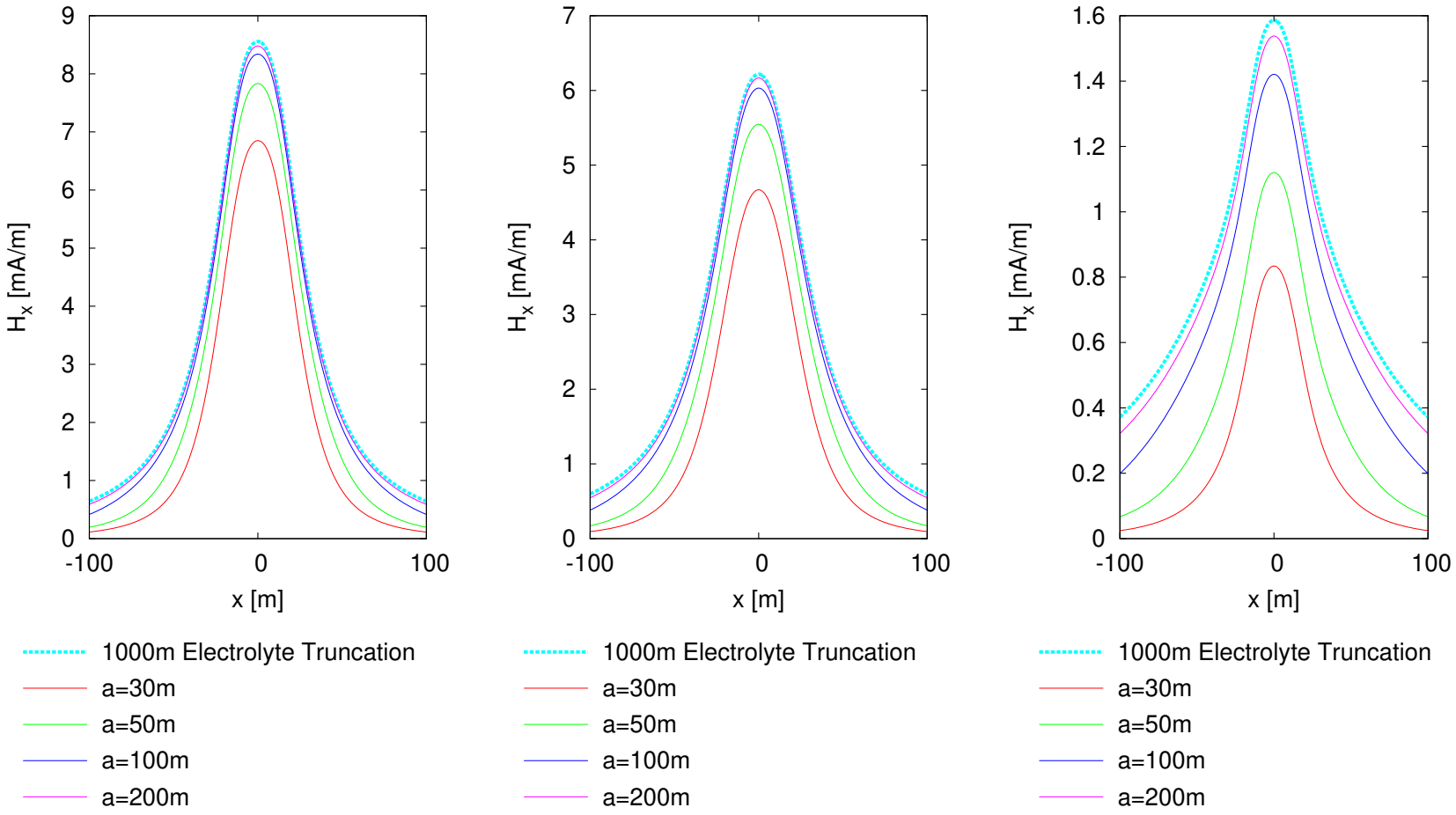

(a) Depth=0 m (b) Depth=2 m (c) Depth=20 m

FIGURE 5.13: x-directed magnetic field intensity $\mathbf{H}$ for rectangular box problem. Electrode currents $\{20\,\mathrm{A}, -10\,\mathrm{A}, -20\,\mathrm{A}, 10\,\mathrm{A}\}$. Integration tolerance is 10^{-6}.

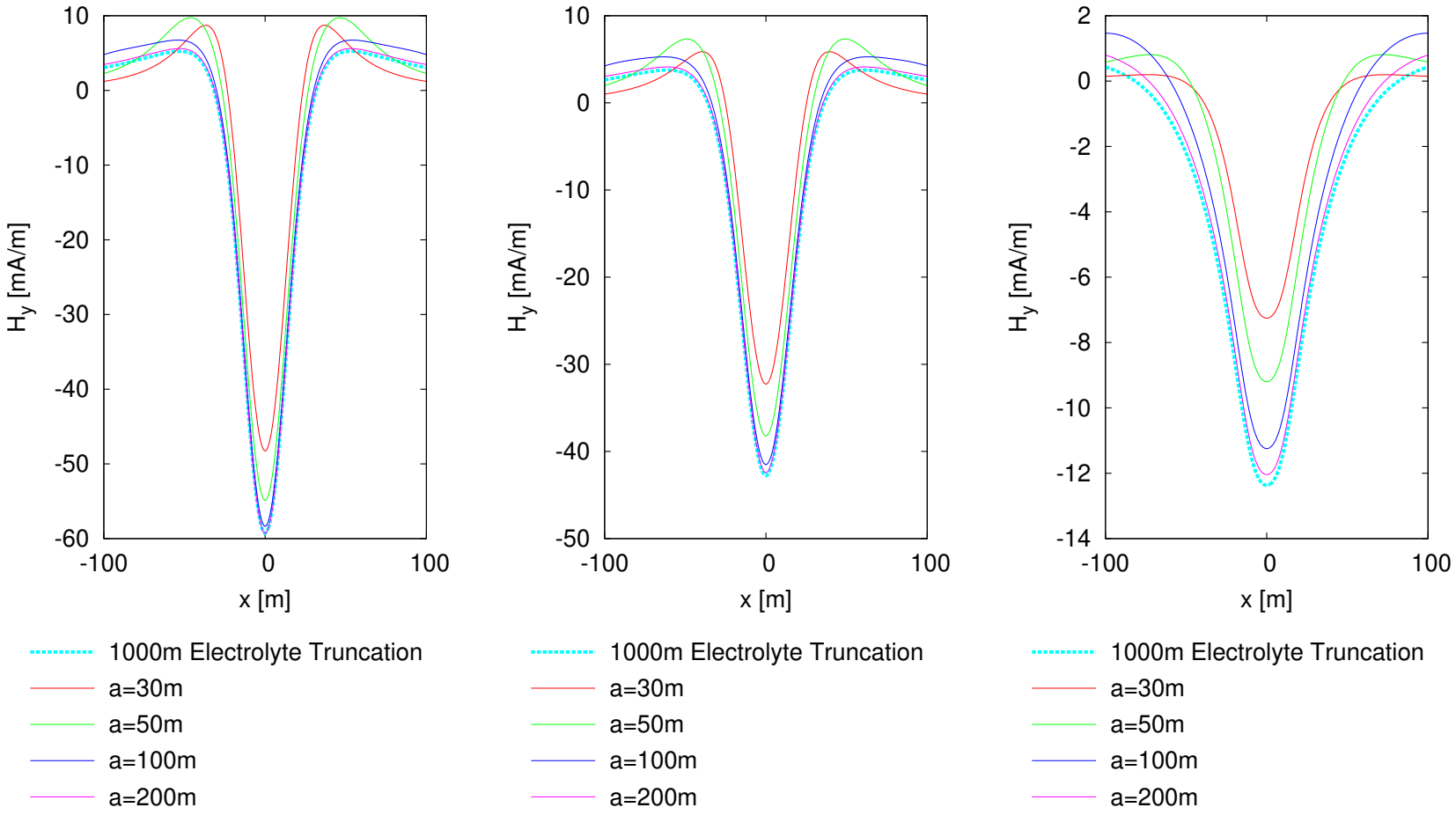

(a) Depth=$0\,\mathrm{m}$ (b) Depth=$2\,\mathrm{m}$ (c) Depth=$20\,\mathrm{m}$

FIGURE 5.14: y-directed magnetic field intensity $\mathbf{H}$ for rectangular box problem. Electrode currents $\{20\,\mathrm{A}, -10\,\mathrm{A}, -20\,\mathrm{A}, 10\,\mathrm{A}\}$. Integration tolerance is 10^{-6}.

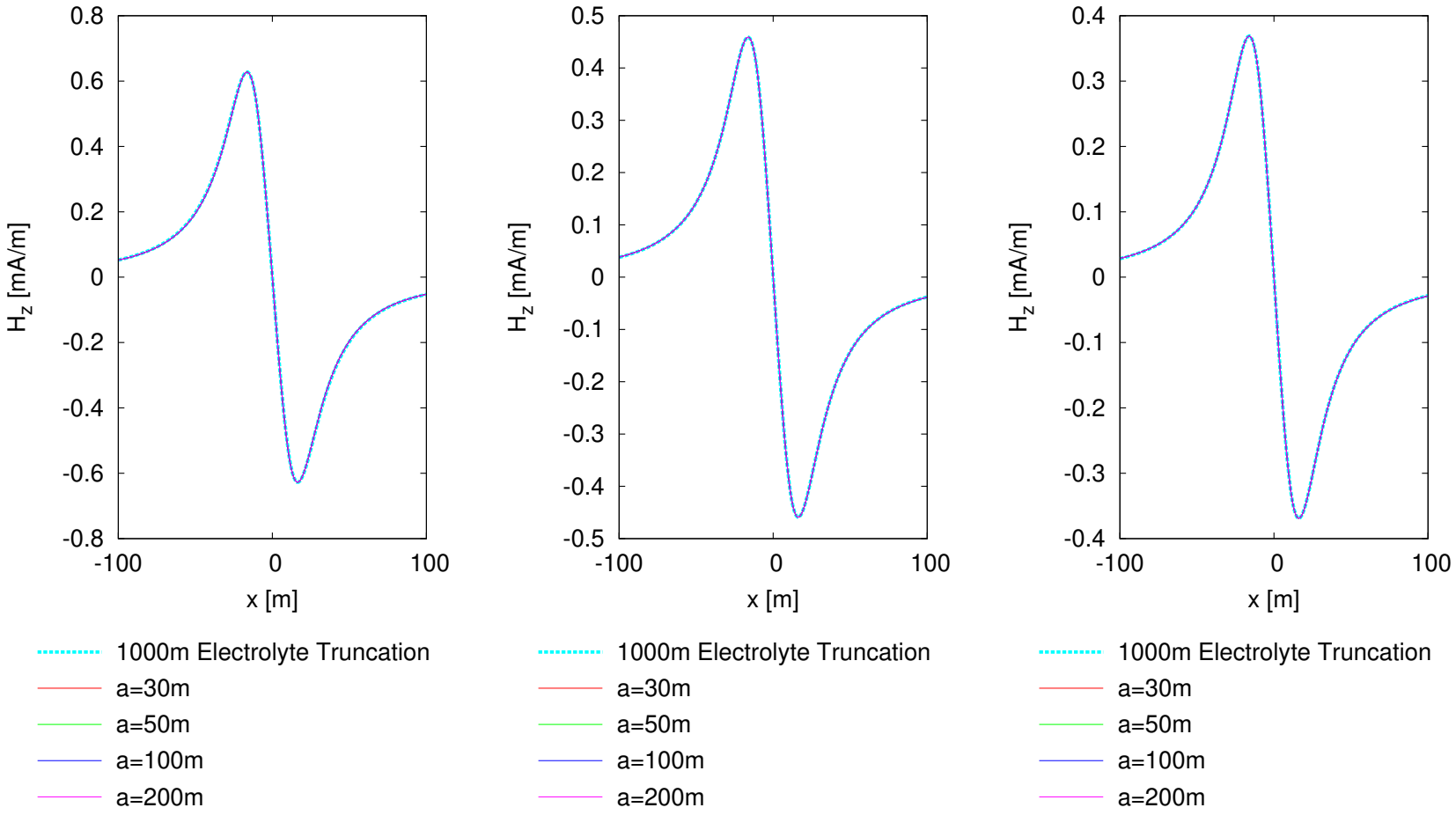

(a) Depth=$0\,\mathrm{m}$ (b) Depth=$2\,\mathrm{m}$ (c) Depth=$20\,\mathrm{m}$

FIGURE 5.15: z-directed magnetic field intensity $\mathbf{H}$ for rectangular box problem. Electrode currents $\{20\,\mathrm{A}, -10\,\mathrm{A}, -20\,\mathrm{A}, 10\,\mathrm{A}\}$. Integration tolerance is 10^{-6}.

CHAPTER 6. Conclusion

In this paper we have looked at methods for accurate computation of fields both from conducting-magnetic sources and from corrosion-related sources on marine structures. High-order Nyström discretizations are found to give a high degree of accuracy.

A set of hexahedral basis functions has been presented, characterized, and employed in solving quasi-magnetostatic problems using a volume integral equation via a general Nyström-moment method conversion for different basis orders and basis function types. It is found that the conversion, with the use of high-order, highly-orthogonal, divergence-conforming bases, maintains accuracy while reducing the number of degrees of freedom and improving the conditioning of the system, though this last effect is less pronounced when a preconditioner is used.

Corrosion-related fields, both electric and magnetic, are simulated using the locally corrected Nyström method. High-order error convergence for benchmark problems is observed, and the performance of various iterative solution techniques is compared for nonlinear problems. It is found that by imposing the normal current density, found on a structure's surface by solving an exterior problem, as a boundary condition on an interior problem for a structure with the same boundary, we can get a good approximation of the magnetic field due to the corrosion-protection currents flowing within the hull. This technique is compared with other existing approaches in terms of accuracy and practicality. A technique for solving corrosion problems with nonlinear boundary conditions is presented that reduces

the size of the matrix to be inverted at each iteration in a Newton-Raphson approach. A strategy for computing the corrosion-related magnetic fields due to corrosion currents flowing through a semi-infinite electrolyte is also described, and is shown to give accurate results while significantly reducing problem size.

6.1 Contributions

The theoretical and experimental contributions of this dissertation to the study of computational electromagnetics are outlined here:

- High-order constrained divergence-conforming volume basis functions
  - Characterization of high-order divergence-conforming basis functions for hexahedral cells numerically constructed using the SVD
  - Thorough algebraic analysis of high-order basis functions and application to constrained bases (Appendix A)
  - Application of Bases to Quasi-Magnetostatic problems using Nyström-MoM conversion
- Numerical simulation of corrosion-related electric and magnetic fields for structures in conducting medium
  - Implementation and characterization of a high-order locally corrected Nyström discretization of electrostatic problem
  - Use of Schur complement to render Newton-Raphson iterative solution of corrosion problems more efficient
  - Mathematical and computational investigation of surface-integral techniques for computation of both structural and volume corrosion-related magnetic fields (CRM)

  - Description of a discrete-source approximation method for CRM calculation
  - Presentation of an analytic test problem for comparison with surface-integral and discrete-source solutions
  - Indirect application of image method for more efficient calculation of CRM fields in semi-infinite medium

- Other general contributions
  - Presentation of general method of Nyström-MoM Conversion for high-order simulations
  - Geometric and numerical description of the failure documented in [11] for integration of kernels with a $\frac{1}{|\mathbf{r}-\mathbf{r}'|}$ singularity on curvilinear surfaces (Appendix B)

6.2 Future Work

Further investigation remains to be done in several topics connected with the work presented in this paper, particularly relating to cathodic protection simulation. One topic is the efficient modeling of structures in shallow water, where both the water surface and the ocean floor affect the corrosion currents and fields. A natural approach is to truncate the electrolyte and solve the resulting interior problem, but the use of image methods using multiple image planes may be a desirable alternative.

In Chapters 4 and 5 of this paper a medium of uniform conductivity was assumed. This is not a valid assumption for some structures, e.g., oil rigs that extend from the surface to great depths through water of varying salinity. The necessary adjustments to the methods presented here in order to apply them to such

problems, perhaps by employing layered-media Green's functions, remain to be investigated.

As mentioned in [57], fast solver methods have been applied successfully to corrosion modeling problems. The Schur complement approach used in Chapter 4 in conjunction with the Newton-Raphson method was developed with the use of fast solvers in mind. While the method has been validated and shown to improve efficiency in a dense system solution, its performance with fast-solver techniques has yet to be tested.

APPENDIX A. Notes on High Order Constrained Bases

A.1 Algebraic Properties of High Order Vector Bases

The constrained basis functions in Chapter 2 are constructed to give a mixed-order representation of fields and currents, that is, for bases of order p, the basis $\mathbf{B}_m^{q,i} = B_m^{q,i}\mathbf{a}_i$ is polynomial complete to order $p+1$ in u^i, but only to order p in $u^{j\neq i}$. This makes the divergence of $\mathbf{B}_m^{q,i}$ complete to order p in u^1, u^2, and u^3, resulting in a polynomial complete representation of charge (cf. [64]). We thus have functions of the form

$$B_m^{q,i} \in \mathbb{R}[{u^i}_{\deg\leq p+1}, {u^j}_{\deg\leq p}, {u^k}_{\deg\leq p}]. \tag{A.1}$$

where $\mathbb{R}[x_{1\deg\leq p_1}, x_{2\deg\leq p_2}, x_{3\deg\leq p_3}]$ signifies the space of polynomials in x_1, x_2, x_3, with real coefficients, of order not greater than p_i in x_i. The function space in (A.1) has dimension $(p+2)(p+1)^2$.

Since, by definition, $\mathbf{a}_i \cdot \hat{\mathbf{n}}$ is nonzero only on F_i and F_{i+3}, the constraints imposed in Section 2.1.1 are implicitly fulfilled on the other four faces. If $B_m^{q,i}$ is also zero on the face F_i or F_{i+3}, then it will have a factor u^i or $u^{i+3} = u^i - 1$, respectively. Thus a half basis for the face F_i has the form

$$(u^i - 1) f(u^i, u^j, u^k), f \in \mathbb{R}[{u^i}_{\deg\leq p}, {u^j}_{\deg\leq p}, {u^k}_{\deg\leq p}]$$

indicating that the space $\mathbf{F}_{half}$ spanned by the half bases has dimension $(p+1)^3$. Similarly the volume bases in the u^i direction can be written as

$$u^i(u^i - 1) f(u^i, u^j, u^k), f \in \mathbb{R}[{u^i}_{\deg\leq p-1}, {u^j}_{\deg\leq p}, {u^k}_{\deg\leq p}]$$

so that the function space $\mathbf{F}_{volume}$ spanned by volume bases in the u^i direction on V_m has dimension $p(p+1)^2$.

Face bases defined on adjacent cell pairs are somewhat more complicated as the entire face basis has support over two adjacent cells, and must have a continuous normal component at the shared face and a zero normal component elsewhere. Let the faces F^m_{i+3} and F^n_{r+3} belonging to adjacent cells V_m and V_n be coincident, and let the transverse coordinates u^j and u^k on cell m correspond to u^s and u^t on cell n, respectively, so that $(u^j, u^k) = (u^s, u^t)$ at any given point on the shared face. Then the constraint on the shared face is

$$B^{q,i}_m(u^i, u^j, u^k)\mathbf{a}_i \cdot \hat{\mathbf{n}}^m(\mathbf{r}) = -B^{q,r}_n(u^r, u^s, u^t)\mathbf{a}_r \cdot \hat{\mathbf{n}}^n(\mathbf{r}) \tag{A.2}$$

where $\hat{\mathbf{n}}^\ell(\mathbf{r})$ is the outward normal from cell ℓ at $\mathbf{r}$. Define

$$t^m(u^i, u^j, u^k) = u^i \qquad \mathbf{r} \in V_m \tag{A.3}$$

$$t^n(u^r, u^s, u^t) = -\left(\frac{\mathbf{a}_i(u^j, u^k) \cdot \hat{\mathbf{n}}^m(u^j, u^k)}{\mathbf{a}_r(u^s, u^t) \cdot \hat{\mathbf{n}}^n(u^s, u^t)}\right) u^r \qquad \mathbf{r} \in V_n \tag{A.4}$$

where the normal and unitary vectors are evaluated at $u^i = u^r = 1$, the two functions make up a function $t^{mn}(\mathbf{r})$, analogous to a triangle or rooftop function, that satisfies (A.2). Now from any $B_{mn}(\mathbf{r})$ satisfying (A.2) one can subtract some function f^{mn} of the form

$$f^{mn}(\mathbf{r}) = t^{mn}(\mathbf{r})g(u^\iota, u^\kappa),\ g(u^\iota, u^\kappa) \in \mathbb{R}[u^\iota_{\deg\leq p}, u^\kappa_{\deg\leq p}], \tag{A.5}$$

where

$$(\iota, \kappa) = \begin{cases} (j,k) & \mathbf{r} \in V_m \\ (s,t) & \mathbf{r} \in V_n \end{cases}.$$

This leaves a function $B_{mn} - f^{mn}$ that is identically zero at the shared face and

at each of the opposite faces. Thus any face basis can be written as the sum of three linearly independent functions, namely a function $f^{mn}(\mathbf{r})$ and two volume bases, one for each of V_m and V_n. Since the space of functions resembling (A.5) is of dimension $(p+1)^2$, the overall function space $\mathbf{F}_{face}$ satisfying (A.2) has dimension $(p+1)^2 + 2 \cdot p(p+1)^2 = (2p+1)(p+1)^2$.

Of course, for computational purposes, we wish to remove the volume basis spaces from the face basis space to avoid the redundancy noted in Section 2.1.3. The face basis and half basis spaces, therefore, are defined with the further qualification that they exclude the space of the volume bases. The half basis, face basis, and volume basis spaces are therefore seen to have the dimensions

$$\dim \mathbf{F}_{half} = (p+1)^2 \tag{A.6}$$

$$\dim \mathbf{F}_{face} = (p+1)^2 \tag{A.7}$$

$$\dim \mathbf{F}_{volume} = p(p+1)^2 \tag{A.8}$$

so that there are $(p+1)^2$ face or half bases associated with each face of a hexahedral cell, and $3p(p+1)^2$ volume bases with each cell.

APPENDIX B. Notes on Corrosion Protection Simulation

B.1 Failure Due to Machine Precision

In surface integral equations such as that encountered in Chapter 4, the term

$$\oint_s \Phi(\mathbf{r}')\boldsymbol{\nabla}' G(\mathbf{r},\mathbf{r}')\cdot\hat{\mathbf{n}}' dS' = \frac{-1}{4\pi}\oint_S \Phi(\mathbf{r}')\frac{\hat{\mathbf{R}}\cdot\hat{\mathbf{n}}'}{R^2}dS' \tag{B.1}$$

where $\mathbf{R} = \mathbf{r} - \mathbf{r}'$ is problematic when the field point $\mathbf{r}$ is on S and S is curvilinear. On a smooth surface, the $1/R^2$ singularity is canceled in part by the surface integration (e.g. by using a Duffy integration scheme [81, 82]) and in part by the vanishing of $\hat{\mathbf{R}}\cdot\hat{\mathbf{n}}$. [1] On curvilinear mesh elements, however, the dot product $\hat{\mathbf{R}}\cdot\hat{\mathbf{n}}$ ceases to vanish as R and instead behaves erratically as R decreases, with an upper bound that varies as $1/R$ rather than R. Thus the singularity is not canceled and

[1] Consider a point $\mathbf{r}'$ on a smooth curved surface S approaching along some curved path C toward $\mathbf{r}$. And let $\hat{\mathbf{n}}'$ be the normal to S at $\mathbf{r}'$. Let P be the center of the osculating circle for C at $\mathbf{r}$. Then in the limit as $\mathbf{r}' \to \mathbf{r}$, the dot product $\hat{\mathbf{R}}\cdot\hat{\mathbf{n}}'$, that is, $\cos\alpha$ or $\sin\beta$, becomes equal to $\sin\frac{\theta}{2}$, that is, to $R/2a$. Thus $|\hat{\mathbf{n}}'\cdot\hat{\mathbf{R}}|$ ultimately approaches 0 as R.

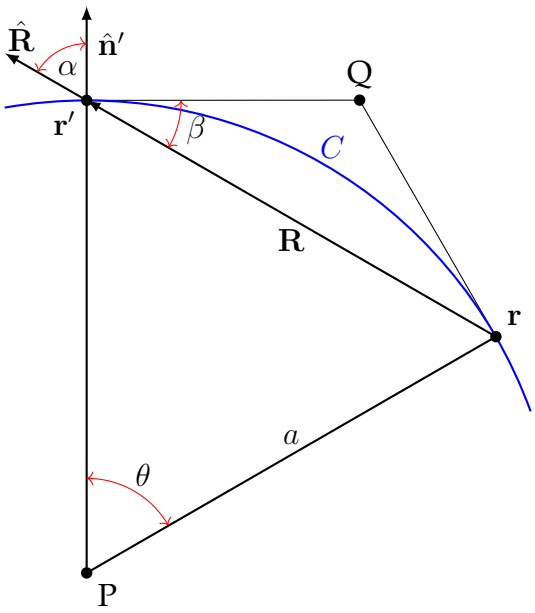

the integration does not converge. This happens when R reaches approximately the square root of machine precision, as shown in Fig. B.1, where $\hat{\mathbf{R}} \cdot \hat{\mathbf{n}}$ is calculated as $R \to 0$ on a sphere described by the Sylvester polynomials (cf. [33]). Different machine precision values are simulated using the Python arbitrary-precision library `mpmath`.

Essentially the same effect has been noted for the magnetic field integral equation (MFIE) [11], where it limits the accuracy of the solution to a relative error of about 10^{-8}. The fact that $\hat{\mathbf{R}} \cdot \hat{\mathbf{n}}$ can behave as $1/R$ when R is small enough means that when the numerical integration is refined for greater accuracy, it actually becomes less accurate rather than merely stagnating at the square root of machine precision (as in Fig. 4.1).

The cause of the issue can be seen by breaking $\mathbf{R}$ into components normal (R_{norm}) and tangential (R_{tan}) to the path of approach C at $\mathbf{r}$. This is diagrammed in Fig. B.2. It is easily shown that the angle between the tangent and $\mathbf{R}$ becomes half the angle θ at the center P of the osculating circle as $\mathbf{r}' \to \mathbf{r}$. The tangential component $R_{tan} = R\cos\frac{\theta}{2}$ ultimately becomes proportional to R as $\mathbf{r}' \to \mathbf{r}$, while the normal component $R_{norm} = R\sin\frac{\theta}{2}$ falls off as $R \cdot \frac{R}{2a}$ where a is the radius of curvature at $\mathbf{r}$.

Figure B.3 shows the $O(R)$ and $O(R^2)$ behavior of the computed R_{tan} and R_{norm}, respectively, as $\mathbf{r}' \to \mathbf{r}$. In the two-dimensional case where $\mathbf{r}'$ approaches $\mathbf{r}$ on the circumference of a circle, this behavior can be corrected by dropping the component of $|\mathbf{r}' - \mathbf{r}|$ from calculations when R reaches the square root of machine precision, as the tangential portion becomes ultimately equal to R (cf. Newton, *Principia*, Lemma 7). The resulting "corrected" behavior of $\hat{\mathbf{n}}' \cdot \hat{\mathbf{R}}$ is shown in Fig. B.4. Further work is necessary to determine the best strategy for correcting the behavior of $\hat{\mathbf{n}}' \cdot \hat{\mathbf{R}}$ on three-dimensional geometries of arbitrary curvature.

B.2 Notes on Surface Integral Computation of CRM Fields

The integral in (5.5) has a strong singularity when $\mathbf{r}$ is on the source cell S_n. This can be dealt with in two ways. We can take advantage of the identity

$$\iint_S \hat{\mathbf{n}} \times \boldsymbol{\nabla}\psi dS = \oint_{\partial S} \psi d\mathbf{C} \tag{B.2}$$

to extract the singularity as

$$\begin{aligned}\iint_{S_n} \hat{\mathbf{n}}' \times \Phi(\mathbf{r}')\boldsymbol{\nabla}' G dS' &= \iint_{S_n} \hat{\mathbf{n}}' \times \Phi(\mathbf{r})\boldsymbol{\nabla}' G dS' \\ &\quad - \iint_{S_n} \hat{\mathbf{n}}' \times (\Phi(\mathbf{r}) - \Phi(\mathbf{r}'))\, \boldsymbol{\nabla}' G dS' \\ = \Phi(\mathbf{r}) \oint_{\partial S_n} G(\mathbf{r}, \mathbf{r}') d\mathbf{C}' &- \iint_{S_n} \hat{\mathbf{n}}' \times (\Phi(\mathbf{r}) - \Phi(\mathbf{r}'))\, \boldsymbol{\nabla}' G dS'. \end{aligned} \tag{B.3}$$

An alternative is to note that for a closed surface S, (B.2) implies that

$$\oiint_S \hat{\mathbf{n}} \times \boldsymbol{\nabla}\psi dS = 0. \tag{B.4}$$

from which we find that

$$\begin{aligned}\oiint_S \hat{\mathbf{n}}' \times (\Phi(\mathbf{r}')\boldsymbol{\nabla}' G)\, dS' &= \oiint_S \hat{\mathbf{n}}' \times [\boldsymbol{\nabla}'(\Phi(\mathbf{r}')G) - G\boldsymbol{\nabla}'\Phi(\mathbf{r}')]\, dS' \\ &= \cancelto{0}{\oiint_S \hat{\mathbf{n}}' \times \boldsymbol{\nabla}'(\Phi(\mathbf{r}')G)\, dS'} - \oiint_S \hat{\mathbf{n}}' \times G\boldsymbol{\nabla}'\Phi(\mathbf{r}') dS' \\ &= -\oiint_S \frac{\hat{\mathbf{n}}' \times \boldsymbol{\nabla}'\Phi(\mathbf{r}')}{|\mathbf{r} - \mathbf{r}'|} dS'. \end{aligned} \tag{B.5}$$

Since this approach requires the computation of a gradient (computed on a cell's parametric coordinates as $\boldsymbol{\nabla}\Phi(u^1, u^2) = \sum_{i=1}^{2} \frac{\partial \Phi}{\partial u^i}\mathbf{a}^i$, [63]) it therefore requires at least a linear approximation of Φ. This means that the basis order p must be greater than zero for a moment-method approach and that the $n \times n$ test grid used in a Nyström

approach must have $n > 1$. One advantage to this approach is that it allows one to integrate a single surface integrand over the entire surface, without the need for a special surface and line integration near the singular point.

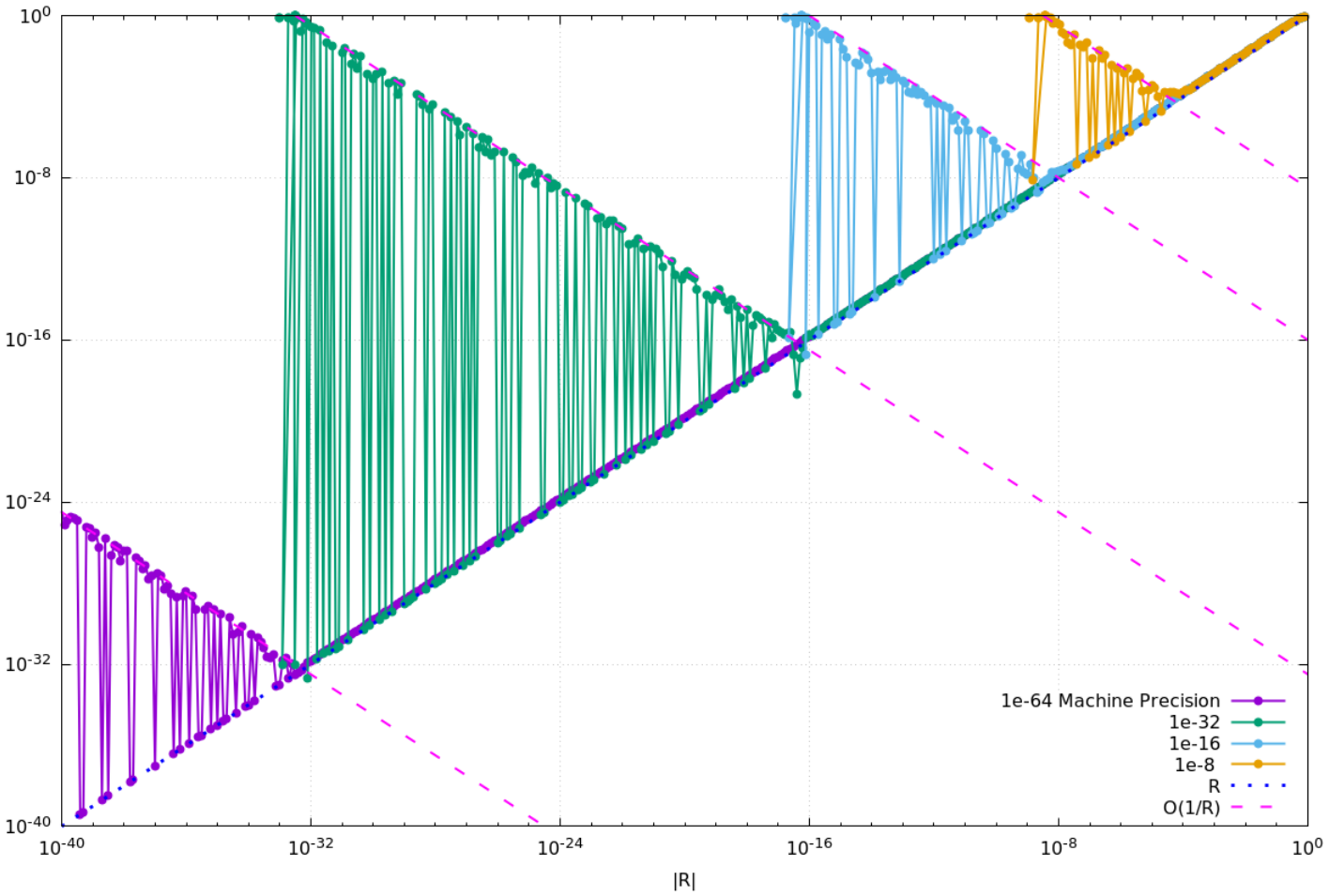

FIGURE B.1: $\hat{\mathbf{n}} \cdot \hat{\mathbf{R}}$ for different machine precision settings on a sphere.

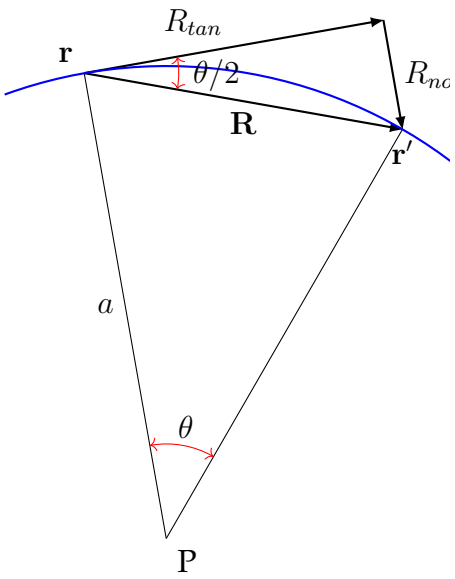

FIGURE B.2: Geometry of $\mathbf{r}' \to \mathbf{r}$ on S discussed on page 136.

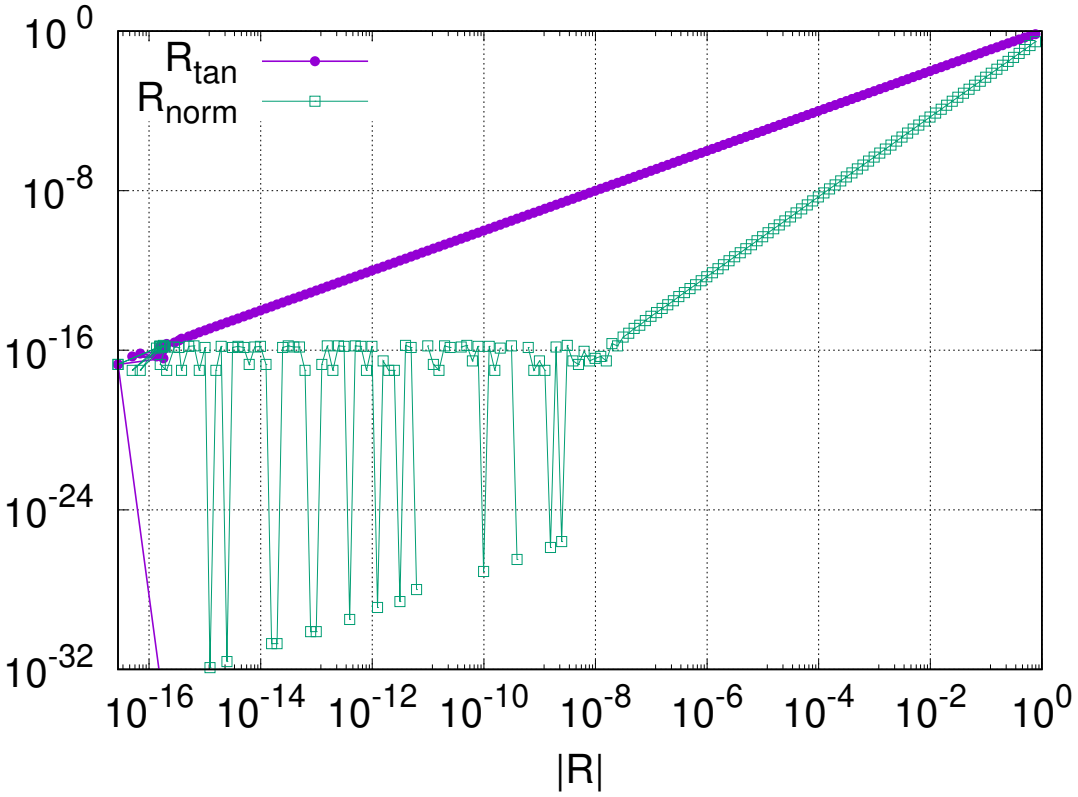

FIGURE B.3: Numerical behavior of $\mathbf{R}$ components as $R \to 0$ in 10^{-16} precision at $\theta = 45°$.

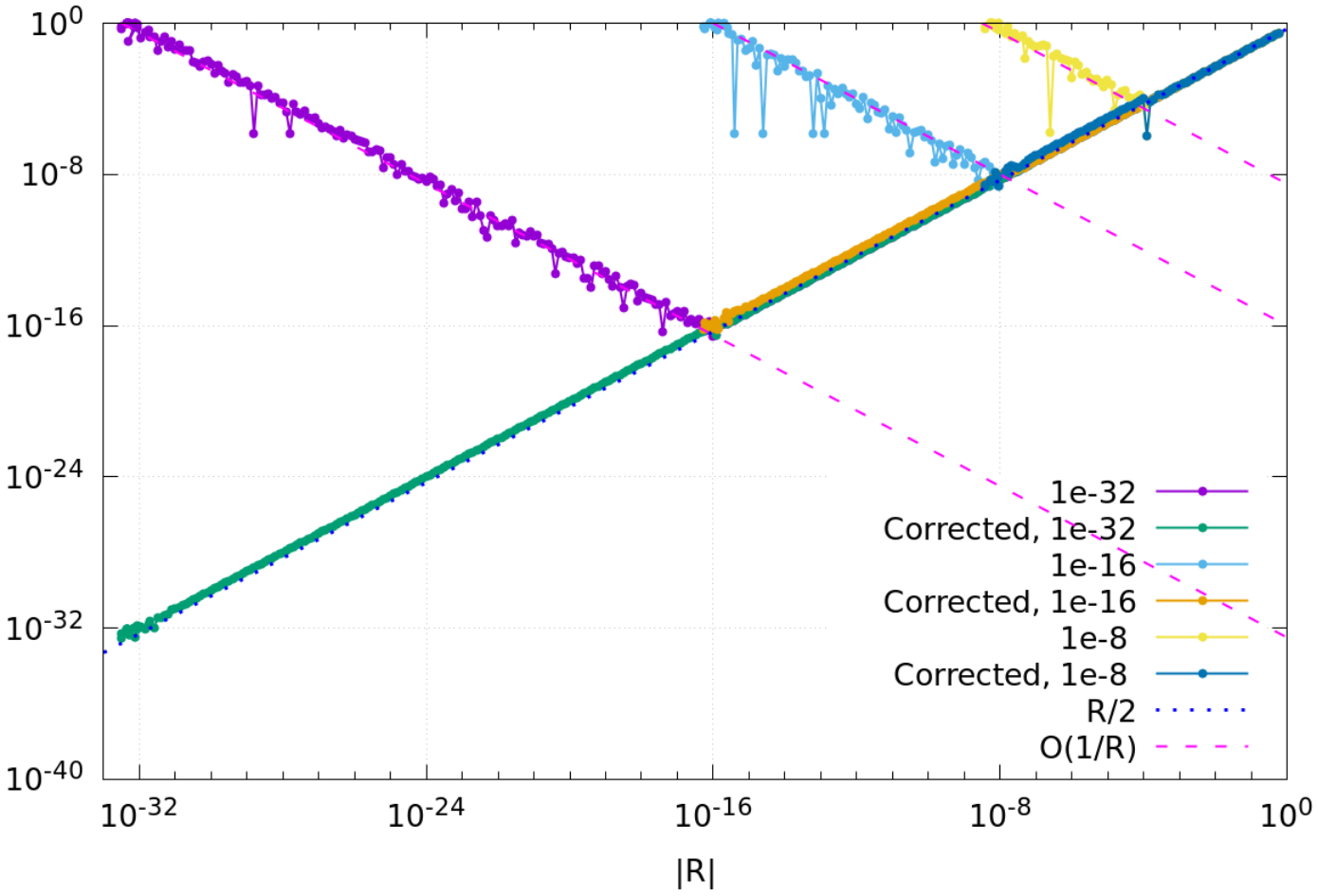

FIGURE B.4: $\hat{\mathbf{n}}' \cdot \hat{\mathbf{R}}$ for different machine precision settings on a sphere with and without correction by removal of R_{norm}.

References

[1] S. Rao, D. Wilton, and A. Glisson, "Electromagnetic scattering by surfaces of arbitrary shape," IEEE Transactions on Antennas and Propagation, vol. 30, pp. 409–418, May 1982.

[2] A. Glisson and D. Wilton, "Simple and efficient numerical methods for problems of electromagnetic radiation and scattering from surfaces," IEEE Transactions on Antennas and Propagation, vol. 28, pp. 593–603, Sep 1980.

[3] B. J. Rubin and S. Daijavad, "Radiation and scattering from structures involving finite-size dielectric regions," IEEE Transactions on Antennas and Propagation, vol. 38, pp. 1863–1873, Nov 1990.

[4] D. Schaubert, D. Wilton, and A. Glisson, "A tetrahedral modeling method for electromagnetic scattering by arbitrarily shaped inhomogeneous dielectric bodies," IEEE Transactions on Antennas and Propagation, vol. 32, pp. 77–85, Jan 1984.

[5] M. Djordjevic and B. M. Notaros, "Double higher order method of moments for surface integral equation modeling of metallic and dielectric antennas and scatterers," IEEE Transactions on Antennas and Propagation, vol. 52, pp. 2118–2129, Aug 2004.

[6] B. M. Notaros and B. D. Popovic, "General entire-domain method for analysis of dielectric scatterers," IEE Proceedings - Microwaves, Antennas and Propagation, vol. 143, pp. 498–504, Dec 1996.

[7] F. Valdes, F. P. Andriulli, K. Cools, and E. Michielssen, "High-order div- and quasi curl-conforming basis functions for Calderòn multiplicative preconditioning of the efie," IEEE Transactions on Antennas and Propagation, vol. 59, pp. 1321–1337, April 2011.

[8] B. M. Notaros, "Higher order frequency-domain computational electromagnetics," IEEE Transactions on Antennas and Propagation, vol. 56, pp. 2251–2276, Aug 2008.

[9] E. Jorgensen, J. Volakis, P. Meincke, and O. Breinbjerg, "Higher order hierarchical Legendre basis functions for electromagnetic modeling," IEEE Transactions on Antennas and Propagation, vol. 52, p. 2985–2995, Nov 2004.

[10] M. M. Kostic and B. M. Kolundzija, "Maximally orthogonalized higher order bases over generalized wires, quadrilaterals, and hexahedra," IEEE Transactions on Antennas and Propagation, vol. 61, p. 3135–3148, June 2013.

[11] R. A. Pfeiffer, J. C. Young, and R. J. Adams, "Numerical characterization of divergence-conforming constrained basis functions for surface integral equations," IEEE Transactions on Antennas and Propagation, vol. 65, pp. 1867–1874, Feb 2017.

[12] N. Hendijani, J. Cheng, R. J. Adams, and J. C. Young, "Constrained locally corrected Nyström method," IEEE Transactions on Antennas and Propagation,

vol. 63, pp. 3111–3121, July 2015.
[13] N. Hendijani, The Constrained Locally Corrected Nyström Method. PhD thesis, University of Kentucky, Lexington, 2015.
[14] R. Pfeiffer, "Constrained divergence-conforming basis functions for method of moments discretizations in electromagnetics," Master's thesis, University of Kentucky, Lexington, 2015.
[15] J. C. Young and R. J. Adams, "High-order divergence-conforming constrained bases for triangular cells," IEEE Transactions on Antennas and Propagation, vol. 65, pp. 4717–4727, Sept 2017.
[16] R. Pasquetti and F. Rapetti, "Spectral element methods on triangles and quadrilaterals: Comparisons and applications," Journal of Computational Physics, vol. 198, pp. 349–362, Feb 2004.
[17] T. Koornwinder, "Two-variable analogues of the classical orthogonal polynomials," Theory and Application of Special Functions, p. 435–495, 1975.
[18] R. A. Pfeiffer, J. C. Young, and R. J. Adams, "Divergence-conforming constrained basis functions for hexahedral volume elements," IEEE Transactions on Antennas and Propagation, vol. 66, pp. 501–504, Jan 2018.
[19] J. P. Adriaens, F. Delince, P. Dular, A. Genon, W. Legros, and A. Nicolet, "Vector potential boundary element method for three dimensional magnetostatic," IEEE Transactions on Magnetics, vol. 27, pp. 3808–3810, Sept 1991.
[20] W. M. Rucker and K. R. Richter, "Three-dimensional magnetostatic field calculation using boundary element method," IEEE Transactions on Magnetics, vol. 24, pp. 23–26, Jan 1988.
[21] S. Balasubramanian, S. N. Lalgudi, and B. Shanker, "Fast-integral-equation scheme for computing magnetostatic fields in nonlinear media," IEEE Transactions on Magnetics, vol. 38, pp. 3426–3432, Dec 2002.
[22] L. F. Canino, J. J. Ottusch, M. A. Stalzer, J. L. Visher, and S. M. Wandzura, "Numerical solution of the helmholtz equation in 2d and 3d using a high-order Nyström discretization," Journal of Computational Physics, vol. 146, p. 627–663, Aug 1998.
[23] S. D. Gedney and J. C. Young, The Locally Corrected Nyström Method for Electromagnetics, pp. 149–198. New York, NY: Springer New York, 2014.
[24] Z. Szabó and A. Iványi, "Adjustment with magnetic field," COMPEL - The international journal for computation and mathematics in electrical and electronic engineering, vol. 22, 2003.
[25] W. Hafla, A. Buchau, and W. M. Rucker, "Consideration of scalar magnetic hysteresis with the integral equation method," IEEE Transactions on Magnetics, vol. 44, pp. 910–913, June 2008.
[26] J. C. Young and S. D. Gedney, "A locally corrected Nyström formulation for the magnetostatic volume integral equation," IEEE Transactions on Magnetics, vol. 47, no. 9, pp. 2163–2170, 2011.
[27] J. C. Young, S. D. Gedney, and R. J. Adams, "Eddy current analysis using a Nyström-discretization of the volume integral equation," IEEE Transactions on Magnetics, vol. 49, no. 12, pp. 5675–5681, 2013.

[28] J. C. Young, R. J. Adams, and S. D. Gedney, "Well-conditioned Nyström discretization of the volume integral equation for eddy current analysis," IEEE Transactions on Magnetics, vol. 51, p. 1–6, Feb 2015.
[29] S. D. Gedney, "On deriving a locally corrected Nyström scheme from a quadrature sampled moment method," IEEE Transactions on Antennas and Propagation, vol. 51, pp. 2402–2412, Sep 2003.
[30] M. Shafieipour, I. Jeffrey, J. Aronsson, and V. I. Okhmatovski, "On the equivalence of rwg method of moments and the locally corrected Nyström method for solving the electric field integral equation," IEEE Transactions on Antennas and Propagation, vol. 62, pp. 772–782, Feb 2014.
[31] M. Shafieipour, J. Aronsson, I. Jeffrey, and V. I. Okhmatovski, "Exact relationship between the locally corrected Nyström scheme and RWG moment method for the mixed-potential integral equation," IEEE Transactions on Antennas and Propagation, vol. 63, p. 4932–4943, Nov 2015.
[32] R. R. Alavi, A. Kiaee, R. Mirzavand, and P. Mousavi, "Rwg mom-via-locally corrected Nyström method in near-field to far-field transformation using very-near-field measurement," IET Microwaves, Antennas Propagation, vol. 12, no. 2, pp. 145–153, 2018.
[33] R. Graglia, D. Wilton, and A. Peterson, "Higher order interpolatory vector bases for computational electromagnetics," IEEE Transactions on Antennas and Propagation, vol. 45, p. 329–342, March 1997.
[34] N. G. Zamani, J. F. Porter, and A. A. Mufti, "A survey of computational efforts in the field of corrosion engineering," International Journal for Numerical Methods in Engineering, vol. 23, no. 7, p. 1295–1311, 1986.
[35] V. G. DeGiorgi and S. A. Wimmer, "Review of sensitivity studies for impressed current cathodic protection systems," Proceedings of the ASME 2011 International Design Engineering Technical Conference & Computers and Information in Engineering Conference, Aug 2011.
[36] J. V. Kurian, A. M. Al-Yacouby, A. A. Sebastian, M. S. Liew, and V. G. Idichandy, "Effect of anodes on hydrodynamic coefficients of tubular cylinders - model tests," vol. 567, pp. 241–246, 2014.
[37] N. Zamani, "Boundary element simulation of the cathodic protection system in a prototype ship," Applied Mathematics and Computation, vol. 26, no. 2, p. 119–134, 1988.
[38] G. Qiao, B. Guo, and J. Ou, "Numerical simulation to optimize impressed current cathodic protection systems for rc structures," Journal of Materials in Civil Engineering, vol. 29, no. 6, p. 04017005, 2017.
[39] K. Wilson, M. Jawed, and V. Ngala, "The selection and use of cathodic protection systems for the repair of reinforced concrete structures," Construction and Building Materials, vol. 39, pp. 19 – 25, 2013. Special Issue: ISCCM 2011, Ningbo, China, November 7-9, 2011.
[40] S. Aoki, K. Amaya, and K. Gouka, "Optimal cathodic protection of ship," WIT Transactions on Modelling and Simulation, vol. 15, pp. 345–356, 1966.
[41] V. DeGiorgi, "A review of computational analyses of ship cathodic protection

systems," WIT Transactions on Modelling and Simulation, vol. 18, pp. 829–838, 1997.
[42] V. DeGiorgi, E. Hogan, K. Lucas, and S. Wimmer, "Issues in modeling electrochemical corrosion systems," WIT Transactions on Modelling and Simulation, vol. 34, pp. 172–180, 2003.
[43] R. W. Ditchfield, J. N. McGrath, and D. J. Tighe-Ford, "Theoretical validation of the physical scale modelling of the electrical potential characteristics of marine impressed current cathodic protection," Journal of Applied Electrochemistry, vol. 25, pp. 54–60, Jan 1995.
[44] V. DeGiorgi, E. Hogan, K. Lucas, and S. Wimmer Journal of Corrosion Science and Engineering, 01 2003.
[45] R. Adey, S. Niku, C. Brebbia, and J. Finnegan, "Computer aided design of cathodic protection systems," Applied Ocean Research, vol. 8, no. 4, p. 209–222, 1986.
[46] E. Santana-Diaz and R. Adey, "Predicting the coating condition on ships using iccp system data," International Journal for Numerical Methods in Engineering, vol. 62, no. 6, pp. 727–746, 2004.
[47] S. A. Wimmer and V. G. Degiorgi, "Detecting damage using electric field measurements: A computational sensitivity study," Tech. Rep. NRL/MR/6350–14-9438, Washington, DC, Feb 2014.
[48] M. Birsan, "Measurement and model predicted corrosion related magnetic signature," Tech. Rep. 2009-253, October 2010.
[49] R. S. Munn and O. F. Devereux, "Numerical modeling and solution of galvanic corrosion systems: Part i. governing differential equation and electrodic boundary conditions," CORROSION, vol. 47, no. 8, pp. 612–618, 1991.
[50] R. S. Munn and O. F. Devereux, "Numerical modeling and solution of galvanic corrosion systems: Part ii. finite-element formulation and descriptive examples," CORROSION, vol. 47, no. 8, pp. 618–634, 1991.
[51] D. Danson and M. Warne, "Current density/voltage calculations using boundary element techniques," NACE Conference, Los Angeles, 1983.
[52] J. O. Bockris, A. K. Reddy, and M. E. Gamboa-Aldeco, Modern Electrochemistry 2A: Fundamentals of Electrodics. Springer, 2001.
[53] F. Varela, Y. Kurata, and N. Sanada, "Prediction of current and potential distributions on galvanic corrosion by boundary element method," WIT Transactions on Modelling and Simulation, vol. 13, pp. 357–366, 1996.
[54] A. V. Nikiforov, I. M. Petrushina, and N. J. Bjerrum, "Electrochemical studies of corrosion in liquid electrolytes for energy conversion applications at elevated temperatures," in High Temperature Corrosion (Z. Ahmad, ed.), ch. 05, Rijeka: InTech, 2016.
[55] W. Sun, G. Yuan, and Y. Ren, "Iterative algorithms for impressed cathodic protection systems," International Journal for Numerical Methods in Engineering, vol. 49, pp. 751–768, 2000.
[56] J. Chuang, N. Zamani, and C. Hsiung, "Some computational aspects of bem simulation of cathodic protection systems," Applied Mathematical Modelling, vol. 11, p. 371–379, Oct 1987.

[57] A. Keddie, M. Pocock, and V. DeGiorgi, "Fast solution techniques for corrosion and signatures modelling," WIT Transactions on Engineering Sciences, vol. 54, pp. 225–234, 2007.
[58] M. D. Pocock and V. G. DeGiorgi, "Combining boundary element and discrete source methods for the modelling of corrosion related magnetic fields," Wessex Institute of Technology Publications, vol. 34, May 2003.
[59] P. Allan and A. Watt, "A study of corrosion related electromagnetic signatures of marine vessels using a bem," WIT Transactions on Modelling and Simulation, vol. 37, pp. 357–367, 2004.
[60] R. Adey and J. M. W. Baynham, "Predicting corrosion related signatures," Simulation of Electro-chemical Processes II. WIT Transactions on Engineering Sciences, vol. 54, pp. 213–223, 2007.
[61] A. Guibert, J. L. Coulomb, O. Chadebec, and C. Rannou, "A post-processing integral formulation for the computation of magnetic field in conductors," IEEE Transactions on Magnetics, vol. 47, pp. 1334–1337, May 2011.
[62] A. Mujezinović, S. Martinez, A. Muharemović, and I. Turković, "Application of the coupled bem/fem method for calculation of cathodic protection system parameters," International Journal of Computational Methods and Experimental Measurements, vol. 5, p. 659–666, Sept 2017.
[63] J. A. Stratton, Electromagnetic Theory. New York: McGraw-Hill Book Company, Inc., 1941.
[64] F. Caliskan and A. F. Peterson, "The need for mixed-order representations with the locally corrected Nyström method," IEEE Antennas and Wireless Propagation Letters, vol. 2, pp. 72–73, 2003.
[65] G. H. Golub and C. F. Van Loan, Matrix Computations (3rd Ed.). Baltimore, MD, USA: Johns Hopkins University Press, 1996.
[66] R. F. Harrington, Time-Harmonic Electromagnetic Fields. New York: McGraw-Hill, 1961.
[67] A. F. Peterson, S. L. Ray, and R. Mittra, Computational methods for electromagnetics. New York: IEEE Press, 1998.
[68] W. C. Chew, Waves and Fields in Inhomogenous Media. New York: IEEE Press, 1999.
[69] P. Yla-Oijala and M. Taskinen, "Well-conditioned Müller formulation for electromagnetic scattering by dielectric objects," IEEE Trans. Antennas Propagat. IEEE Transactions on Antennas and Propagation, vol. 53, no. 10, p. 3316–3323, 2005.
[70] S. D. Gedney, A. Zhu, and C.-C. Lu, "Study of mixed-order basis functions for the locally corrected Nyström method," IEEE Transactions on Antennas and Propagation, vol. 52, pp. 2996–3004, Nov 2004.
[71] W. R. Smythe, Static and dynamic electricity. New York: McGraw-Hill, 1939.
[72] K. Fujiwara and T. Nakata, "Results for benchmark problem 7 (asymmetrical conductor with a hole)," COMPEL - The international journal for computation and mathematics in electrical and electronic engineering, vol. 9, pp. 137–154, Dec 1990.
[73] N. G. Zamani, J. M. Chuang, and J. F. Porter, "BEM simulation of cathodic

protection systems employed in infinite electrolytes," International Journal for Numerical Methods in Engineering, vol. 24, no. 3, p. 605–620, 1987.
[74] J. D. Jackson, Classical Electrodynamics. New York: John Wiley & Sons, Ltd., 1962.
[75] N. Morita, N. Kumagai, and J. R. Mautz, Integral equation methods for electromagnetics. Artech House, 1990.
[76] F. Zhang, ed., The Schur Complement and Its Applications. New York: Springer-Verlag, 2005.
[77] N. Chen, S. L. Ho, and W. N. Fu, "An efficient two-grid finite-element method of 3-d nonlinear magnetic-field computation," IEEE Transactions on Magnetics, vol. 45, pp. 4797–4800, Oct 2009.
[78] S. A. Wimmer, V. G. Degiorgi, and E. A. Hogan, "Computational prediction of electric fields in shallow water testing environment," Volume 2: 29th Computers and Information in Engineering Conference, Parts A and B,San Diego, California, USA, Aug-Sept 2009.
[79] J.-C. Lin and D. Durand, "Magnetic field of current monopoles in prolate and oblate spheroid volume conductors," IEEE Transactions on Magnetics, vol. 34, pp. 2177–2184, 1998.
[80] A. Ferguson and D. Durand, "A theory of the magnetic field from current monopoles," Journal of Applied Physics, vol. 71, pp. 3107–3113, 1992.
[81] M. G. Duffy, "Quadrature over a pyramid or cube of integrands with a singularity at a vertex," SIAM Journal on Numerical Analysis, vol. 19, pp. 1260–3, Dec 1982.
[82] S. E. Mousavi and N. Sukumar, "Generalized duffy transformation for integrating vertex singularities," Computational Mechanics, vol. 45, p. 127, Oct 2009.

Vita

Robert Pfeiffer received a B.A. in Liberal Arts from Thomas Aquinas College, Santa Paula, CA, in May of 2012. He studied Electrical Engineering at the Milwaukee School of Engineering in Milwaukee, WI, from September 2012 to May 2014. During this time he worked as an engineering intern for Johnson Controls Inc. He received the M.S. in Electrical Engineering in December 2015 at the University of Kentucky in Lexington, KY, where he has worked as a graduate research assistant since August 2014.